

# **Quantum-mimetic imaging**

by

Dheera Venkatraman

B.S., Massachusetts Institute of Technology (2006)

M.Eng., Massachusetts Institute of Technology (2007)

Submitted to the Department of Electrical Engineering and Computer  
Science

in partial fulfillment of the requirements for the degree of

Doctor of Philosophy

at the

MASSACHUSETTS INSTITUTE OF TECHNOLOGY

February 2015

© Massachusetts Institute of Technology 2015. All rights reserved.

Author .....  
.....

Department of Electrical Engineering and Computer Science  
January 30, 2015

Certified by .....  
.....

Franco N. C. Wong  
Senior Research Scientist  
Thesis Supervisor

Accepted by .....  
.....

Leslie A. Kolodziejski  
Chairman, Department Committee on Graduate Theses



# **Quantum-mimetic imaging**

by

Dheera Venkatraman

Submitted to the Department of Electrical Engineering and Computer Science  
on January 30, 2015, in partial fulfillment of the  
requirements for the degree of  
Doctor of Philosophy

## **Abstract**

Many recent experiments have explored the use of nonclassical states of light to perform imaging or sensing. Although these experiments require quantum descriptions of light to explain their behavior, the advantages they claim are not necessarily unique to quantum light. This thesis explores the underlying principles behind two of those imaging techniques and realizes classical experiments that demonstrate similar properties to their quantum counterparts.

The principal contributions of this thesis in the preceding quantum-mimetic imaging paradigm are the experimental implementation of phase-conjugate optical coherence tomography and phase-sensitive ghost imaging, two experiments whose quantum counterparts utilize phase-sensitive light with nonclassical strength. This thesis also explores the use of compressed sensing to further speed up acquisition of ghost imaging.

Finally, a new paradigm inspired by compressed sensing is demonstrated, in which high-quality depth and reflectivity images are simultaneously captured using only the first photon arrival at each pixel. This paradigm is also extended to the case of single-photon APD arrays which may offer few-photon low-light imaging capabilities beyond what is possible with current camera technologies.

Thesis Supervisor: Franco N. C. Wong

Title: Senior Research Scientist



## Acknowledgments

First and foremost I am extremely grateful to my advisor Senior Research Scientist Dr. Franco Wong, without whom this research would not be possible, and to thesis committee members Prof. Jeffrey Shapiro and Prof. Vivek Goyal for being true mentors throughout the course of this work.

Dr. Wong was an extraordinary mentor who was highly inspirational and encouraging at every step along this research. He was not only extremely patient and available with every student, but also a quick and pragmatic thinker when any kind of difficulties arose in the laboratory. His guidance over the years was invaluable in the path to true step-by-step scientific research and in becoming a more independent thinker, communicator, and problem-solver.

Prof. Shapiro was an excellent teacher and his scientific rigor provided invaluable insight in understanding the theoretical foundations of our work. His presentations and comments at conferences, group meetings, and 6.453 lectures have always inspired me to strive harder to express concepts more clearly and concisely, and he always was willing to make time amidst his numerous responsibilities to jump in and provide his theoretical insights on any situation.

Embarking on cross-disciplinary projects has always been my true passion. Prof. Goyal, whose expertise is more concentrated on the signal processing side of our work, was highly supportive of our collaborative endeavor, and in the process was always patient in mentoring and exposing me to completely different viewpoints and approaches to scientific problems. The many cross-group discussions and debates were extremely insightful about not only our research project but also the possibilities that lie in the future for producing high-impact results through interdisciplinary collaborations.

I would like to thank all fellow group members, current and former, in no particular order: Zheshen Zhang, Sara Mouradian, Murphy Niu, Valentina Schettini, Maria Tengner, Raúl García-Patrón, Veronika Stelmakh, Tian Zhong, Taehyun Kim, Onur Kuzucu, Saikat Guha, Nicholas Hardy, Julian Le Gouët, Baris Erkmen, and my research collaborators Ahmed

Kirmani, Andrea Colaço, Dongeek Shin, Rudi Lussana, for the numerous thought-provoking discussions in the office and laboratory, and the many insights that we have shared over the years which have helped me grow as a researcher and person.

Being able to express thoughts coherently and cultivate talent in younger students is also an indispensable part of humanity's scientific endeavors. I thank Prof. Dennis M. Freeman who offered me the opportunity to be a teaching assistant for 6.003, for his true enthusiasm and heart in exceptional teaching, and for setting an example of quality education. It was also through being a teaching assistant that I learned that although receiving an A in a course demonstrates ability to grasp subject matter from one angle, it is not until you try to teach the course to someone else that one truly and thoroughly understands the subject matter and the multiple valid ways of approaching each and every detail.

I would like to thank the numerous student and professional organizations on campus who have provided a support network, forged true friendships, and expanded my career horizons. These include the MIT-China Innovation and Entrepreneurship Forum, the MIT Sustainability Summit, the MIT Chinese Students and Scholars Association, the MIT Singapore Students Society, the MIT Republic of China (Taiwan) Students Association, and the Ashdown House Executive Committee, through all of which I have met numerous fellow MIT colleagues who have helped me develop the professional side of my career and fostered cross-disciplinary connections and opportunities to startups and industries worldwide. To the same extent I also thank all of my friends, too numerous to list here, who have supported me over the years.

Last but not least, I would also like to thank my parents and family for all their support both before and during my years at MIT.

This thesis marks the end of not only a doctoral program, but also a much longer chapter of my life at MIT including my earlier years as an undergraduate at the Institute. Although I spent much of my childhood moving from place to place, my decade at MIT has by far made the biggest impact on my life, both academically and personally. From late-night hacking on electronics projects to serious entrepreneurship discussions in the hallways, MIT has always

been an open playground, both literally and figuratively, for both academic and extracurricular innovation, and it is by far the culture of openness, freedom, and mutual trust that I have found most helpful in fostering true synergies among the highly-motivated scientists, leaders, and innovators. I cannot express the gratitude I have for all the conveniences MIT provides, including effectively unlimited static IP addresses and no port restrictions, unlimited symmetric bandwidth, gigabit ethernet drops in every bedroom, open buildings and classrooms, laser cutters, machine shops, electronics supply rooms, piano practice rooms, and the myriad other resources that have been exceedingly useful both directly and indirectly to my doctoral research and further professional pursuits. The unique openness and willingness of MIT community members to trust, support, and mentor each other, form cross-disciplinary collaborations, share access to resources, and share expertise have also been invaluable to all of my developments at MIT.

This work was supported by the DARPA Quantum Sensors Program, the DARPA InPho program through the U.S. Army Research Office, and by the National Science Foundation.



# Contents

<b>1</b>	<b>Introduction</b>	<b>19</b>
<b>2</b>	<b>Phase-conjugate optical coherence tomography</b>	<b>23</b>
2.1	Optical coherence tomography configurations . . . . .	24
2.1.1	Conventional OCT . . . . .	24
2.1.2	Quantum OCT . . . . .	26
2.1.3	Phase-conjugate OCT . . . . .	28
2.2	Generating phase-sensitive light with parametric downconversion . . . . .	30
2.2.1	Single-mode parametric fluorescence . . . . .	30
2.2.2	SPDC under strong pumping . . . . .	34
2.3	Experimental setup . . . . .	35
2.3.1	SPDC source . . . . .	35
2.3.2	Double-pass configuration and phase conjugation . . . . .	36
2.3.3	Dispersion simulation using long fiber spool . . . . .	38
2.3.4	Interferometric measurement . . . . .	40
2.3.5	Data collection . . . . .	41
2.4	Results . . . . .	41
2.5	Conclusions . . . . .	44
<b>3</b>	<b>Classical phase-sensitive ghost imaging</b>	<b>47</b>
3.1	Near- and far-field ghost imaging . . . . .	49
3.2	Ghost imaging with spatial light modulators . . . . .	51

3.2.1	SLM: Principle of operation . . . . .	51
3.2.2	Pitfalls . . . . .	51
3.3	Experimental setup . . . . .	53
3.4	Results . . . . .	55
3.5	Signal-to-noise ratio . . . . .	58
3.6	Computational ghost imaging . . . . .	59
3.7	Compressed ghost imaging . . . . .	63
3.8	Computational compressed ghost imaging . . . . .	67
3.9	Conclusions . . . . .	68
<b>4</b>	<b>Single-photon imaging</b>	<b>73</b>
4.1	First-photon imaging . . . . .	75
4.1.1	Experimental setup and calibration . . . . .	75
4.1.2	Computational reconstruction procedure . . . . .	82
4.1.3	Results . . . . .	88
4.2	Reflectivity from depth data . . . . .	92
4.3	Imaging using a SPAD array . . . . .	93
4.3.1	Hardware specifications . . . . .	94
4.3.2	Experimental setup . . . . .	96
4.3.3	Computational reconstruction approach . . . . .	98
4.3.4	Preliminary results . . . . .	99
4.3.5	Comparison to first-photon imaging . . . . .	100
4.4	Conclusions . . . . .	101
<b>5</b>	<b>Conclusions</b>	<b>115</b>
<b>Appendices</b>		<b>119</b>
<b>A</b>	<b>HydraHarp file converter</b>	<b>121</b>
<b>B</b>	<b>SPAD file converter</b>	<b>133</b>

## List of Figures

2-1	Schematic of conventional optical coherence tomography (C-OCT). . . . .	25
2-2	Schematic of quantum optical coherence tomography (Q-OCT). . . . .	27
2-3	Schematic of phase-conjugate optical coherence tomography (PC-OCT). . . . .	28
2-4	Schematic of setup for parametric fluorescence generation and collection in single-mode fiber. We use type 0 phase matching (signal, idler, pump are polarized on the same axis) in a MgO:PPLN crystal. . . . .	31
2-5	Spectrum of a home-built passively mode-locked fiber laser [1] used as a seed source. . . . .	32
2-6	EDFA output spectrum at maximum output power setting, before and after modifications by IPG Photonics to remove excess internal fiber. The broadening of the spectrum and double peak is caused by self-phase modulation inside the fiber at high power levels. . . . .	33
2-7	EDFA output power (1560 nm) as a function of drive current, showing linear behavior with a threshold of $\sim$ 400 mA. . . . .	34
2-8	SHG output power (780 nm) as a function of input power (1560 nm), showing quadratic dependence at low power levels and linear dependence at high power levels. . . . .	35
2-9	SPDC output power as a function of pump power, showing the linear dependence in the low-flux regime and exponential dependence in the high-flux (amplified) regime. . . . .	36

2-10 (a) Power spectral densities (solid) and theoretical models based on Sellemeier coefficients (dashed) for various crystal temperatures, with pump power fixed at 2 W. (b) Linear dependence of SPDC output bandwidth as a function of pump power, with temperature fixed at 86°C. . . . .	37
2-11 PC-OCT experimental setup. CWDM: course Wavelength division Multi-plexer, OPA: optical parametric amplifier, PBS: polarizing beamsplitter. . . . .	38
2-12 Transmittance of 1550 nm and 1570 nm channels of the CWDM, scanned using a InGaAs detector and tunable fiber-coupled laser with a maximum wavelength of 1575 nm, showing nearly flat-top transmission and sharp falloff, allowing the reference and signal to be efficiently separated. . . . .	39
2-13 (a) Center position and (b) FWHM of the PC-OCT interferometric envelope, with (c) synchronized measurements of the ambient room temperature, showing the effect of temperature on the index of refraction of the long fibers in the experiment. . . . .	40
2-14 Three PC-OCT scans with a high reflectivity mirror used as a target, translated by 450 $\mu\text{m}$ between subsequent scans. . . . .	42
3-1 Conceptual ghost imaging schematic, reproduced from Erkmen et al. [2]. . .	49
3-2 Pseudothermal SLM-based ghost imaging setup which can be operated in either phase-sensitive mode (anti-correlated SLM phase patterns) or phase-insensitive mode (identical SLM phase patterns). . . . .	52
3-3 (a) Sample single-frame speckle pattern as imaged by the CCD. The artifact in (a) is due to the SLMs' inter-pixel dead space. (b) Portion of a USAF spatial-resolution transmission mask used as the object. (c) Phase-insensitive and (d) phase-sensitive far-field ghost images, each averaged over 18640 realizations.	54

3-4 MIT-logo ghost images after 7000 realizations for (a) phase-insensitive and (b) phase-sensitive light, showing image inversion in (b). The images are individually normalized, with the noise levels clipped for improved visibility. The bright-spot artifact at the center prevents us from obtaining an image in that small region. . . . .	56
3-5 Far-field ghost imaging under loose focusing ( $w_0 = 150 \mu\text{m}$ ) for (a) and (b), and tight focusing ( $w_0 = 50 \mu\text{m}$ ) for (c) and (d), with the SLM located at a distance of $2.75 \times$ the Rayleigh range $z_R$ . The mask is an off-center letter M. Phase-insensitive images in (a) and (c) are not affected, but phase-sensitive measurements in (b) and (d) show degradation that is severe for tight focusing in (d). . . . .	57
3-6 Theoretical (blue) and experimental (red) signal-to-noise ratio curves for a simple square transmission mask as a function of the number of realizations $N$ . . . . .	59
3-7 Computational ghost imaging schematic, in which there are no spatially resolving detectors and the reference arm is replaced by a computer-generated reference that is used to drive the spatial light modulator. . . . .	60
3-8 Pseudothermal, phase-insensitive ghost imaging setup used to test computational and compressed ghost imaging. In computational ghost imaging, we do not use the CCD camera. . . . .	60
3-9 (a) Sample pseudorandom phase pattern imposed on SLM. The phase modulation at each pixel is independent and uniformly distributed on $[0, 2\pi]$ and encoded as a greyscale value in this visualization. (b) Simulated result of the far-field speckle pattern. . . . .	61
3-10 Side-by-side results of an MIT logo mask imaged using (a) traditional ghost imaging with optical signal and reference arms and (b) computational ghost imaging in which the reference arm is replaced by a computer simulation, averaged over $M = 300$ to 9600 independent pseudorandom phase patterns. . . . .	62

3-11 Schematic of the Rice University single pixel camera, reproduced from [3]. DMD: digital micromirror device, PD: photodetector, DSP: digital signal processor, RNG: random number generator. (TODO: add (a) and (b) to figure)	63
3-12 Ghost images processed using compressed sensing for a binary MIT logo mask, using (a) DCT and (b) TV sparsifying transforms. . . . .	65
3-13 Ghost images of an MIT logo mask imaged using (a) traditional averaging and (b) compressed sensing using the same data set. . . . .	66
3-14 Relaxing the constraint to varying degrees in the computational reconstruction using DCT as a sparsifying basis. From top to bottom, we increase the number of realizations, and from left to right, we relax the equality constraint, allowing for errors in the data. We used this process to determine the value of the relaxation parameter $\epsilon$ to use. . . . .	70
3-15 Attempts to obtain images of an MIT logo mask imaged using compressed sensing with a computationally-simulated reference arm. (a) shows the com- putational ghost imaging result using traditional processing, and (b) shows the result of applying compressed sensing techniques. (TODO: add (a) and (b) to figure) . . . . .	71
3-16 Computational compressed ghost imaging using a simpler object. (a) MIT logo mask and ghost image results for (b) covariance-based and (c) compressed sensing using TV minimization for the same number of realizations, showing the same problems seen in Figure 3-15. (d) Simpler square mask and results using (e) covariance-based and (f) compressed sensing using TV minimization.	71
3-17 Sample speckle patterns acquired by a CCD array (left) and the corresponding computational simulation results (right). We attribute the large discrepancy to imperfections in the SLM array. . . . .	72
4-1 Schematic of the raster-scanning imager used for first-photon imaging. . . . .	77
4-2 Raster scanning was performed in alternating directions for each row in order to avoid abrupt transitions in translating the galvo mirrors. . . . .	79

4-3	Description of the MATLAB-friendly .out format generated by our custom GNU C .ht3 file reader. . . . .	80
4-4	Pulse shape of the PicoQuant LDH series laser diode obtained by histogramming, and skewed Gamma function fit. . . . .	81
4-5	Reflectivity and depth information obtained from a single photon arrival: the depth information is obtained by measuring the time difference between the photon arrival and the laser pulse sync signal, while the reflectivity information is obtained by the number of laser pulse periods elapsed until the first photon detection. . . . .	82
4-6	Early reflectivity and depth images of a mannequin and flower scene imaged using a $300 \times 300$ -pixel raster scan without added background noise. (a) Reference ("ground truth") measurement obtained using several hundred photon arrivals at each pixel, averaged. (b) Raw ML estimates obtained using only the first photon arrival at each pixel. (c) Our computational reconstruction method applied to the data in (b). . . . .	89
4-7	3D mesh views of a single first-photon acquisition with added background noise after various stages of processing. (A)-(C): Raw reflectivity ML estimate $\alpha_{ML}(x, y)$ superimposed over depth ML estimate $Z_{ML}(x, y)$ from first photon data, (D)-(F): after reflectivity reconstruction of $\alpha(x, y)$ , (G)-(I): after background noise censoring, (J)-(L): after depth reconstruction of $Z(x, y)$ . . .	90
4-8	Close-up of two regions of reflectivity data for mannequin target. (a) ML estimate using only 1 photon per pixel and (b) the same data after processing using our computational reconstruction technique. . . . .	91
4-9	Depth chart test consisting of square features of linearly increasing height. (a) Image produced by traditional averaging with several hundred detections per pixel, (b) ML estimate using only the first photon arrival, and (c) data in (b) processed using our computational reconstruction method. . . . .	103

4-10 Reflectivity chart test. (a) Image produced by traditional averaging with several hundred detections per pixel, (b) ML estimate using only the first photon arrival, and (c) data in (b) processed using our computational reconstruction method. . . . .	104
4-11 (a) Raw depth values from a $1000 \times 1000$ -pixel first-photon acquisition in the presence of high background noise, but range-gated to the indicated scale for visualization purposes. Evidence of high-reflectivity features on the T-shirt and face visually manifest as regions of coherent regions of color, which are the result of low variances in depth. (b) Reflectivity information gained from a version of (a) without range-gating. The number of pulses until the first detection was not used in this method. . . . .	105
4-12 Experimental setup for single-photon imaging with a SPAD array. (TODO: Increase font size) . . . . .	106
4-13 Scanning scheme to obtain high-resolution images using the $32 \times 32$ -pixel SPAD array. (a) We translate the array by increments of a full array size (4.8 mm) along both axes to image multiple "tiles" of the entire array. (b) Zoom-in view of individual SPAD pixels showing the active area with no subpixel scanning, (c) $2 \times 2$ subpixel scanning by translating along each axis by 75 $\mu\text{m}$ , multiplying the resolution by 2 and (d) $4 \times 4$ subpixel scanning by translating along each axis by 37.5 $\mu\text{m}$ , 75 $\mu\text{m}$ , and 112.5 $\mu\text{m}$ , multiplying the resolution by 4. . . . .	107
4-14 Terminology used in the describing the SPAD array imaging acquisition scheme.	108
4-15 SPAD array imaging results for $360 \times 360$ -pixel reflectivity images of a mannequin comparing traditional averaging with spatial regularization. Dwell times are in time units of acquisition frames (65 $\mu\text{s}$ ). . . . .	109
4-16 SPAD array imaging results for $360 \times 360$ -pixel reflectivity images of a table, cardboard box, and books comparing traditional averaging with spatial regularization. Dwell times are in time units of acquisition frames (65 $\mu\text{s}$ ). . . . .	110

4-17 SPAD array imaging results for $360 \times 360$ -pixel reflectivity images of two basketballs comparing traditional averaging with spatial regularization. Dwell times are in time units of acquisition frames ( $65 \mu\text{s}$ ). . . . .	111
4-18 First-photon reflectivity imaging of three scenes simulated using the SPAD array, in which only the first arrival at each pixel is used regardless of subsequent arrivals within a fixed dwell time. (a) Traditional ML estimate of the reflectivity and (b) the same data after processing using our first-photon imaging technique described in the previous section. Depth results are not generated since $s(\cdot)$ is nearly a delta function for the laser pulse width and time bin size used. . . . .	112
4-19 SPAD array imaging results for $360 \times 360$ -pixel depth maps of a mannequin comparing traditional averaging with spatial regularization. Dwell times are in time units of acquisition frames ( $65 \mu\text{s}$ ). Pixels with no data are represented as depth values of 0. . . . .	113



# Chapter 1

## Introduction

Over the latter half of the 20th century much attention has been devoted to applying quantum-mechanical foundations previously laid by Heisenberg, Hilbert, Dirac, von Neumann, Schrodinger, and other early theoreticians. Many properties unique to quantum mechanics, including projective measurement, entanglement, no-cloning theorem, quantized eigenstates of systems, the uncertainty principle, and quantum descriptions of electromagnetic fields, led scientists to consider real-world applications of these quantum effects that are not realizable using classical physics. Today, many high-impact, widespread technologies are based on these quantum mechanical foundations, including magnetic resonance imaging, flash drive storage, laser technologies, and atomic clocks. Numerous other quantum techniques have been proposed and are highly active areas of research, including quantum cryptography, quantum computation, quantum error correction, and quantum imaging, with hopes that they will find widespread applications in the near future.

Most schemes for quantum sensing and measurement claim improvements over traditional classical imaging in a variety of properties ranging from resolution to privacy to background-free measurements. However, although it is often verifiable both theoretically and experimentally that the quantum versions of these experiments do indeed offer the proposed improvements, this is not a rigorous proof that they necessarily owe their improvements to quantum mechanical effects, and that there does not exist a classical but non-traditional

experiment scheme to realize the same.

In this thesis we focus more specifically on quantum-mimetic imaging, the study of classical imaging experiments that demonstrate properties similar to their quantum counterparts. In particular, most biphoton sources, such as those using nonlinear crystals generate phase-sensitive coherence between the signal and idler beams. In contrast, most everyday classical light sources, including thermal light, sunlight, light-emitting diodes which are typically only capable of producing phase-insensitive coherence. Most quantum metrology experiments employ entangled biphoton sources, and therefore it is common to attribute their advantages to quantum entanglement. However, in many cases those advantages arise from phase-sensitive coherence alone, and in this work we will examine two such cases: quantum optical coherence tomography (OCT) and quantum ghost imaging.

In Chapters 2 and 3 we focus on these two experiments, respectively, using two different techniques to construct a classical phase-sensitive light source. Chapter 2 describes a phase-conjugate optical coherence tomography (OCT) system using an amplified downconversion-based classical phase-sensitive light source that realizes two of the key advantages afforded by quantum OCT without utilizing quantum entanglement. In Chapter 3 we develop a different classical phase-sensitive light source based on a pair of spatial light modulators that mimics the properties of phase-sensitive ghost imaging, also previously thought to be uniquely quantum. In addition, we learn that classical ghost imaging has the additional advantage of being able to employ compressed sensing, a computational reconstruction technique to make use of spatial correlations present in real-world scenes to increase acquisition speed by as much as a factor of 10.

In Chapter 4 we describe a research collaboration in which we take concepts learned from computational reconstruction in ghost imaging and apply them to a more general description of imaging. In particular, we develop first-photon imaging, an imaging framework to acquire high-quality depth and reflectivity images of real-world scenes using only one photon per pixel of data, and also begin development of a similar framework for acquisition of high-quality images using single-photon detector arrays.

Finally, in Chapter 5 we conclude this thesis, summarize the novel contributions, and propose potential future extensions to the work presented here.

TODO expand Kevin Resch, Howell et al



# Chapter 2

## Phase-conjugate optical coherence tomography

The past two decades have witnessed a number of experiments focused on the use of quantum-entangled states of light to achieve enhanced measurement capability in metrology. For example, quantum optical coherence tomography (Q-OCT) proposed by Abouraddy et al. [4] and later demonstrated by Nasr et al. [5], utilized maximally entangled photon states and Hong-Ou-Mandel interferometry [6] to achieve a  $2\times$  axial resolution improvement and dispersion cancellation over standard conventional OCT.

Such effects, including the enhanced resolution afforded by the reduced width of the Hong-Ou-Mandel interference, and dispersion cancellation [7, 8], were initially thought to be distinctly non-classical. However, much of the early research overlooked the possibility of classical light sources that possess no entanglement but are nevertheless maximally correlated in the classical, stochastic sense. Recent advances in nonlinear optical crystals and a better understanding of parametric downconversion have permitted us to generate a variety of these interesting classical light fields that bear properties previously associated exclusively with quantum optics. Of particular note is the ability to generate classical states with classically-maximal phase-sensitive correlations.

In particular, in the case of Q-OCT, Erkmen and Shapiro [9] have shown that both the

$2\times$  axial resolution improvement and dispersion cancellation are not exclusively quantum effects, but merely a result of the phase-sensitive cross-correlation between the signal and idler of the biphoton state. This leads to the question of whether the same advantages can be obtained from an experiment with classical phase-sensitive light sources, which are uncommon but can be experimentally constructed. Erkmen and Shapiro proposed such a technique [9], called phase-conjugate optical coherence tomography (PC-OCT) which uses an unconventional arrangement using only classical light sources and classical photodetectors to achieve both of these advantages previously associated with Q-OCT.

In this chapter we explore classical, quantum, and phase-conjugate OCT configurations, build a parametric downconversion-based source to generate classical phase-sensitive light, and use it to implement PC-OCT.

## 2.1 Optical coherence tomography configurations

Optical coherence tomography (OCT) is a three-dimensional imaging technique that employs interference measurements to derive axial resolution. We explore three main techniques by which this is accomplished: conventional OCT (C-OCT), quantum OCT (Q-OCT), and phase-conjugate OCT (PC-OCT). In our analysis we disregard transverse scanning, and focus solely on axial (depth) resolution, which is the differentiating aspect of the three methods.

### 2.1.1 Conventional OCT

The basic principle of C-OCT is shown in Figure 2-1. C-OCT uses classical signal and reference light beams that have phase-insensitive cross-correlations, as might be generated using any classical high-flux source with a short coherence length (such as an LED or pulsed laser source) and a 50-50 beam splitter. The signal beam interrogates the sample and the reflected light is recombined with the reference beam using a simple Michelson interferometer to measure the second-order correlations between the two beams. As the path length of either

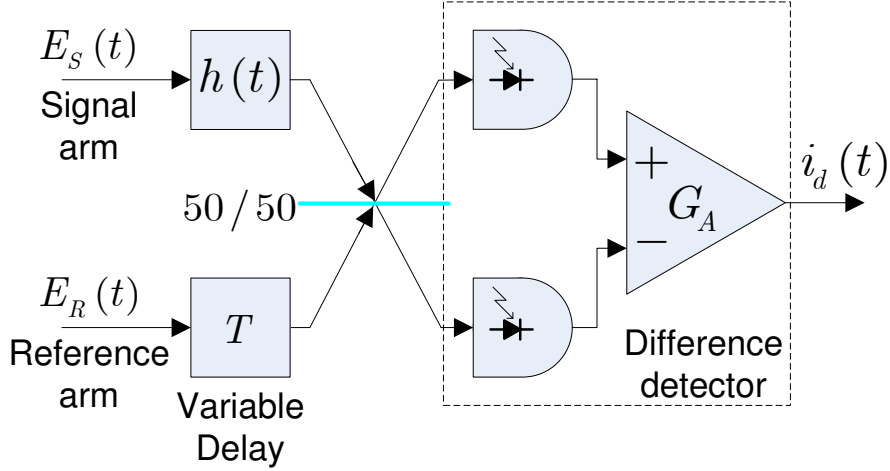


Figure 2-1: Schematic of conventional optical coherence tomography (C-OCT).

beam is scanned, the interference envelope reflects the axial profile of the target.

Erkmen describes in [10] the analytic computation of the interference signature of C-OCT, which we briefly summarize here. We assume classical zero-mean, stationary, jointly Gaussian signal and reference fields with complex envelopes  $E_S(t)$  and  $E_R(t)$  with powers  $\hbar\omega_0|E_K(t)|^2$  for  $K = S, R$ , respectively. In the case of C-OCT there are no phase-sensitive cross-correlations, and these fields are completely characterized by their phase-insensitive auto- and cross-correlations:

$$\langle E_J^*(t + \tau) E_K(t) \rangle = \mathcal{F}^{-1}[S(\Omega)] \quad (2.1)$$

for  $J, K = S, R$  where

$$\mathcal{F}^{-1}[S(\Omega)] = \int_{-\infty}^{\infty} \frac{d\Omega}{2\pi} S(\Omega) e^{i\Omega r} \quad (2.2)$$

is the inverse Fourier transform of  $S(\Omega)$  and  $S(\Omega) = S(-\Omega)$  is the common spectrum of the signal and reference beams at  $\pm\Omega$  from the center frequency  $\omega_0$ . We assume a target with an axial profile  $h(t)$ , where  $t$  is the time delay incurred in interrogating the target, and

baseband impulse response  $H(\Omega) = \mathcal{F}[h(t)]$ . In the case of a weakly reflecting mirror located at time delay  $T_0$  and complex reflectivity  $r$  with  $|r| \ll 1$ , this baseband impulse response is defined by:

$$H(\Omega) = r e^{i(\omega_0 + \Omega)T_0}. \quad (2.3)$$

After the signal field  $E_S(t)$  interacts with the sample, the resulting field is described by the convolution of  $E_S(t)$  with  $h(t)$ . An interferometric measurement is then made with the reference beam  $E_R(t)$  delayed by time  $T$ . As shown by Erkmen and Shapiro [9], the resulting interferometric envelope is given by

$$\langle i_d(t) \rangle = 2q\eta G_A \operatorname{Re} \left( \int_{-\infty}^{\infty} \frac{d\Omega}{2\pi} H^*(-\Omega) S(\Omega) e^{-i(\Omega - \omega_0)T} \right). \quad (2.4)$$

Note that this envelope is linear in  $H(\Omega)$ . If we insert the response of the weakly reflecting mirror, we obtain an envelope proportional to  $e^{-\Omega_S^2(T_0-T)^2/2}$  for  $S(\Omega) \propto e^{-\Omega^2/2\Omega_S^2}$ . For a source with bandwidth  $\Omega_S$ , this gives us an axial resolution of  $4/\Omega_S$ , where we define resolution as the full-width between the  $e^{-2}$  attenuation points of the visibility envelope.

Note also that C-OCT is vulnerable to dispersion in the sample, which will manifest itself inside  $H(\Omega)$ . Due to the linear dependence on  $H(\Omega)$ , there will be no dispersion-cancelling properties in C-OCT.

### 2.1.2 Quantum OCT

In Q-OCT, first proposed by Abouraddy et al. [4], the signal and reference beams are replaced by an entangled biphoton source and the Michelson interferometer is replaced by a Hong-Ou-Mandel (HOM) interferometric measurement [11], as shown in Figure 2-2. In order to analyze Q-OCT we must use the quantum description of the fields. Suppose we have signal and reference beams with photon-unit field operators  $\hat{E}_S(t)$  and  $\hat{E}_R(t)$ , respectively, with commutators

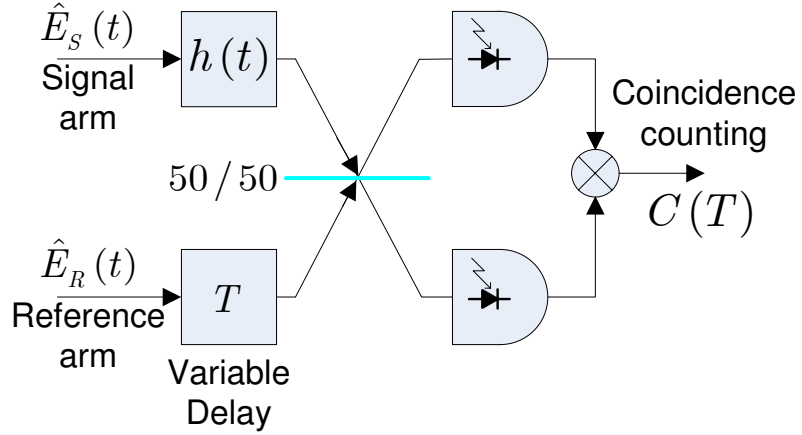


Figure 2-2: Schematic of quantum optical coherence tomography (Q-OCT).

$$[\hat{E}_J(t), \hat{E}_K^\dagger(u)] = \delta_{JK}\delta(t-u) \quad (2.5)$$

for  $J, K = S, R$ . We further assume that the fields have the maximum phase-sensitive cross-correlation permitted by quantum mechanics:

$$\langle \hat{E}_S(t + \tau) \hat{E}_R(t) \rangle = F^{-1}[\sqrt{S(\Omega)(S(\Omega) + 1)}] . \quad (2.6)$$

Under these conditions, and in the biphoton limit (low brightness and low photon flux) where HOM is usually performed,  $S(\Omega)$  and the photon coincidence counting signature is shown by Erkmen and Shapiro [9] to be:

$$\langle C(T) \rangle = \frac{q^2\eta^2}{2} \left[ \int_{-\infty}^{\infty} \frac{d\Omega}{2\pi} |H(\Omega)|^2 S(\Omega) - \text{Re} \left( \int_{-\infty}^{\infty} \frac{d\Omega}{2\pi} H^*(-\Omega) H(\Omega) S(\Omega) e^{-i2\Omega T} \right) \right] . \quad (2.7)$$

Using the same partially-reflecting mirror, the dip in the coincidence counts is proportional to  $e^{-2\Omega_S^2(T_0-T)^2}$ . Note that by the same resolution definition, we obtain an axial resolution of  $2/\Omega_S$  which is two times better than that of C-OCT for the same source bandwidth  $\Omega_S$ .

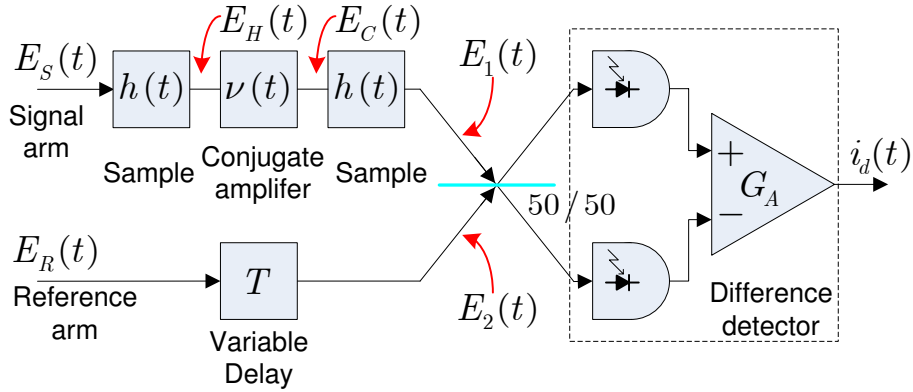


Figure 2-3: Schematic of phase-conjugate optical coherence tomography (PC-OCT).

Moreover, note that unlike C-OCT, the HOM dip term of Eq. 2.7 is nonlinear in  $H(\Omega)$  and involves a phase conjugation which will result in the cancellation of all even-order dispersion in the sample.

### 2.1.3 Phase-conjugate OCT

Although advantages of Q-OCT were earlier attributed to quantum effects, Erkmen and Shapiro showed that they are merely results of the phase-sensitive coherence between the signal and idler and achievable using PC-OCT [9], whose conceptual block diagram is shown in Figure 2-3. In this configuration, the signal and idler are classical sources with a phase-sensitive cross-correlation. The sample is interrogated twice at the same point with phase conjugation between the two passes.

In PC-OCT, we assume classical signal and idler complex envelopes  $E_S(t)$  and  $E_R(t)$  with maximal phase-sensitive correlations as permitted by classical physics. The signal beam  $E_S(t)$  is focused on a target with axial profile  $h(t) = F^{-1}[H(\Omega)]$ . The resulting complex envelope is

$$E_H(t) = E_S(t) * h(t) \quad (2.8)$$

where  $*$  denotes convolution. We then pass  $E_H(t)$  into a conjugate amplifier with impulse

response  $v(t)$ , resulting in the field:

$$E_C(t) = [E_H^*(t) + w(t)] * v(t) \quad (2.9)$$

where  $w(t)$  is zero-mean white Gaussian quantum noise injected by the conjugation process, satisfying *TODO*, and  $v(t)$  is the impulse response of the conjugator. After conjugation, the light is focused onto the same sample a second time, resulting in

$$E_1(t) = [E_C(t) * h(t)] . \quad (2.10)$$

We then recombine  $E_1(t)$  with the reference beam, delayed by  $T$ , in a Michelson interferometer, yielding an interference signature of the form

$$\langle i_d(t) \rangle = 2q\eta G_A \operatorname{Re} \left( \int_{-\infty}^{\infty} \frac{d\Omega}{2\pi} H^*(-\Omega) H(\Omega) V^*(-\Omega) S(\Omega) e^{-i(\Omega - \omega_0)T} \right) . \quad (2.11)$$

This interference signature bears much resemblance to the second term of the interference signature of Q-OCT; both PC-OCT and Q-OCT have  $H^*(\Omega)H(-\Omega)$  dependence. Indeed, if we use the same  $H(\Omega)$  of the low-reflectivity mirror, we obtain a visibility function proportional to  $e^{-2\Omega_S^2(T_0 - T/2)^2}$  and axial resolution of  $2/\Omega_S$  for a sufficiently broadband conjugator and  $S(\Omega) \propto e^{\Omega^2/2\Omega_S^2}$ , which is identical to the resolution afforded by Q-OCT. In addition, the  $H^*(\Omega)H(-\Omega)$  dependence of PC-OCT will result in even-order dispersion cancellation. Thus, PC-OCT realizes both of these advantages of Q-OCT with an entirely classical experiment.

It is also worth noting that PC-OCT can be (or may even preferably be) operated in a high-flux regime while Q-OCT cannot, since Q-OCT requires interference between individual photons and coincidence counting in order to perform the measurement. PC-OCT relies solely on classical interferometry, and thus is operable under a much wider range of conditions, including broad daylight, and data acquisition can be performed rapidly with classical detectors without large dwell times at each axial position.

## 2.2 Generating phase-sensitive light with parametric downconversion

Spontaneous parametric downconversion (SPDC) in nonlinear crystals was first observed in the 1960's and its properties extensively studied since then [12, 13, 14, 15, 16, 17, 18]. Recently, SPDC has been of particular interest to quantum optics experiments, particularly to generate heralded single photons [19, 20] and entangled photons [21, 22]. However, while SPDC is useful in the weakly-pumped regime for quantum optics, few works have exploited the strongly-pumped regime for its strong classical phase-sensitive coherence between the signal and idler beams, which we make use of to implement PC-OCT.

### 2.2.1 Single-mode parametric fluorescence

We would like to couple our SPDC outputs into a single-mode fiber to ensure maximal phase-sensitive cross-correlations between the signal and idler outputs, as well as for the experimental convenience afforded by fiber optics. As SPDC output is typically highly multi-modal, a number of studies [21, 23, 24, 25, 26, 27] have explored the idea of manipulating the focusing of the pump beam to concentrate the majority of SPDC output into a single spatial mode. Based on analysis from these earlier studies [28], we set our pump focusing parameter to  $\xi_p = L/(k_p w_p^2) = \pi/2$  where  $w_p$  is the pump waist size and  $k_p$  is the wavenumber of the pump beam. However, a later and more comprehensive study by Bennink [29] which was later supported by results by Dixon et al. [30] shows that under the approximation that the focusing parameters of the signal, idler, and pump are similar ( $\xi_s \approx \xi_i \approx \xi_p \approx \xi$ ), the joint spectral density of the signal and idler  $|\psi(\omega_s, \omega_i)|^2$  is proportional to:

$$|\psi(\omega_s, \omega_i)|^2 \propto F(\xi, \Phi) = \int_{-1}^1 \frac{\sqrt{\xi} \exp(i\Phi l/2)}{1 - i\xi l} dl \quad (2.12)$$

where  $\Phi$  is the phase mismatch of the crystal. This is maximized for  $\xi \approx 2.84$  and  $\Phi \approx -1.04\pi$ , yielding  $F \approx 2.06$ . In our suboptimal focusing case of  $\xi = \pi/2$ ,  $F(\xi = \pi/2, \Phi)$  is

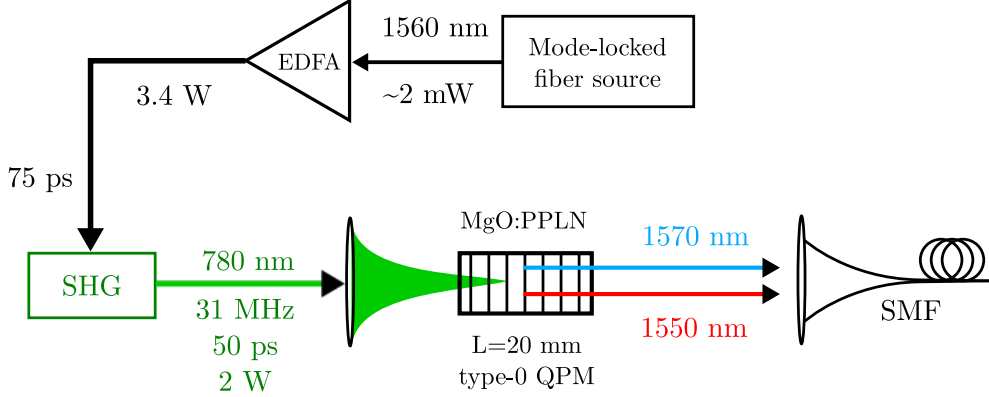


Figure 2-4: Schematic of setup for parametric fluorescence generation and collection in single-mode fiber. We use type 0 phase matching (signal, idler, pump are polarized on the same axis) in a MgO:PPLN crystal.

maximized for  $\Phi \approx -0.75\pi$ , yielding  $F \approx 1.96$ , implying that our joint spectral density is  $\sim 5\%$  less than optimal.

Figure 2-4 shows a schematic of the SPDC generation setup. A home-built passively mode-locked pulsed Er-doped fiber laser employing polarization-maintaining fiber [1] was used as a seed source. The center wavelength of 1560 nm was set by a Bragg grating within the laser cavity. The laser generated 75-ps pulses at a repetition rate of  $\sim 31.1$  MHz and average output power of  $\sim 1.9$  mW, with an output spectrum shown in Figure 2-5. This seed laser output was fed into an IPG Photonics Er-doped fiber amplifier (EDFA) with a maximum output of 6 W. In practice, we set the amplifier output power to a lower setting (typically 3-4 W) to avoid the effects of self-phase modulation (SPM), which at high power levels distorts the pulse shape and destroys the transform-limited properties of the pulse. In order to further reduce the effect of SPM, we had the EDFA serviced by IPG Photonics to reduce the internal fiber length to a bare minimum. The spectrum of the output at maximum power setting, before and after modification, is shown in Figure 2-6. The EDFA output power showed linear behavior as a function of drive current, after a minimum threshold of  $\sim 400$  mA, as shown in Figure 2-7.

We then frequency-doubled the free-space output of the EDFA using a MgO:PPLN crystal with a grating period of  $19.47 \mu$ , housed in a temperature-controlled oven set at  $86.5^\circ\text{C}$ ,

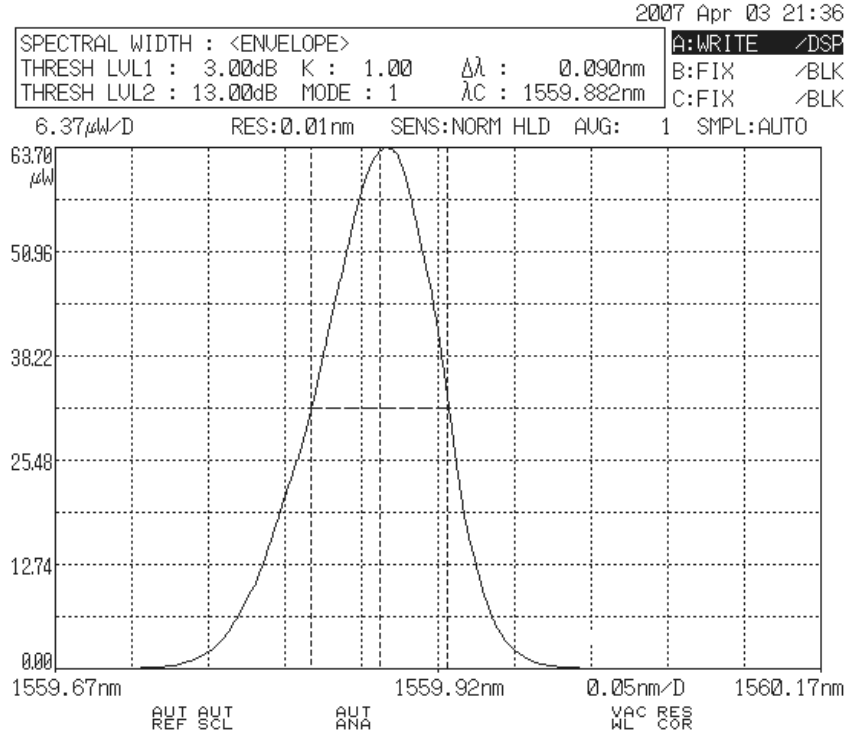


Figure 2-5: Spectrum of a home-built passively mode-locked fiber laser [1] used as a seed source.

which was phase-matched to produce 50-ps pulses at 780 nm by second harmonic generation (SHG). By focusing the input into the crystal to a waist of  $40 \mu\text{m}$  and careful optimization of the temperature we were able to convert 3.4 W of 1560 nm input into 2 W of output at 780 nm, indicating a conversion efficiency of 59%. The SHG output power is quadratic in the input power in the low efficiency regime, but linear in the high efficiency regime, as shown in Figure 2-8. Multiple dichroic mirrors were used to filter out the remaining 1560 nm light. Since we intend to use the 780 nm light to pump an SPDC source at 1560 nm with a second nonlinear crystal, it is important that the strong leftover 1560 nm light from the EDFA is almost completely filtered out with a sufficient number of dichroic mirrors after the SHG stage; we placed enough dichroic mirrors to attenuate the residual 1560 nm power to under 1 nW.

We then optimized the pump focusing for the SPDC using our earlier theoretical estimates

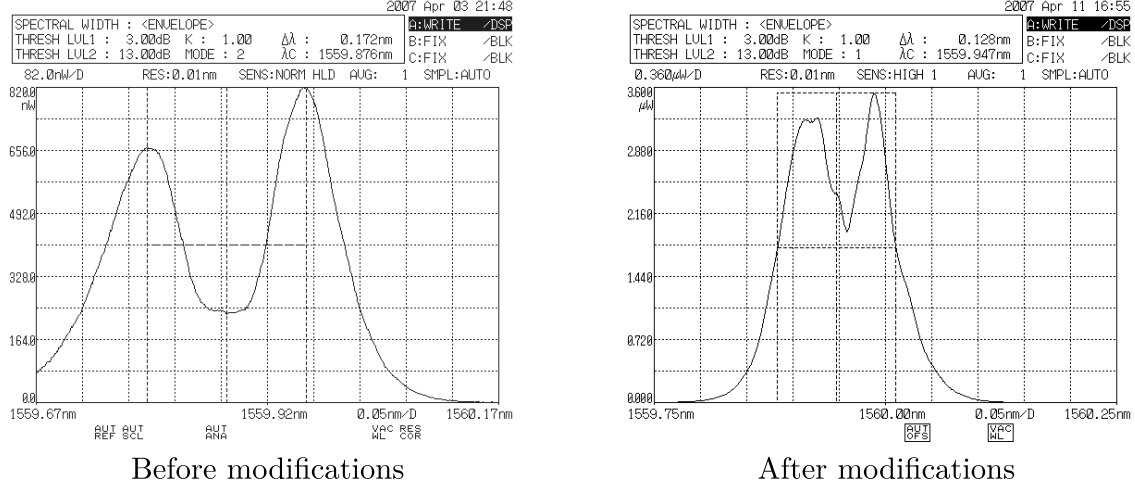


Figure 2-6: EDFA output spectrum at maximum output power setting, before and after modifications by IPG Photonics to remove excess internal fiber. The broadening of the spectrum and double peak is caused by self-phase modulation inside the fiber at high power levels.

as a starting point by focusing the pump to a waist of  $35 \mu\text{m}$ , which gives  $\xi_p = \xi_t \sim 1$ . With this focusing fixed, we optimize the coupling of the SPDC output into a single mode SMF-28 fiber, measuring the power at the other end of the fiber using a fiber-coupled InGaAs detector with 10-fW sensitivity. In order to measure the coupling efficiency, we also obtained the total SPDC output power by using a multi-mode fiber in its place. Using this initial setting, we obtained a ratio of  $\eta_T = 50\%$ . However, to account for the coupling losses and deduce the actual single-mode content of the SPDC output, we connected a single-mode 1550 nm fiber laser source to both our single- and multi-mode fiber inputs and obtained an efficiency of  $\eta_f = 82 \pm 2\%$ . Our SPDC single-mode content can then be deduced to be  $\eta_{SM} = \eta_T / \eta_f = 61 \pm 1.5\%$ .

We then varied the pump focusing and repeated the efficiency measurement at each setting. At a waist of  $w_p = 25 \mu\text{m}$  we obtained  $\eta_T = 57.5\%$  and  $\eta_{SM} = 70 \pm 2\%$  which corresponds to  $\xi_p = \xi_t = 1.7$ . One crystal shattered under tight focusing conditions as the pump power was increased, after which we subsequently avoided attempting to focus the pump too tightly as a precaution. However, as described above, later work by Bennink [29] indicates that tighter focusing may have yielded better results.

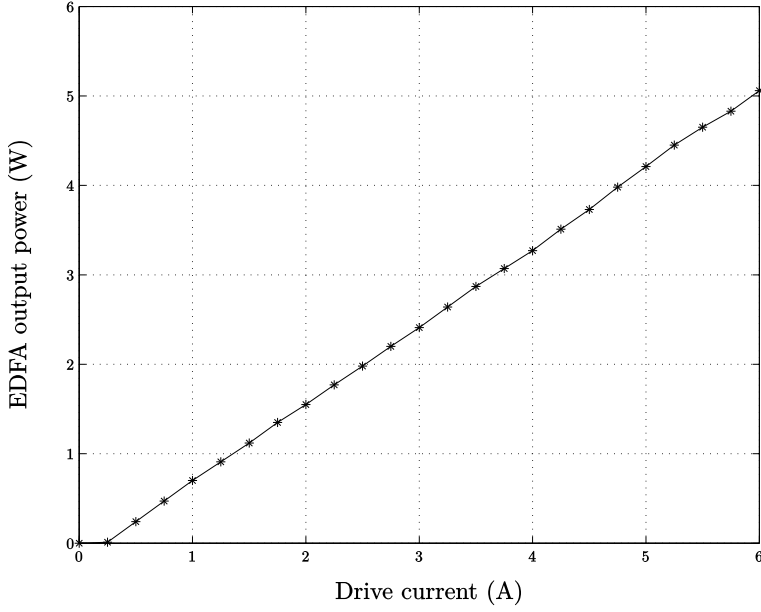


Figure 2-7: EDFA output power (1560 nm) as a function of drive current, showing linear behavior with a threshold of  $\sim 400$  mA.

### 2.2.2 SPDC under strong pumping

SPDC is traditionally used in the low-flux regime to generate biphoton and entangled photon states. However, in this experiment we are interested not in the quantum properties of SPDC but merely the phase-sensitive cross-correlations between the signal and idler. Thus, it is useful to have strong pumping beyond this low-flux regime. While in the low-flux regime, the SPDC power output is linear in the pump power, as the pump power is increased sufficiently, the SPDC output enters a regime of exponential dependence, due to the parametric amplification of the parametric fluorescence itself before exiting the crystal. This parametric amplification incidentally also breaks any entanglement properties of the SPDC outputs, but PC-OCT does not make use of quantum entanglement. In the amplified regime, the signal and reference beams continue to have classically-maximal phase-sensitive correlation which is sufficient for the experiment. Figure 2-9 shows that for our setup, we enter this regime at pump powers greater than 0.5 W - 1 W. It is also worth noting that as we enter this regime, the SPDC output bandwidth increases linearly with pump power, shown in Figure 2-10(b).

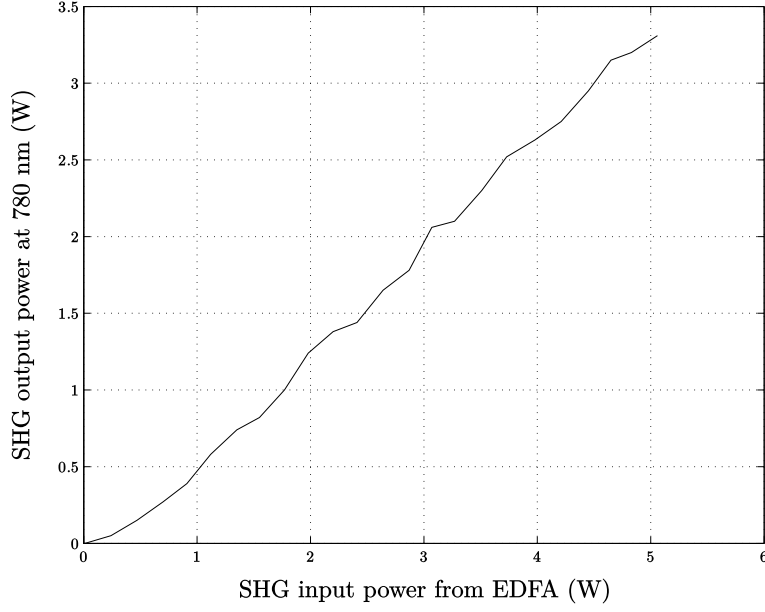


Figure 2-8: SHG output power (780 nm) as a function of input power (1560 nm), showing quadratic dependence at low power levels and linear dependence at high power levels.

## 2.3 Experimental setup

We now turn to using our SPDC-based phase-sensitive light source to demonstrate PC-OCT, with the setup shown in Figure 2-11. We devised a method to interrogate the same sample twice with phase conjugation, a physical simulation of sample dispersion using a long fiber spool to demonstrate dispersion cancellation, a classical interferometric measurement, and an automated positioning and data collection system.

### 2.3.1 SPDC source

We coupled the SPDC light previously described into the input of a 4-channel JDS Uniphase course wavelength division multiplexer (CWDM) with center wavelengths at 1530 nm, 1550 nm, 1570 nm, and 1590 nm, with nearly flat-top passbands of 16 nm at each channel, as shown in Figure 2-12. We used the 1550 nm channel as the reference and the 1570 nm channel as the signal.

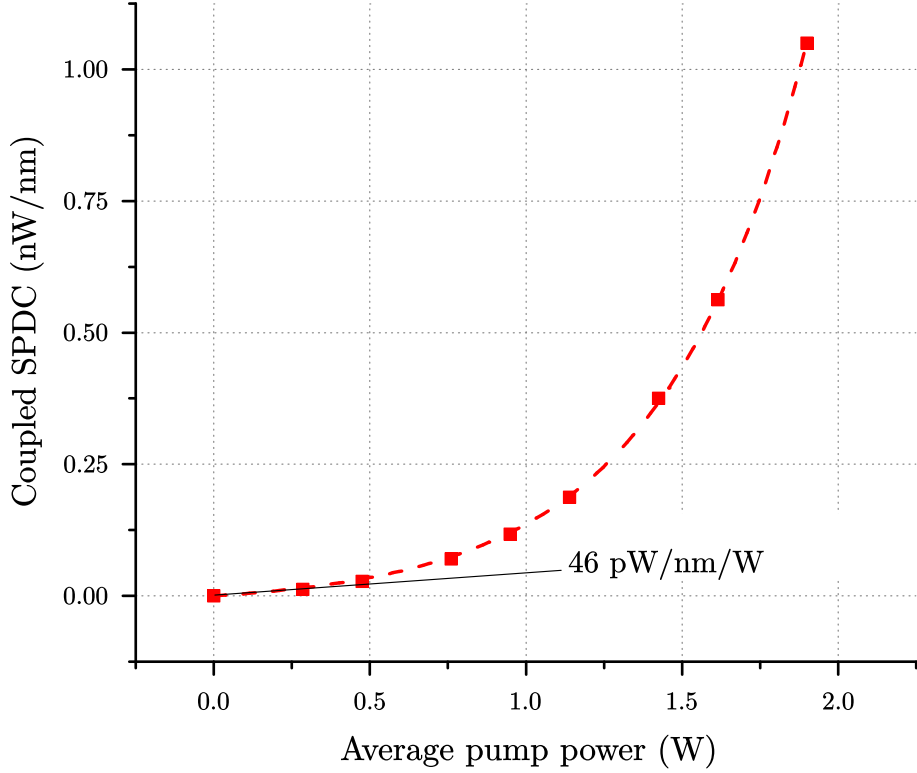


Figure 2-9: SPDC output power as a function of pump power, showing the linear dependence in the low-flux regime and exponential dependence in the high-flux (amplified) regime.

### 2.3.2 Double-pass configuration and phase conjugation

PC-OCT requires that the signal light passes through the same target twice before an interference measurement with the idler beam. We accomplished this double-pass configuration using a polarizing beamsplitter (PBS) and quarter-waveplate as shown in Figure 2-11. We first sent the 1570-nm light from the first CWDM to a second CWDM that is configured in reverse (i.e., light was injected into the 1570 nm channel and exited at the common port). We then collimated the output and configured it to be horizontally polarized using polarization control paddles. The horizontally polarized light then passed through a polarizing beamsplitter (PBS) unreflected, followed by a quarter-waveplate, leaving it in a circular polarization before interacting with the target. The reflected light passed through the same waveplate on the return path, converting it to a vertical polarization, which upon returning

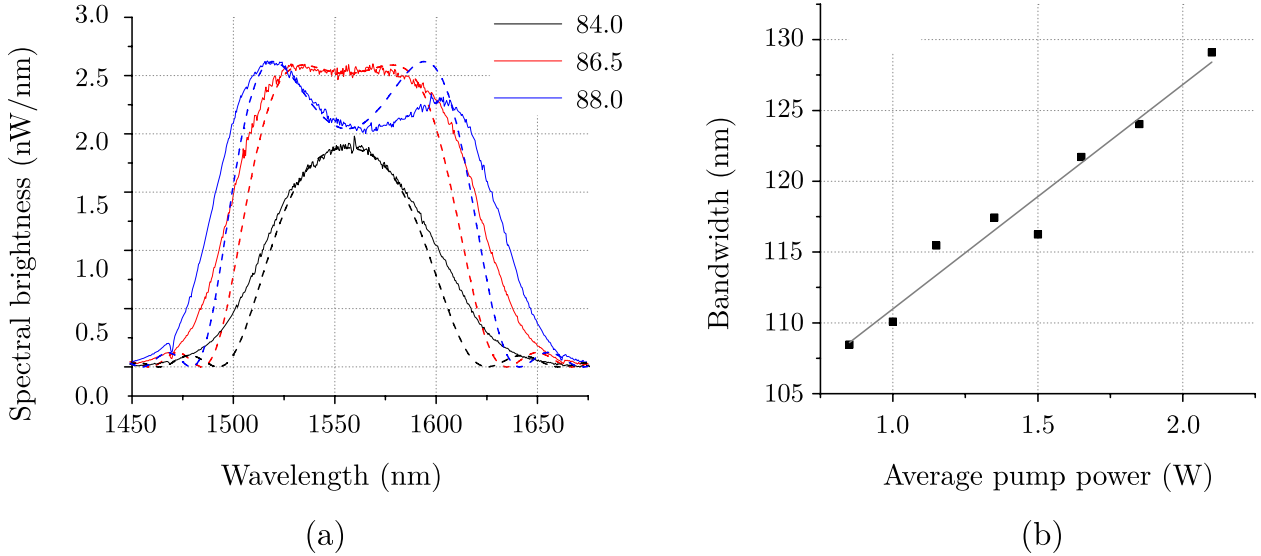


Figure 2-10: (a) Power spectral densities (solid) and theoretical models based on Sellemeier coefficients (dashed) for various crystal temperatures, with pump power fixed at 2 W. (b) Linear dependence of SPDC output bandwidth as a function of pump power, with temperature fixed at 86°C.

to the PBS was reflected into an optical parametric amplifier (OPA) which performed the phase conjugation using a third MgO:PPLN crystal of the same poling period. Parametric amplification necessitates that the pulsed pump light and the pulsed return signal are matched in time, which we accomplished by re-using the residual 780 nm pulsed pump signal from the second (SPDC) crystal with a free-space variable delay. In this experiment, the 50-ps pump pulse limited the range of targets to a maximum axial displacement of  $\sim 15$  mm, beyond which parametric amplification would not occur, although it is in principle possible to translate the pump and target simultaneously to accommodate larger ranges.

The reflected, phase-conjugated light then followed the entire optical path in reverse and was re-coupled back into the second CWDM. Since the OPA was pumped at 780 nm, the wavelength of the phase-conjugated beam was 1550 nm and exited the second CWDM from its 1550 nm port, ready for interference measurement with the 1550 nm reference arm.

We additionally installed fiber-coupled filters on both reference and signal (after conjugation) arms. The filters have Lorentzian spectral profiles with widths of  $\Delta\lambda = 0.36$

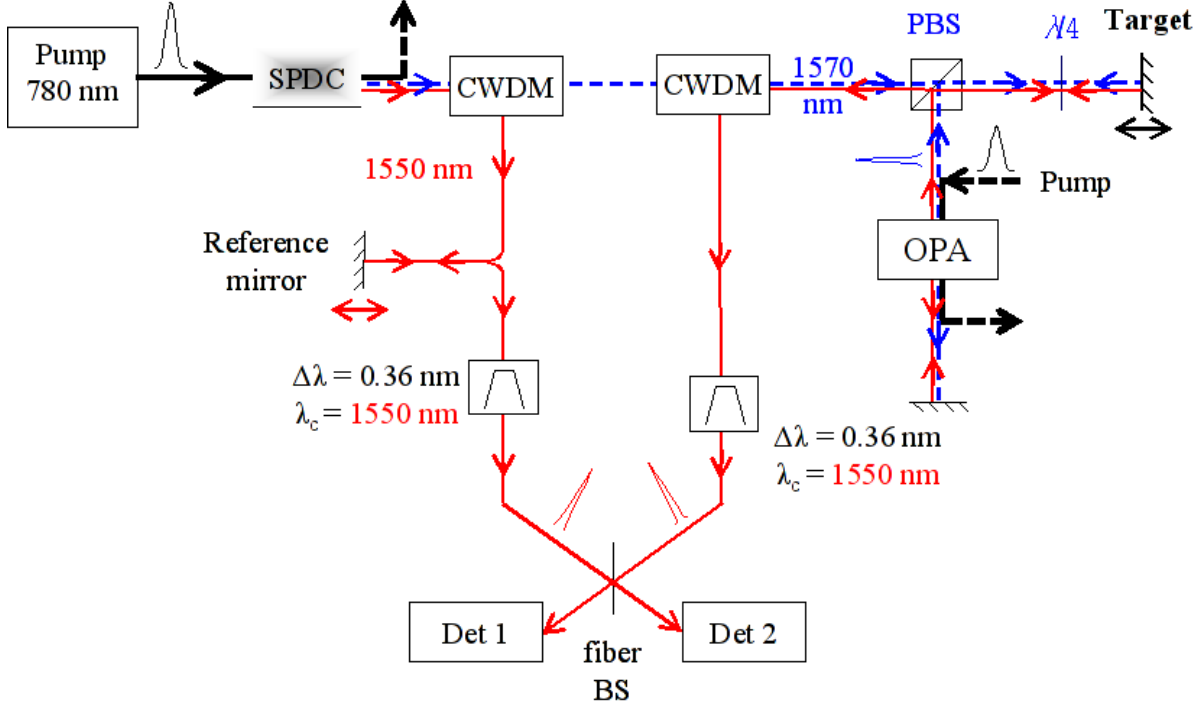


Figure 2-11: PC-OCT experimental setup. CWDM: course Wavelength division Multiplexer, OPA: optical parametric amplifier, PBS: polarizing beamsplitter.

nm and tunable center wavelengths near 1550 nm, and transmission of  $\sim 45\%$ , setting the measurement bandwidth narrow enough for signal and idler beams to be transform-limited.

### 2.3.3 Dispersion simulation using long fiber spool

At the pulse width of 50 ps we used in our experiment, typical free-space optics cannot easily provide sufficient dispersion to test the even-order dispersion-cancelling properties of PC-OCT; however, sample dispersion becomes a significant issue for OCT experiments involving thick samples and femtosecond lasers. For testing purposes, we simulate sample dispersion by inserting  $\sim 50$  meters of SMF-28 fiber (with a dispersion of 17 ps/nm/km) in the signal arm. In the reference arm, we do not wish to deliberately induce dispersion, but it is necessary to match the optical path length of the signal arm in order to perform an interferometric measurement. Since zero dispersion fiber is not widely available, we used

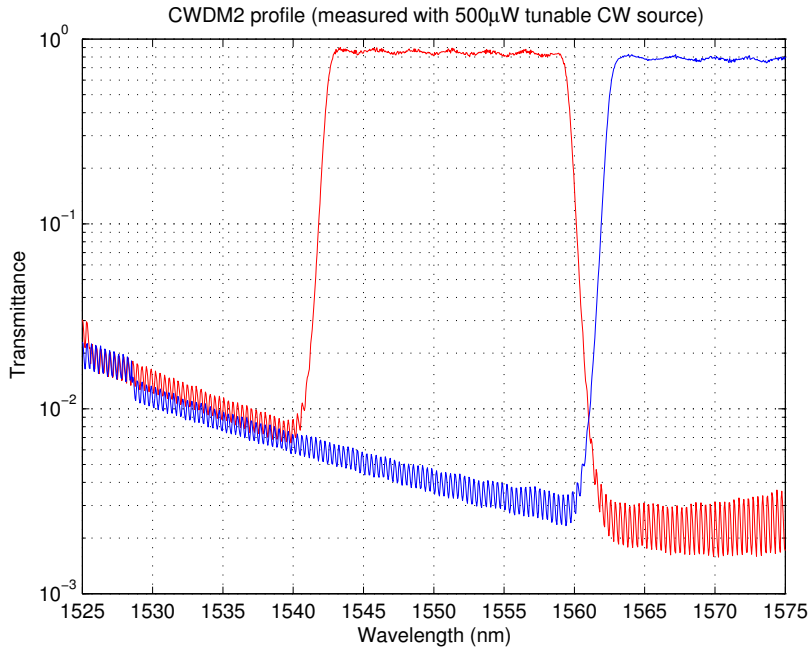


Figure 2-12: Transmittance of 1550 nm and 1570 nm channels of the CWDM, scanned using a InGaAs detector and tunable fiber-coupled laser with a maximum wavelength of 1575 nm, showing nearly flat-top transmission and sharp falloff, allowing the reference and signal to be efficiently separated.

Corning LEAF fiber, a widely-available nonzero dispersion-shifted fiber commonly used for telecommunications with a dispersion of  $\sim 4 \text{ ps/nm/km}$  at 1560 nm. Although this dispersion will not be cancelled by PC-OCT, it is much lower than the SMF-28 fiber used in the signal arm. The reference arm needed a total of 135 m of LEAF fiber to match the total optical length of SMF-28 in the signal arm. This length was measured by injecting pulses into both arms and performing time-of-flight measurement using high-speed InGaAs photodetectors.

We observed that the index of refraction of fiber was significantly affected by changes in the ambient temperature; the fluctuations in room temperature by  $\pm 1^\circ\text{C}$  were enough to cause several millimeters of difference in effective optical length after the  $\sim 135$  m of fiber length used in the experiment. We confirmed this by monitoring the changes in room temperature, as shown in Figure 2-13, and alleviated the problem by placing the bulk of the fiber spool inside a thermally-insulating foam container, performing successive measure-

ments within a short time frame, and monitoring the room temperature carefully to ensure consistent measurement conditions.

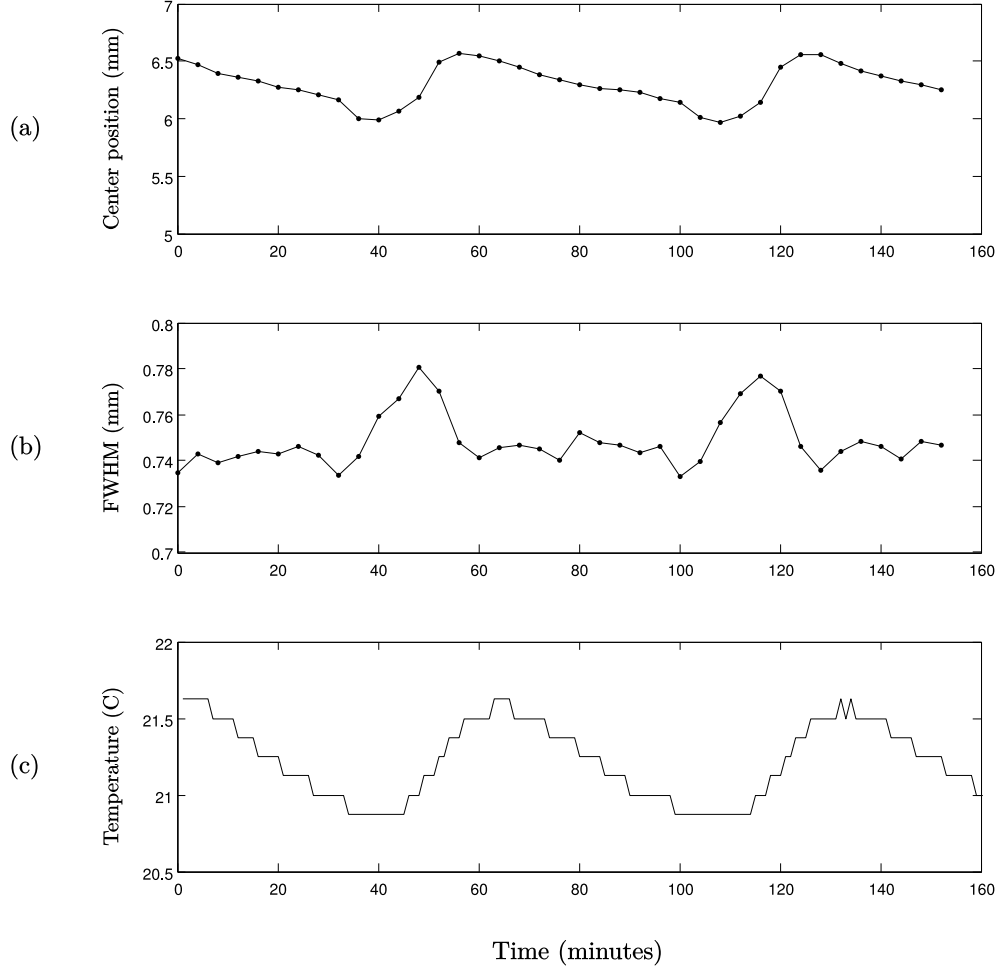


Figure 2-13: (a) Center position and (b) FWHM of the PC-OCT interferometric envelope, with (c) synchronized measurements of the ambient room temperature, showing the effect of temperature on the index of refraction of the long fibers in the experiment.

### 2.3.4 Interferometric measurement

Interferometric measurement was performed by combining both signal and reference arms using a 50/50 fiber beam splitter. A fiber circulator and free-space delay facilitated the ability to fine-tune the optical path length difference of the two arms. A constantly swept

piezoelectric transducer was added to the free-space delay in order to continuously scan the interferometer over a full wavelength at each position and measure the interference visibility. (TODO: show interference signal envelope sample)

### 2.3.5 Data collection

We connected both interferometer outputs to two channels of a high-sensitivity (0.1 pW) HP8163A InGaAs power meter, and linked to a computer via GPIB connection. A custom Visual Basic program was written to synchronously drive the PicoMotor stages and read values from both channels of the power meter. The PZT mirror was modulated at a frequency of 80 Hz, intentionally slower than the averaging time of the power meter, allowing the program to read the interference amplitude by logging a series of power values from the power meter with the stage stationed at any point. The interference amplitude was normalized to the sum of power outputs from both channels in order to compensate for laser power fluctuations.

## 2.4 Results

Using a high reflectivity mirror as a target, Figure 2-14 shows the results of three successive scans of the target with a relative separation of  $\Delta z = 450 \mu\text{m}$ . Given the double-pass configuration, one would expect the resulting peaks to have a relative separation of  $\Delta z_R = 2\Delta z$  giving us a  $2\times$  axial improvement. The observed shifts were  $920 \pm 20 \mu\text{m}$  and  $1660 \pm 20 \mu\text{m}$ , confirming this behavior; the discrepancy in the right peak from the expected  $\sim 1800 \mu\text{m}$  is likely attributable to room temperature fluctuation as described earlier. Note that this effect is particularly noticeable because of the added long fibers for inducing dispersion.

In addition to the  $2\times$  axial resolution improvement, we expect to observe cancellation of even-order dispersion in the signal arm. The expected width of the interference envelope is

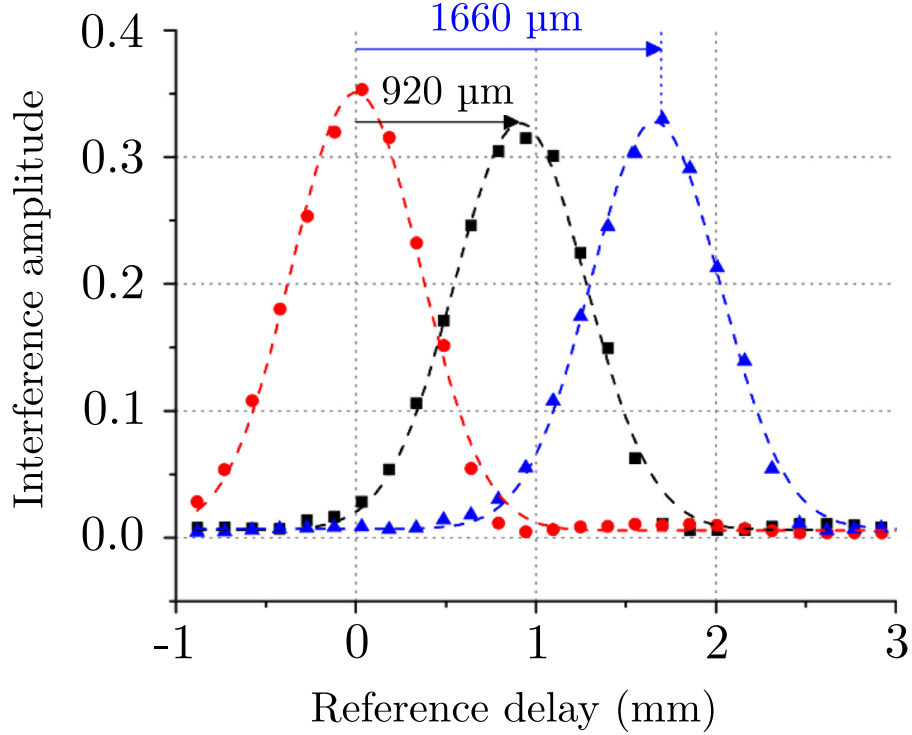


Figure 2-14: Three PC-OCT scans with a high reflectivity mirror used as a target, translated by  $450 \mu\text{m}$  between subsequent scans.

given by the convolution of the signal and reference fields, accounting for dispersion:

$$L_{OCT}^2 = 4L_0^2 + (c\Delta\lambda_F)^2(D_S(z_{S1} - z_{S2}) + D_Rz_R) \quad (2.13)$$

where  $z_{S1} = 77.1 \text{ m}$  is the length of fiber in the signal arm before conjugation,  $z_{S2} = 71.2 \text{ m}$  is the length of fiber after conjugation (leaving a net 5.9 meters of fiber in which dispersion is not cancelled in the signal arm),  $z_R = 135 \text{ meters}$  is the length of fiber in the reference arm, and  $D_S$  and  $D_R$  are the dispersion coefficients in the signal and reference arms, respectively. Since we intended to deliberately induce dispersion in the signal arm to demonstrate the dispersion-cancelling properties of PC-OCT, we used standard SMF-28 fiber which has  $D_S = 17 \text{ ps/nm/km}$ . The length of fiber in the reference arm was chosen to match the signal arm for interometric measurement; we chose not to have a significant

amount of dispersion in the reference arm, in order to demonstrate the dispersion-cancelling properties of the phase-conjugating signal arm. However, as zero-dispersion fiber was not available, we used LEAF fiber, a commonly-used nonzero dispersion shifted fiber (NZ-DSF) designed for telecommunications and with a dispersion of  $D_R = 4.2 \text{ ps/nm/km}$ . Using these values, we obtain a predicted FWHM of  $L_{OCT} = 893 \pm 30 \mu\text{m}$  which is in excellent agreement with the measured width of  $890 \pm 30 \mu\text{m}$ . If dispersion had not been cancelled, we would flip the sign of  $z_{S2}$ :

$$L_{OCT}^2 = 4L_0^2 + (c\Delta\lambda_F)^2(D_S(z_{S1} + z_{S2}) + D_Rz_R). \quad (2.14)$$

This yields  $L_{OCT} = 3.02 \text{ mm}$ , over three times larger than our measured value, suggesting that dispersion cancellation was achieved almost perfectly in the signal arm.

We see that PC-OCT recovers both of the main advantages previously associated with Q-OCT using an entirely classical setup. In addition, Erkmen showed [10] that as long as the conjugator gain  $|V|^2$  is large and reflected field strong, the signal-to-noise ratio (SNR) of PC-OCT is similar to that of C-OCT, which is expected since they employ a similar principle of operation. On the other hand, Q-OCT relies on SPDC to generate entangled photon states and thus necessitates operation at low flux and use of Geiger-mode avalanche photodetection to observe fourth-order Hong-Ou-Mandel interference, which significantly limits acquisition speed and operating conditions.

PC-OCT owes its resolution advantage to its double-pass configuration. However, an intimate relationship between this and Q-OCT can be seen in Abouraddy's interpretation of Q-OCT [4] which accounts for the  $H^*(\Omega)H(-\Omega)$  term as a product of an actual sample illumination and a virtual sample illumination, which in PC-OCT is manifested in two successive illuminations. PC-OCT's double-pass configuration providing an axial advantage over C-OCT also leads us to consider the possibility of C-OCT in a double-pass configuration, with phase-insensitive sources and no phase conjugation. In this case, although a resolution advantage would be obtained, even-order dispersion would be doubled instead of cancelled [9].

## 2.5 Conclusions

Recent developments in quantum optics have led to new methods in sensing that involve entangled biphotons and other nonclassical states of light to achieve advantages over their conventional counterparts. In particular, Q-OCT uses quantum interferometry to achieve a two-fold resolution improvement and even-order dispersion cancellation over C-OCT. Although these advantages have been proposed and demonstrated, we begin to question the true nature of the claimed advantages of these quantum techniques, whether those advantages are truly quantum in nature, and moreover, if there is an unconventional classical method to achieve the same results.

In particular, we demonstrate experimentally through PC-OCT that Q-OCT's advantages, although realizable using quantum interferometry, arise from the phase-sensitive cross-correlations in the signal and idler beams and are realizable using a novel classical technique. In addition, PC-OCT is operable at much higher light levels and acquisitions may be performed extremely rapidly, incorporating the best advantages of classical sensing.

In this work, we also address the experimental implementation issue of PC-OCT. Most classical light sources have only phase-insensitive cross-correlations and no phase-sensitive cross-correlations. Our setup requires strong and broadband phase-sensitive cross-correlations between signal and idler beams, which in principle can be produced by splitting a laser beam and imposing anti-correlated phase noises on both beams using modulators. However, in this work, we demonstrate an approach that employs nonlinear optics, which provide a bandwidth significantly higher than can be achieved using modulators. We consider the SPDC sources used to generate biphoton states with phase-sensitive cross-correlations for quantum optics experiments, but operated in a strong-pump, high-flux regime in which photons are amplified before exiting the crystal. Although this destroys their entanglement properties, the phase-sensitive cross-correlations are preserved perfectly which is sufficient to implement PC-OCT, which makes no use of quantum interference. We implemented such a source and carried out a PC-OCT experiment, demonstrating the realizability of strong, phase-sensitive classical light sources which, while unconventional, are not beyond the limits of classical physics, and

may be useful for a variety of other sensing applications.



# Chapter 3

## Classical phase-sensitive ghost imaging

In the previous chapter, we explored the benefits afforded by quantum OCT over classical OCT, finding that both axial resolution improvement and even-order dispersion cancellation originate not from quantum effects but rather from the phase-sensitive cross-correlations between the signal and idler photons in quantum OCT. We then constructed a classical phase-sensitive light source by using SPDC in the high-flux, entanglement-breaking regime, which we utilized to implement phase-conjugate OCT. Demonstration of phase-conjugate OCT allows us to use a classical light source and classical detection to realize the benefits of quantum OCT. However, there are other ways to construct classical phase-sensitive light sources.

In this chapter, we focus on the application of phase-sensitive light sources to ghost imaging, a transverse imaging modality that has been receiving considerable and increasing attention of late owing to its novel physical characteristics and its potential applications to remote sensing. Ghost imaging exploits the cross correlation between the photocurrents obtained from illumination of two spatially-separated photodetectors by a pair of highly-correlated, partially-coherent optical beams. One beam, referred hereinafter as the signal beam, interrogates a target (or sample) and then illuminates a single-pixel (bucket) detector

that provides no spatial resolution. The other beam, which we refer to as the reference beam, does not interact with the target, but it impinges on a scanning pinhole detector or a high-resolution camera, hence affording a multi-pixel output. The term “ghost imaging” refers to the fact that neither photocurrent alone yields a target image, and that the object lies in an arm with no spatially-resolving detectors, but cross-correlating the two photocurrents does produce an image of the object.

A basic schematic of the concept of ghost imaging is shown in Figure 3-1. Pittman et al. realized the first such ghost imaging experiment [31] using an entangled pair of signal and idler photons, with an bucket detector on one arm and a spatially-resolving detector on the other arm, showing that it was possible to image an object placed in the arm with no spatial resolution by counting the coincidences between the two detectors. At the time, this was interpreted as a quantum phenomenon, owing to the entanglement of the two photons. However, subsequent experiments by Valencia et al. [32] and Ferri et al. [33] demonstrated ghost imaging using thermal light, a gotating ground-glass disk and a beamsplitter, generating correlated intensity fluctuations in two arms. Abouraddy et al. analyzed the role of entanglement in several two-photon imaging configurations using quantum descriptions of the optical fields [34, 35]. The disparity between the theories of thermal-light ghost imaging experiments at the time, which use semiclassical descriptions of the field, and those using entangled photons, sparked numerous discussions about the advantages and unique properties of each [36, 37, 38], and prompting development of a unified framework to describe the fundamental physics of ghost imaging.

Erkmen and Shapiro developed such a unified theory of ghost imaging with Gaussian-state light [2] that encompasses both biphoton and pseudothermal light sources. In the case of SPDC, a nonclassical phase-sensitive cross correlation between the signal and idler photons is exploited to achieve the ghost image; in the case of pseudothermal light sources, it is the phase-insensitive cross correlation between the two arms as imposed by the ground glass diffuser that produces the ghost image. However, they also showed the possibility of using unconventional, classical phase-sensitive light sources to achieve ghost imaging. In this

chapter, we implement such a system by using spatial light modulators (SLMs) to impose phase-sensitive correlations between the two arms.

In this chapter, we implement such a phase-sensitive classical source and demonstrate the first phase-sensitive classical ghost imaging experiment, and similar to PC-OCT, showing that phase-sensitive coherence is not unique to quantum sources.

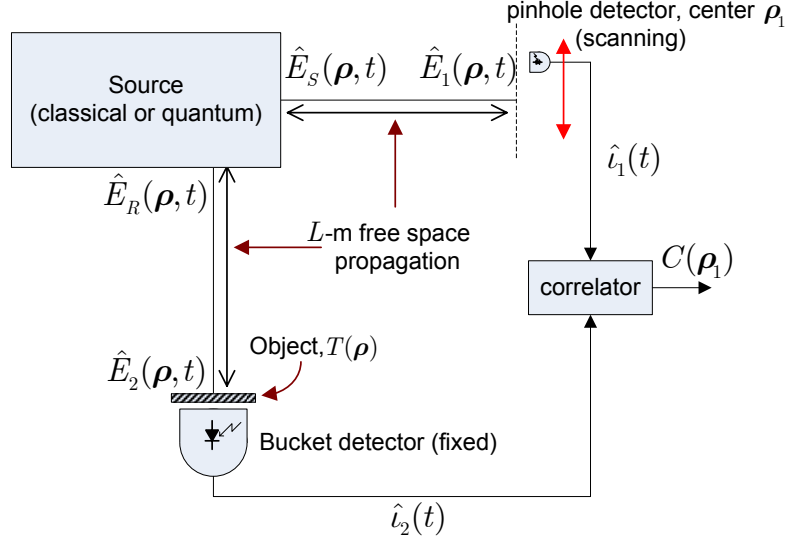


Figure 3-1: Conceptual ghost imaging schematic, reproduced from Erkmen et al. [2].

### 3.1 Near- and far-field ghost imaging

Erkmen and Shapiro extensively analyzed ghost imaging for the case of jointly-Gaussian signal and reference fields and explored both the near field, where diffraction effects are negligible, and far-field propagation where diffraction spread is dominant. For phase-insensitive coherence propagation, in which the phase patterns of the signal and reference fields are directly correlated (such as the signal and reference arms generated by a rotating ground glass followed by a beamsplitter), the difference between near-field and far-field regimes is

defined by a single Fresnel number,

$$D_0 = \frac{k_0 \rho_0 a_0}{2L} \quad (3.1)$$

where  $k_0$  is the  $k$ -vector magnitude,  $a_0$  is the coherence radius at the source,  $\rho_0$  is the transverse coherence radius, and  $L$  is the propagation distance to the target, where  $D_0 < 1$  indicates being in the far field and  $D_0 > 1$  indicates being in the near field [2].

However, for phase-sensitive propagation, in which the phases of the signal and reference beams are anticorrelated at the source plane, the near and far field regimes are defined by two Fresnel numbers: the Fresnel number for diffraction of the coherence length,

$$D_N = k_0 \rho_0^2 / (2L) \quad (3.2)$$

and the Fresnel number for diffraction of the intensity radius,

$$D_F = k_0 a_0^2 / (2L) . \quad (3.3)$$

For SLM-based ghost imaging, we assume low coherence where  $\rho_0 < a_0$ . In this case for phase-sensitive imaging the near-field regime is defined by  $D_N > 1$  and the far-field is defined by  $D_F < 1$ , which is more stringent than the condition for phase-insensitive light [2].

Erkmen and Shapiro showed that in particular, for a transmission mask  $T(\rho)$  used as an object, the phase-insensitive far-field ghost image signature is proportional to  $|T(\rho)|^2$ , whereas the phase-sensitive far-field ghost image signature is proportional to  $|T(-\rho)|$  [2]. Thus, for phase-insensitive light we obtain an upright ghost image whereas in the phase-sensitive case we obtain an inverted ghost image. The inverted far-field ghost image is also characteristic of ghost imaging with biphoton sources which also produce only phase-sensitive cross correlations.

## 3.2 Ghost imaging with spatial light modulators

Similar to our work in PC-OCT described in the previous chapter, we now turn to the implementation of a classical source of signal and reference beams with phase-sensitive cross-correlations in multi-spatial modes that is suitable for ghost imaging. We achieve this by splitting an ordinary continuous-wave laser beam using a 50/50 beamsplitter and imposing computer-generated pseudorandom phase patterns using a pair of synchronized spatial light modulators. By imposing identical phase patterns on the two SLMs we obtain phase-insensitive cross-correlations; by using opposite phase patterns on the two SLMs we obtain phase-sensitive cross-correlations between the two beams.

### 3.2.1 SLM: Principle of operation

There are two main principles of operation that are used in phase-modulating SLMs today: deformable mirrors, which selectively deform spatial regions over an optical wavelength, and liquid crystal arrays, which exploit electric field-dependent birefringence to impose a phase pattern. SLMs based on deformable mirrors (such as those sold by Boston Micromachines) are insensitive to the polarization of the input beam, may operate at very high modulation frequencies (often in the range of tens of kHz), but may suffer from much higher cross-talk between adjacent pixels because they are mechanically linked. On the other hand, those that are liquid-crystal based (such as those sold by Boulder Nonlinear Systems and Hamamatsu) suffer less cross-talk, but only modulate a single polarization axis and are limited to much slower speeds, typically no higher than 50-200 Hz. In this work, we use a liquid crystal-based Boulder Nonlinear Systems Model P512 SLMs which have  $512 \times 512$  pixels with individually addressable phases. The array size is  $7.68 \times 7.68$  mm with a pixel fill factor of 83.4%.

### 3.2.2 Pitfalls

Tests on the P512 SLMs revealed a number of nonidealities. First, although specified to have a maximum switching frequency of 10-30 Hz, we found that this is highly dependent

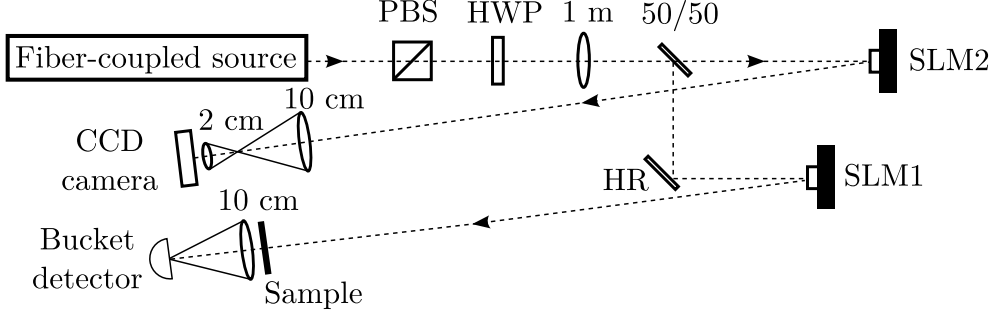


Figure 3-2: Pseudothermal SLM-based ghost imaging setup which can be operated in either phase-sensitive mode (anti-correlated SLM phase patterns) or phase-insensitive mode (identical SLM phase patterns).

on the phase stroke: while a smooth ramp from a phase of 0 to  $2\pi$  is accomplishable at upwards of 30 Hz, a sudden step transition from 0 to  $\pi$ , for example, may require  $\sim 0.3$  seconds to settle. Thus, for the purpose of implementing ghost imaging in which we impose uniformly-distributed random phases, we choose to limit the frame rate to about 2 Hz. The limits of the SLM may in fact be better characterized by an analog bandwidth rather than a maximum switching frequency.

Second, the fill factor of the P512 SLMs is 83.4%, with the behavior of the "dead" regions unspecified. Using a lens to image the SLM surface onto a camera using a polarizer for phase analysis, we found that the dead regions had high cross-talk with adjacent pixels, which may result from falloff from the electric field of the active regions of those pixels.

Third, although the voltage-to-phase calibration provided by Boulder Nonlinear Systems was reasonably accurate for the center region of the SLM, we found that the full SLM surfaces deviated from being flat by as much as a few wavelengths. Xun and Cohn also documented similar distortions in a Boulder Nonlinear Systems SLM [39]. Although in principle a per-pixel calibration could be done, we mitigate this issue by using only the center  $128 \times 128$  pixels of the SLM where the calibration is reasonably consistent.

### 3.3 Experimental setup

Figure 3-2 shows our experimental setup. A 10-mW,  $\lambda_0 = 795$  nm, laser beam was divided by a 50-50 beam splitter into signal and reference, each of which was focused to form a  $w_0 \approx 200 \mu\text{m}$  beam waist at its respective liquid-crystal SLM. The polarizing beam splitter and half-wave plate ensured that the SLMs' illumination was vertically polarized. The SLMs (Boulder Nonlinear Systems) have  $512 \times 512$  pixels (each  $15 \times 15 \mu\text{m}$ ) with individually addressable phases. A control computer generated a  $128 \times 128$  array of uniformly-distributed random phases (on  $[0, 2\pi]$ ) that were applied to the central  $128 \times 128$  pixels of SLM1 to modulate the signal beam with a  $\rho_0 = 7.5 \mu\text{m}$  coherence radius that is much smaller than  $w_0$ . We programmed SLM2 synchronously with the same phase pattern as SLM1 for phase-insensitive cross-correlations, or with its complement for phase-sensitive light. We estimate a phase accuracy of  $\sim 20$  mrad for most cases, with a few small intervals (close to the zero phase end) where we were only able to successfully calibrate to within 50-100 mrad of precision. We generated and updated the SLMs' phase patterns at 2 Hz.

Theory [2] shows that phase-sensitive and phase-insensitive correlations propagate differently, but  $D_F \equiv \pi w_0^2 / \lambda_0 L \ll 1$ , with  $L$  being the propagation distance, is sufficient for both to be in their far fields. We used  $L = 80$  cm from SLM1 to the object, so that  $D_F \approx 0.2$ , hence allowing a comparison of far-field phase-sensitive and phase-insensitive ghost images. A 10-cm focal length, 5-cm diameter lens in the signal arm focused the light transmitted through the object on a standard photodetector. An identical 10-cm lens, placed in the reference arm  $L = 80$  cm from SLM2, served as the objective for a telescope with a 2-cm focal length eyepiece. This telescope was adjusted to produce a  $\sim 5.7 \times$  minified image of the speckle pattern at the objective plane. The camera was a shutterless Basler Pilot charge-coupled device (CCD) with  $1600 \times 1200$  pixels, each  $7.4 \times 7.4 \mu\text{m}$  in size with 12-bit dynamic range. We adjusted the CCD exposure and gain parameters to minimize the occurrence of vertical blooming [40], which would degrade the image quality. Figure 3-3(a) displays a typical single-shot CCD image of the far-field speckle pattern in the reference arm produced by one of the random phase patterns at SLM2. The observed  $\sim 1$  mm speckle radius at

the objective lens is consistent with the expected far-field coherence radius,  $\rho_L = \lambda_0 L / \pi w_0$ . The expected spatial extent of the speckle pattern, set by the  $2\lambda_0 L / \pi \rho_0 \approx 57$  mm intensity diameter, is slightly larger than the 50-mm lens mount's circular aperture that is visible in Fig. 3-3(b).

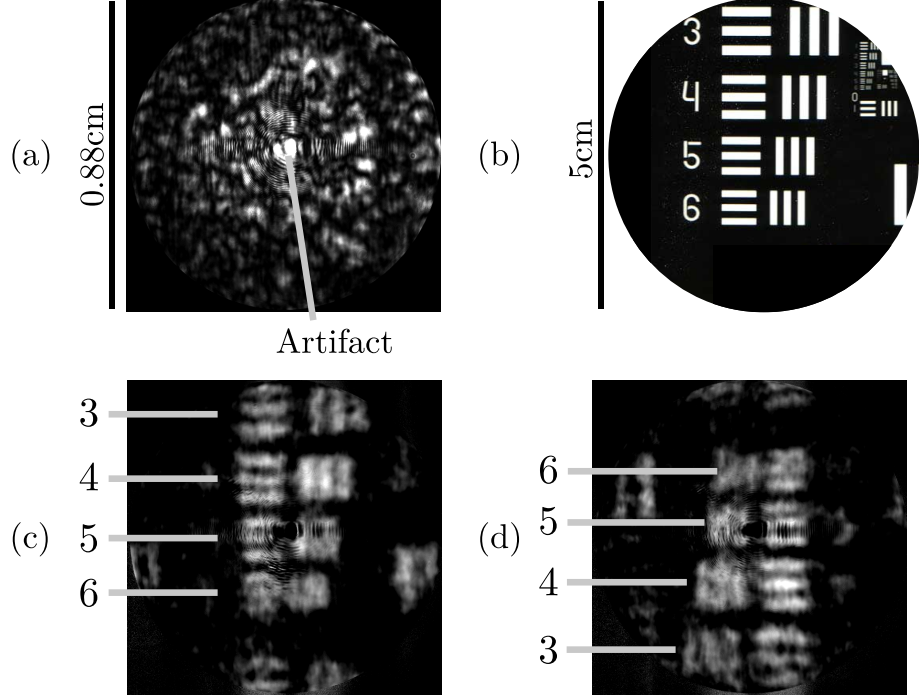


Figure 3-3: (a) Sample single-frame speckle pattern as imaged by the CCD. The artifact in (a) is due to the SLMs' inter-pixel dead space. (b) Portion of a USAF spatial-resolution transmission mask used as the object. (c) Phase-insensitive and (d) phase-sensitive far-field ghost images, each averaged over 18640 realizations.

The bright central spot in the Figure 3-3(a) speckle pattern is an artifact that prevented ghost-image formation in that region. We have traced the artifact to three potential problems in our experimental setup. First, the SLM phase patterns must be uniformly distributed over  $[0, 2\pi]$ . Second, the polarization of the incident beam must exactly match the active axis of the SLM. Any phase bias or polarization misalignment gives rise to a brighter center spot, but we were able to resolve these two problems by careful SLM calibration and polarization alignment, respectively. The third effect that we observed experimentally as well as confirmed by computer simulation, is that our SLMs are limited by a sub-optimal,  $\sim 83\%$  pixel fill factor.

The inter-pixel dead space behaves much like a 2-D diffraction grating, creating a grid of spots in the far field including a prominent zero-order spot at the center.

We used elements 3, 4, 5, and 6 from group 2 of a 1951 U.S. Air Force (USAF) resolution transmission test mask as our object, as shown in Fig. 3-3(b), and placed it just before the 10-cm lens in the signal arm. The bucket detector and CCD outputs were fed in real-time to the control computer, which averaged the outputs from a sequence of SLM phase patterns to compute the cross-covariance between each CCD pixel and the bucket detector. Although the cross-correlation between the CCD pixels and bucket detector contains a high DC background which is present in classical-state ghost images [2, 41], we obtain a high-contrast ghost image of the object by computing the cross-covariance.

### 3.4 Results

Figures 3-3(c) and (d) show the measured phase-insensitive (in-phase SLMs) and phase-sensitive (anti-phase SLMs) ghost images of the test object (Figure 3-3), each obtained by averaging over 18640 random phase-pattern realizations. The only change made to the setup in transitioning from phase-insensitive to phase-sensitive ghost imaging was to switch the SLM1 and SLM2 patterns from in-phase (same phase) to anti-phase operation. The image inversion in the phase-sensitive case is in accord with theory [2, 41] for phase-sensitive classical or quantum light sources. Figure 3-4 shows another example of image inversion between far-field phase-insensitive and phase-sensitive ghost imaging—here for an MIT-logo object—obtained using 7000 random phase-pattern realizations.

Figures 3-3(c) and (d) show comparable spatial resolutions for the phase-insensitive and phase-sensitive ghost images. The known spacings for the markings on the USAF test mask allow us to evaluate that resolution. In particular, the line spacings for elements 3 and 4 (the largest two elements) are well separated, but those for elements 5 and 6 are less discernible. We thus estimate the spatial resolution to be approximately equal to the spacing between lines in element 4, which is 1.42 mm. This value is in good agreement with theory [2], which shows that the resolution is speckle-size limited to the object-plane spatial coherence radius

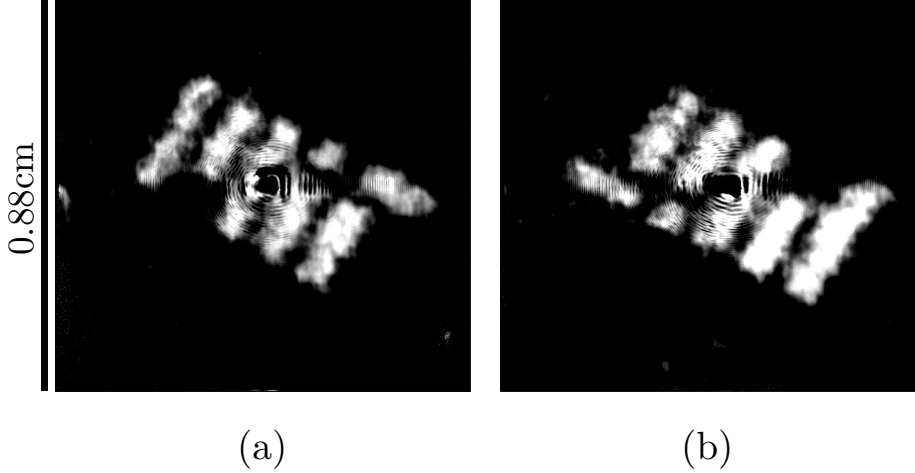


Figure 3-4: MIT-logo ghost images after 7000 realizations for (a) phase-insensitive and (b) phase-sensitive light, showing image inversion in (b). The images are individually normalized, with the noise levels clipped for improved visibility. The bright-spot artifact at the center prevents us from obtaining an image in that small region.

$$\rho_L \approx 1.0 \text{ mm.}$$

The signal-to-noise ratio (SNR) for a single pixel of a ghost image is defined as the squared-mean value of that image pixel (cross-covariance averaged over all realizations per run) averaged over multiple independent runs of the experiment, divided by the variance of the same image pixel over those runs [2]. Since a reliable SNR measurement requires the statistics from multiple independent trials, which would take a very long time with our equipment, we approximate it by averaging the SNR over spatially adjacent pixels (with similar brightness) from data in a single acquisition. We thus obtain an SNR of  $\sim 7.5$  for the phase-insensitive measurement of Fig. 3-3(c), and  $\sim 7.9$  for the phase-sensitive measurement of Fig. 3-3(d). Because we operated in the narrowband, high-brightness regime with a binary mask, the theoretical SNR for both phase-insensitive and phase-sensitive cases is  $\sqrt{2\pi}(T_I/T_0)(\rho_L^2/A_T)$  [2], where  $T_I/T_0$  is the ratio of the integration time to the source coherence time, and  $A_T$  is the mask's transmissive area. For our experiment,  $T_I/T_0 = 18640$ , the number of phase-pattern realizations, and  $A_T \approx 3.5 \text{ cm}^2$ , yielding  $\text{SNR} \approx 133$  for both cases. While the measured SNR for the phase-sensitive and phase-insensitive images are similar, as theory predicts, they are far lower than the theoretical SNR. We believe that this reduction

could be partially due to inaccuracies in calibration between SLM1 and SLM2 which would degrade the resulting ghost image. In addition, our spatial approximation may have failed due to variations in brightness at different pixels or in the far-field speckle pattern, causing the spatially-averaged SNR to reach an asymptote. We notice in tests that for lower numbers of realizations (under 2000) the spatially-averaged SNR tracks more closely the theoretical value.

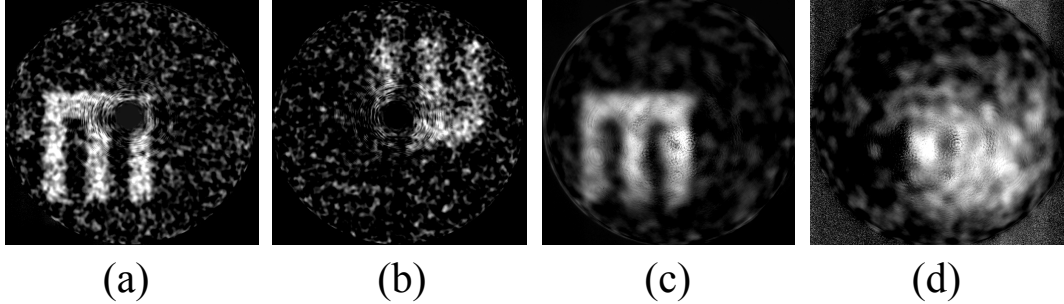


Figure 3-5: Far-field ghost imaging under loose focusing ( $w_0 = 150 \mu\text{m}$ ) for (a) and (b), and tight focusing ( $w_0 = 50 \mu\text{m}$ ) for (c) and (d), with the SLM located at a distance of  $2.75 \times$  the Rayleigh range  $z_R$ . The mask is an off-center letter M. Phase-insensitive images in (a) and (c) are not affected, but phase-sensitive measurements in (b) and (d) show degradation that is severe for tight focusing in (d).

Our experiments show that phase-sensitive ghost images are badly degraded for tightly-focused illumination when the SLMs are not located at the beam waist, where the wave front is flat. On the other hand, loosely-focused illumination makes these ghost images far less sensitive to the axial displacement of the SLM from the beam waist. For phase-insensitive ghost imaging, however, there is very little sensitivity to SLM position relative to the beam waist. These behaviors were demonstrated by using only the spatially-resolving CCD arm to simulate both the signal and reference paths as follows. In the first measurement frame we set the SLM to the reference pattern and collected a CCD image of the far-field speckle pattern. In the second frame we set the SLM to the signal pattern, imposed a mask (object) on the camera's image using software, and summed pixel outputs to simulate the bucket detector. This approach avoided potential misalignment between the two physical arms, enabling clean observation of differences between loose versus tight focusing. Figure 3-5 shows our phase-

insensitive and phase-sensitive measurements taken under loose ( $w_0 = 150 \mu\text{m}$ ) and tight ( $w_0 = 50 \mu\text{m}$ ) focusing with the SLM located  $2.75 \times$  the Rayleigh range  $z_R = \pi w_0^2 / \lambda_0$  behind the beam waist for each case. The results show that tight focusing and misplacement of the SLM caused significant degradation of the phase-sensitive ghost image. The physical explanation is that the spherical phase-front present on a mislocated SLM due to tight focusing adds the same amount of pixel-dependent phase bias to the signal and reference beams such that their phases are no longer anti-correlated. Because phase-sensitive ghost imaging requires the phases of the signal and reference beams to be anti-correlated, this pixel-dependent phase bias impairs formation of the the phase-sensitive ghost image. Phase-insensitive operation, however, only requires that the two arms have equal phases, so that identical focusing and SLM placement in both arms suffices to produce a high-quality ghost image.

### 3.5 Signal-to-noise ratio

Erkmen and Shapiro showed that the signal-to-noise ratio (SNR) scales linearly in the number of realizations and is given by [41, 42]:

$$\text{SNR} = \sqrt{2\pi} \frac{T_1}{T_0} \frac{\rho_0^2}{A_T} |T(\rho_1)|^4 \quad (3.4)$$

where  $T(\rho)$  is the field transmission mask,  $T_0$  is the coherence time,  $T_1$  is the averaging time,  $\rho_0$  is the coherence radius, and  $A_T$  is the total area over which  $T(\rho) = 1$ .  $A_T/\rho_0^2$  is the number of spatial resolution cells, and for an SLM-based experiment with discrete realizations,  $T_1/T_0$  is the number of realizations. Figure 3-6 shows a sample of an experimental SNR curve alongside the theoretical curve for a square outline used as a transmission mask, which is in good agreement until the SNR flattens at around 45, which we reach at around  $N = 3000$  realizations.

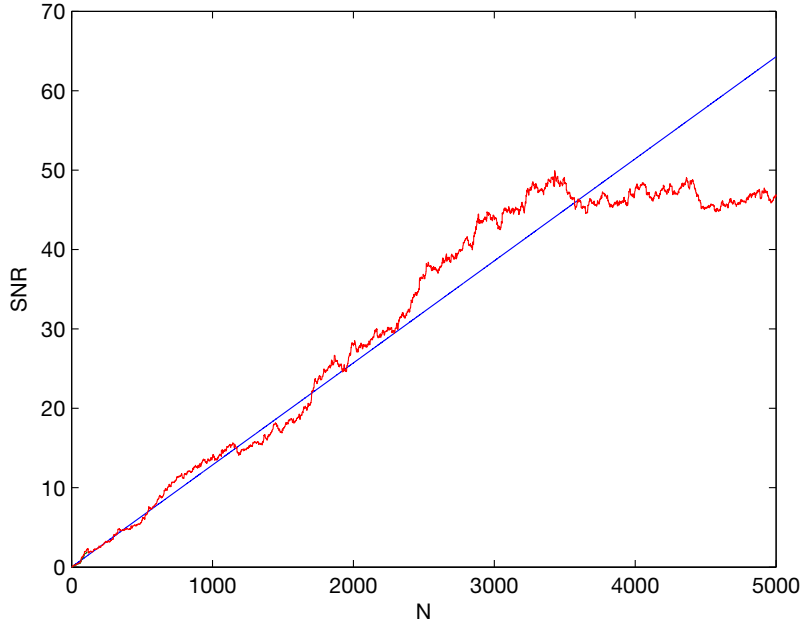


Figure 3-6: Theoretical (blue) and experimental (red) signal-to-noise ratio curves for a simple square transmission mask as a function of the number of realizations  $N$ .

### 3.6 Computational ghost imaging

In the case of pseudothermal or SPDC-generated signal and idler fields, the cross-correlations between the fields at transverse locations separated by greater than a coherence length are inherently random. However, SLM-based ghost imaging uses deterministic, pseudorandom modulations imposed by a computer. Since ghost imaging is a product of classical coherence propagation [2], we can in principle eliminate the reference arm altogether and replace it with a computational simulation of the free-space optical propagation from the SLM plane to the CCD camera plane, as proposed by Shapiro [41, 43]. As shown in Figure 3-7, this computational replacement permits us to image an object using only a signal arm, without any spatially-resolving detectors.

In order to realize this simulation, we consider the source field  $E_R(\rho, t)e^{i\omega_0 t}$  at the SLM plane of the hypothetical reference arm, which is a product of the original cw laser beam field and the phases that would have been deterministically imposed on the reference arm SLM. In

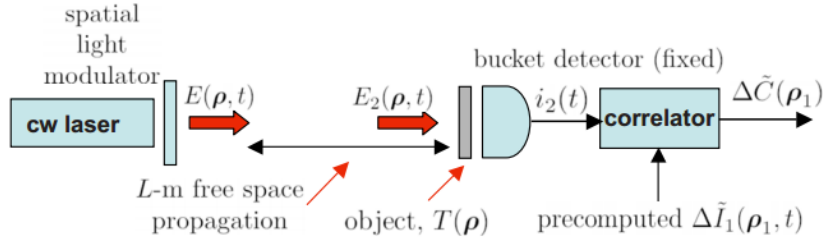


Figure 3-7: Computational ghost imaging schematic, in which there are no spatially resolving detectors and the reference arm is replaced by a computer-generated reference that is used to drive the spatial light modulator.

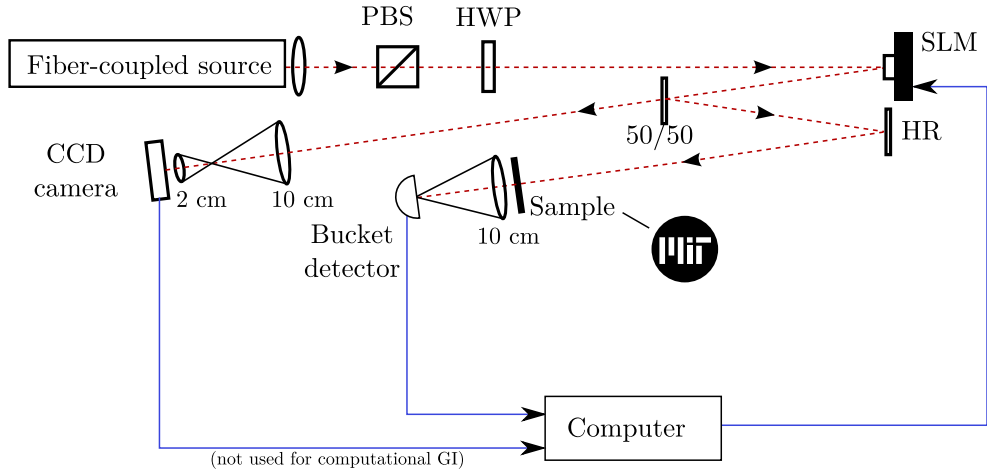


Figure 3-8: Pseudothermal, phase-insensitive ghost imaging setup used to test computational and compressed ghost imaging. In computational ghost imaging, we do not use the CCD camera.

the case of phase-insensitive ghost imaging, these would be identical to the phases imposed on the signal arm; in the case of phase-sensitive ghost imaging, they would be the negative. We assume the SLM to be a square of size  $D \times D$ , with square pixels of size  $d \times d$ . Since  $d$  is much smaller than the beam waist at the SLM, the light field can be approximated over each pixel as a plane wave. The sum of these plane waves at pixels indexed by  $n = \{1 \dots (D/d)^2\}$ , multiplied by the phases  $\phi_n(t)$  deterministically imposed on them, yields an SLM-plane field

$$E_R(\rho, t) = \sum_n \text{rect} \left( \frac{x - x_n}{d} \right) \text{rect} \left( \frac{y - y_n}{d} \right) e^{i\phi_n(t)}, \quad (3.5)$$

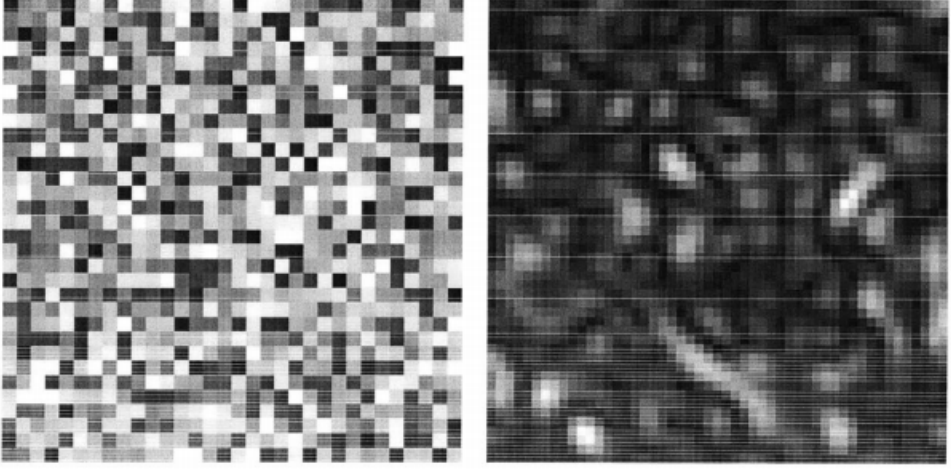


Figure 3-9: (a) Sample pseudorandom phase pattern imposed on SLM. The phase modulation at each pixel is independent and uniformly distributed on  $[0, 2\pi]$  and encoded as a greyscale value in this visualization. (b) Simulated result of the far-field speckle pattern.

where  $\text{rect}(\cdot)$  is the unit-length rectangle function. We assume quasimonochromatic paraxial diffraction over a free-space path of length  $L$  between the SLM and the CCD of the reference arm yields a CCD-plane field  $E'$  of [44]:

$$E'_R(\rho', t) = \sum_n \frac{d}{\lambda_0 L} \text{sinc}\left(\frac{x'd}{\lambda_0 L}\right) \text{sinc}\left(\frac{y'd}{\lambda_0 L}\right) e^{-ik_0(x'x_n + y'y_n)/L} e^{-ik_0(|x'|^2 + |y'|^2)/2L} e^{i\phi_n(t)} \quad (3.6)$$

where  $\rho_n = (x_n, y_n)$  is the center of pixel  $n$ .

The far-field intensity pattern which would have been recorded by the reference arm CCD is then given by  $I'(\rho, t) \propto |E'(\rho, t)|$ . Figure 3-9 shows a sample pseudorandom phase pattern with independent phase values each uniformly distributed over  $[0, 2\pi]$ , and the resulting computed far-field intensity pattern, which shows a speckle pattern with a feature size on the order of  $\rho_L$ .

We test computational ghost imaging by first switching to a phase-insensitive ghost imaging setup using a single SLM and a beamsplitter, as shown in Figure 3-8. This eliminates any differences between the behaviors of two SLM devices. We perform computational ghost

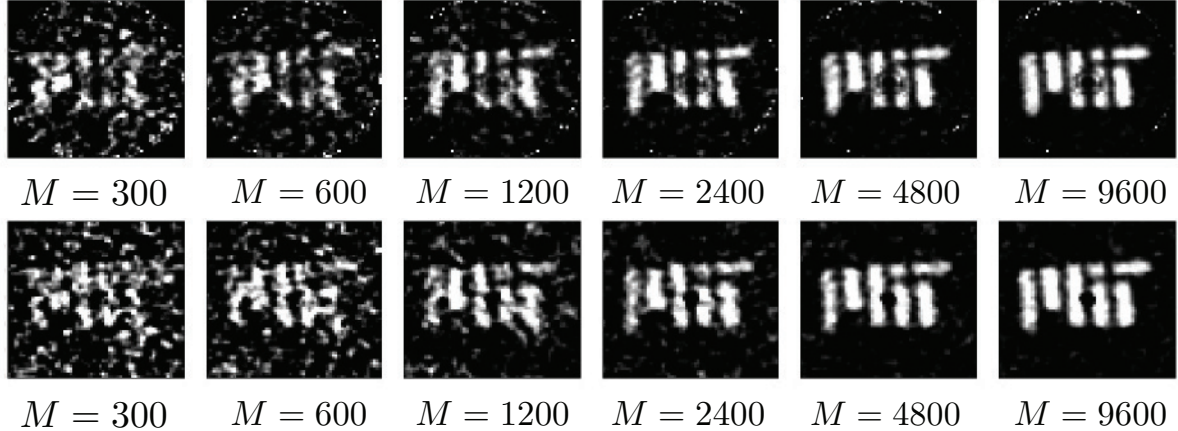


Figure 3-10: Side-by-side results of an MIT logo mask imaged using (a) traditional ghost imaging with optical signal and reference arms and (b) computational ghost imaging in which the reference arm is replaced by a computer simulation, averaged over  $M = 300$  to 9600 independent pseudorandom phase patterns.

imaging in a fashion similar to traditional ghost imaging, using this far-field intensity pattern in place of a CCD image in the reference arm. In Figure 3-10 we show side-by-side results of traditional ghost imaging and computational ghost imaging, realized over 9600 pseudorandom phase patterns, noting that the speed of image formation is similar in both cases. Bromberg et al. [45] also performed a similar experiment which demonstrated high-quality images with SNRs on par with theory for 16000 realizations.

By replacing the reference arm with a computer simulation and using only a single bucket detector in the signal arm to obtain almost identical results, we show that pseudothermal ghost imaging relies on simple classical coherence propagation, and not non-local quantum correlations as previously suggested in [? ].

Although not explored significantly in this research, computational ghost imaging can provide a number of advantages over traditional ghost imaging. First, the elimination of the reference arm allows for a simpler device; this is useful for field applications where building a reference arm of the required length would be impractical. Second, computational ghost imaging can be used to image objects at wavelengths where bucket detectors are available but CCD arrays are not. Third, the intensity patterns can be simultaneously computed at

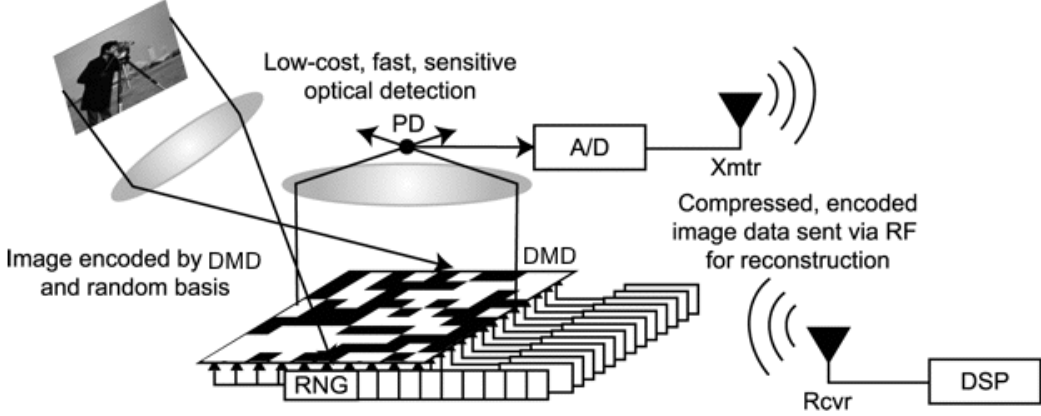


Figure 3-11: Schematic of the Rice University single pixel camera, reproduced from [3]. DMD: digital micromirror device, PD: photodetector, DSP: digital signal processor, RNG: random number generator. (TODO: add (a) and (b) to figure)

multiple depths for a single phase pattern, allowing depth-of-field effects to be exploited to gain some degree of range resolution. These advantages are discussed in detail in [41].

### 3.7 Compressed ghost imaging

We now reinstate the experimental reference arm in Figure 3-2 and consider another variation of ghost imaging, in which we focus on the processing of our results to significantly reduce the required acquisition time. In this section we make use of compressed sensing (CS) [46], a novel processing technique which has been applied to numerous fields of imaging, notably single-pixel cameras [47], whose setups are very similar in nature to signal arm of a ghost imaging setup. Katz et al. first implemented compressive ghost imaging using a rotating ground glass and a beamsplitter [48]; here we attempt to apply a similar technique to SLM-based ghost imaging.

The basic idea behind compressed sensing is that given that real-world objects exhibit some degree of spatial structure, a small number of measurements of known, random linear projections of the object contains enough information to reconstruct the object. This spatial structure is captured by sparsity in some transform basis, such as the discrete cosine trans-

form (DCT) or wavelet basis. In other words, we expect that most real-world objects have a relatively small number of nonzero coefficients in the transform basis.

Making this very realistic assumption drastically reduces our solution space, and consequently the number of measurements required for faithful reconstruction, a method first proposed by Candes et al. [46]. Rather than using averaging to slowly converge toward our solution over thousands of realizations, we instead use a relatively low number of measurements, treat the image as a solution to an underdetermined linear system, and employ computational optimization techniques to move to a solution that fits our sparsity criteria. Sparsity is usually quantified in terms of the  $\ell_1$ -norm (sum of the absolute values) of the coefficients in the transform basis [46], which allows us to employ well-known, efficient convex optimization algorithms to quickly search for a global optimum.

Compressed sensing was used by the single-pixel camera at Rice University [47], as shown in Figure 3-11. The single-pixel camera uses a digital micromirror device (DMD), whose pixels can be set to selectively reflect light, placed at the image plane of a camera, and a single-pixel photodetector to collect all the light reflected by the DMD. Although their implementation placed the DMD at the receiver, allowing it to be used with arbitrary illumination sources, the single-pixel camera could in principle be accomplished by using a custom, broadband light source and spatially modulating the illumination using the DMD (i.e. projecting known illumination patterns onto the object).

This operation of the single-pixel camera is functionally similar to ghost imaging in that a pseudorandom spatial pattern is projected onto the object and the single-pixel detector is equivalent to a bucket detector. The only difference relevant to data processing is that in ghost imaging, we are unable to arbitrarily configure the intensity pattern at the object plane; we can only configure the phase modulations at the SLM and determine the resulting far-field intensity pattern at the object plane either experimentally (using a reference arm) or by simulation (using computational ghost imaging). However, as long as we have knowledge of these patterns, we can employ the compressed sensing technique that is associated with single-pixel cameras.

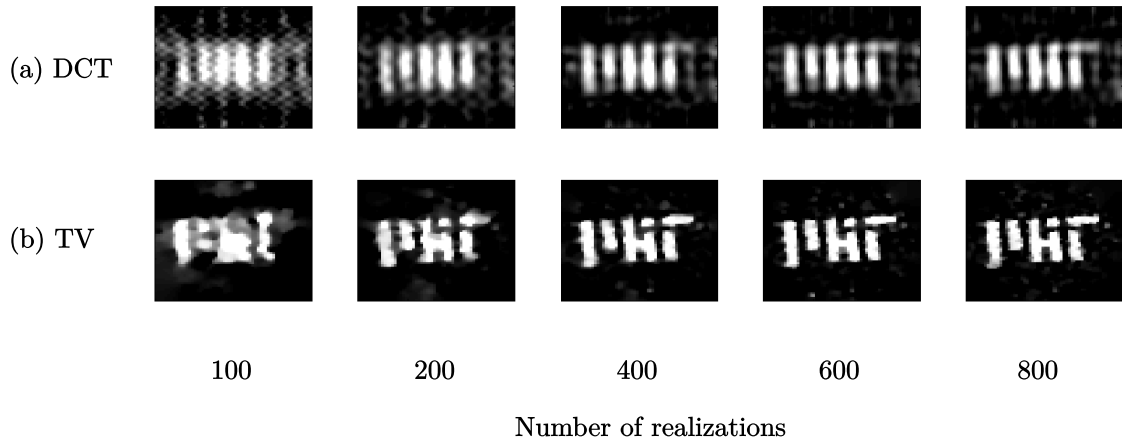


Figure 3-12: Ghost images processed using compressed sensing for a binary MIT logo mask, using (a) DCT and (b) TV sparsifying transforms.

To computationally reconstruct a  $N \times N$ -pixel image  $x_{i \in [0, N^2]}$ , we solve for

$$\hat{x} = \arg \min_x \|W\{x\}\|_1, \text{ s. t. } Ax = b \quad (3.7)$$

where  $x$  is a 1-by- $N^2$  vector representing the pixels of the image rearranged as a single column,  $A$  is a  $M$ -by- $N^2$  matrix containing  $M \ll N^2$  realizations of object-plane intensity patterns, one pattern per row and rearranged in the same order as  $x$ ,  $b$  is a  $M$ -by-1 vector that stores the resulting bucket detector measurements for each pattern, and  $W\{\cdot\}$  is a sparsifying transform (such as DCT, for example). Assuming the system operates perfectly and delivers the correct observations for  $b$ , this equation determines the sparsest solution  $x$  that satisfies the underdetermined equation system  $Ax = b$ .

However, since  $b$  will be corrupted by noise, in most experimental situations it is necessary to relax this equality constraint. We do this by solving instead for

$$\hat{x} = \arg \min_x \|W\{x\}\|_1, \text{ s. t. } \|Ax - b\|_2 < \epsilon \quad (3.8)$$

where  $\epsilon$  represents the maximum magnitude of the error in the bucket detector measurements.

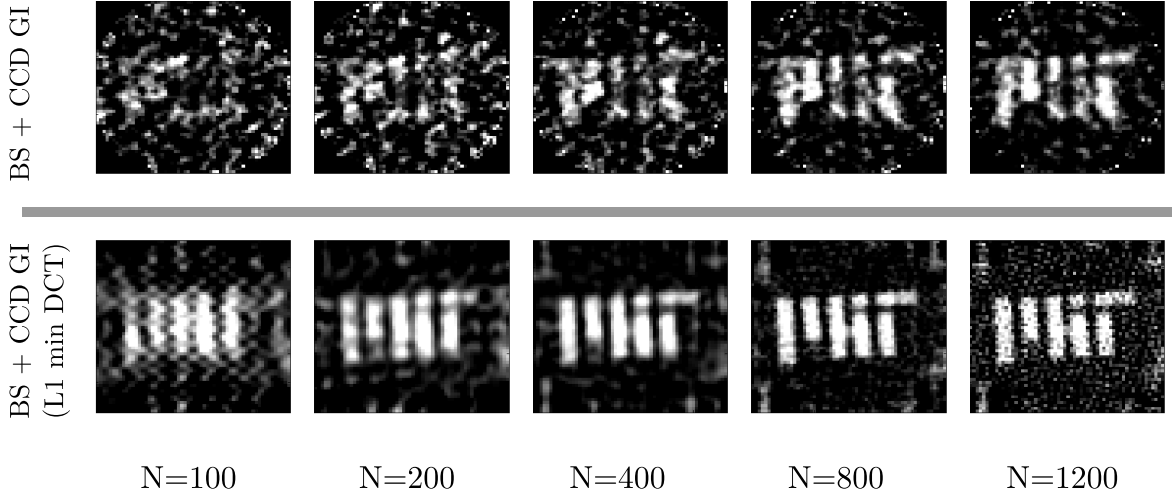


Figure 3-13: Ghost images of an MIT logo mask imaged using (a) traditional averaging and (b) compressed sensing using the same data set.

This optimization problem can be solved efficiently using convex optimization techniques. We make use of the L1-Magic [49] package for MATLAB which is designed specifically to solve this problem. Another similar method to relax the equality constraint is to solve for

$$\hat{x} = \arg \min_x \left[ \|W\{x\}\|_1 + \frac{1}{2\rho} \|Ax - b\|_2^2 \right] \quad (3.9)$$

for a tunable relaxation parameter  $\rho$  which can be solved using the YALL1 package [50] developed at Rice University.

We use the same phase-insensitive ghost imaging setup shown in Figure 3-2 and the same transmission mask of the MIT logo. Since this is a binary mask with sharp edges, we note that DCT may not be a suitable sparsifying basis because it is not localized in space and the sharp edges would excite numerous basis components. A more suitable sparsifying transform for this type of sample is based on total variation (TV), in which we solve for

$$\hat{x} = \arg \min_x \| \text{TV}(x) \|_1, \text{ s. t. } \|Ax - b\|_2 < \epsilon \quad (3.10)$$

where  $\text{TV}(\cdot)$  represents the sum of the absolute differences of consecutive pixels in the image.

This problem is also readily solved by L1-Magic [49]. Figure 3-12 shows results of ghost imaging using compressed sensing using DCT and TV sparsifying transforms, showing that TV does indeed perform better for this particular type of mask. In both cases, we scan over the relaxation parameter  $\epsilon$  to find an optimal value, as illustrated in 3-14 for the DCT case. If the constraint is too tight, artifacts originating from noise remaining in the image; if the constraint is too loose, the convex optimization routine over-smoothes the image and arrives at a solution that does not fit the data.

We also compare compressed sensing to traditional ghost image processing based on the second-order cross-correlations between the reference and bucket signals. Figure 3-13 shows side-by-side results of ghost images obtained using traditional averaging and TV compressed sensing using identical data sets. We see in this case that by 200 realizations, the image obtained by compressed sensing is already intelligible, and by 400 realizations it is clear. In contrast, the traditional averaging method is barely intelligible before 1200 realizations; in Figure 3-10 of the previous section we observed that it took several thousand realizations to form a high-quality image.

## 3.8 Computational compressed ghost imaging

We now turn to the question of whether it is possible to entirely replace the reference arm with a computational simulation, and apply compressed sensing techniques at the same time. Figure 3-15 shows sample results of applying our compressed sensing algorithm to the data set used to produce computational ghost images in Figure 3-10. We see that although there is barely some evidence of an object, we are unable to extract a usable image from this method. We were, however, able to recover images for simpler masks, as seen in Figure 3-16.

In order to debug this issue further, in Figure 3-17 we reinstate the physical reference arm and compare images obtained by the CCD with our computational simulation; we see a significant discrepancy in the two patterns. We attribute this largely to imperfections in the SLM as described earlier in the Pitfalls section. In particular, since the effect of a single SLM pixel on the far-field speckle pattern is not localized, we expect that the deviations in the

flatness of the SLM plane may highly affect the far-field pattern. In addition, we are unable to reliably predict the physical behavior of the dead space regions of our SLM. In the case of computational ghost imaging without compressed sensing, most of these discrepancies are averaged away after a large number of realizations. However, compressed sensing searches for a sparse object given an underdetermined set of data rather than averaging over a long time, making it much less tolerant to systematic errors; it is essential that especially the measurement matrix ( $A$ ) be sufficiently accurate, which as demonstrated by Figure 3-17 is not the case.

## 3.9 Conclusions

Similar to our work with phase-coherent optical coherence tomography described in the previous chapter, we present phase-sensitive far-field ghost imaging, another example of an experiment previously thought to be exclusive to quantum sources. In addition, we present a new type of classical phase-sensitive light source that is realized by deterministically imposing pseudorandom phase patterns on a pair of light beams using spatial light modulators. We also demonstrate that much like biphoton ghost imaging, phase-sensitive classical ghost imaging also produces an inverted image in the far field.

We demonstrate a couple of advantages that are unique to classical ghost imaging. First, since we impose deterministic phase patterns, we can eliminate the reference arm from the experiment entirely and replace it with a computer simulation. This also greatly simplifies the setup and allows it to be potentially used for long-range ghost imaging where a physical reference arm would be impractical to implement, or imaging at wavelengths where bucket detectors are available but CCD arrays are not. Such a simulation would not be possible using quantum light sources. Similar to our PC-OCT experiment described in the previous chapter, our use of classical detectors permits us to operate at much higher power levels and improve acquisition speed. In contrast to quantum ghost imaging experiments which often require hours or more of acquisition time, we were able to obtain clean images within a few minutes with our main limitation being only the SLM frame rate, offering a practical

speedup by several hundred times.

We additionally recognize that our imaging targets have spatial structure and are far from pixelwise random in nature. This is captured by the concept of spatial sparsity, and explore the use of compressed sensing to further speeding up the acquisition time by computationally reconstructing the image instead of averaging over a large number of trials. We show that with as few as 400 realizations we obtain clear images of our transmission mask, offering a factor of 5-10 speedup in acquisition in comparison with traditional averaging methods.

We also explored the possibility of combining computational ghost imaging with compressed sensing, which did not yield good results in our case. We attribute this to deficiencies in our SLM which prevent us from accurately simulating its physics, which is not essential for traditional acquisition which averages out such errors, but negatively affects compressed sensing which requires an accurate model of the measurement being performed.

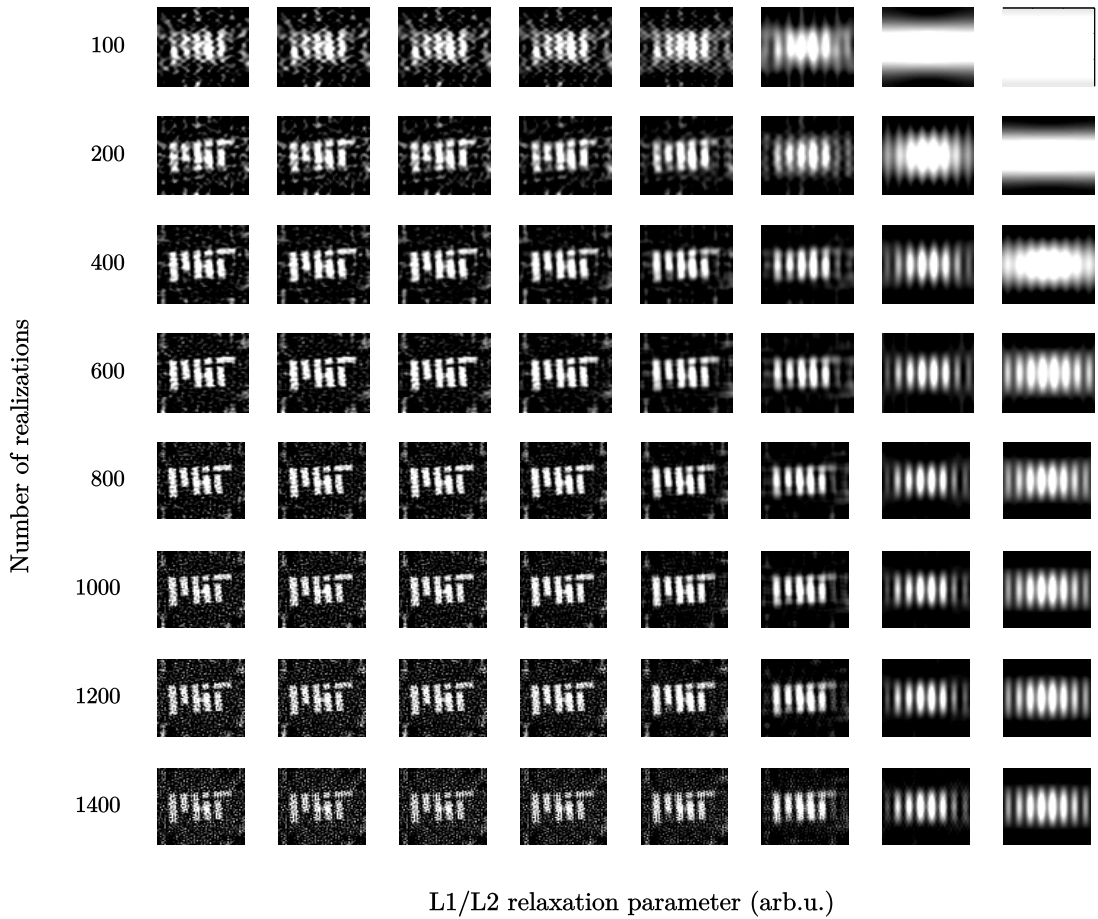


Figure 3-14: Relaxing the constraint to varying degrees in the computational reconstruction using DCT as a sparsifying basis. From top to bottom, we increase the number of realizations, and from left to right, we relax the equality constraint, allowing for errors in the data. We used this process to determine the value of the relaxation parameter  $\epsilon$  to use.

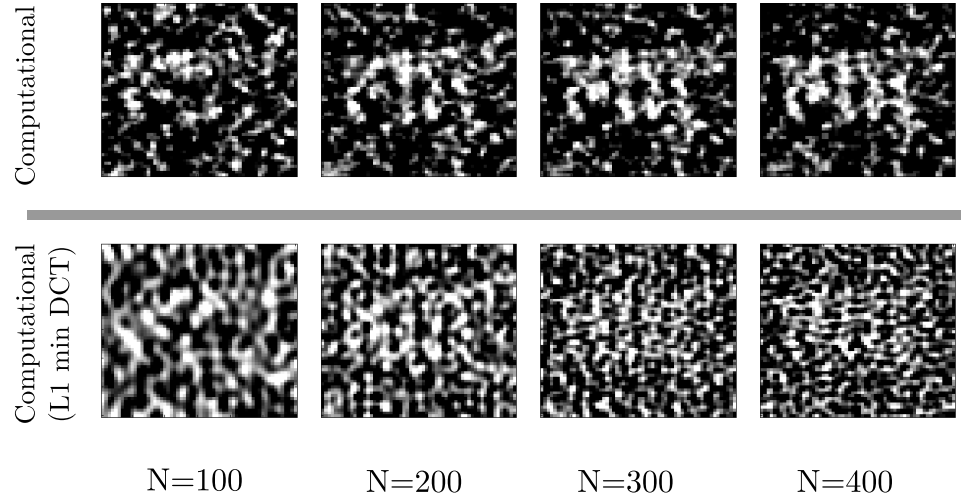


Figure 3-15: Attempts to obtain images of an MIT logo mask imaged using compressed sensing with a computationally-simulated reference arm. (a) shows the computational ghost imaging result using traditional processing, and (b) shows the result of applying compressed sensing techniques. (TODO: add (a) and (b) to figure)

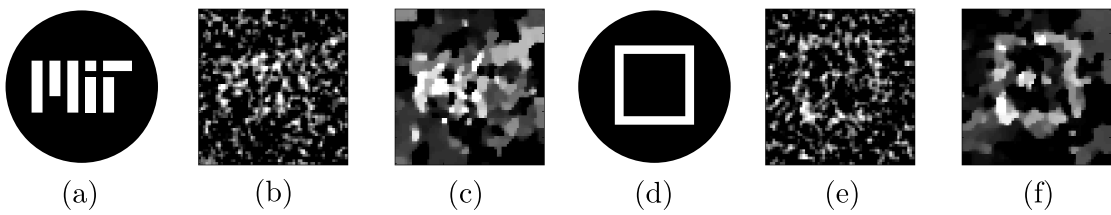


Figure 3-16: Computational compressed ghost imaging using a simpler object. (a) MIT logo mask and ghost image results for (b) covariance-based and (c) compressed sensing using TV minimization for the same number of realizations, showing the same problems seen in Figure 3-15. (d) Simpler square mask and results using (e) covariance-based and (f) compressed sensing using TV minimization.

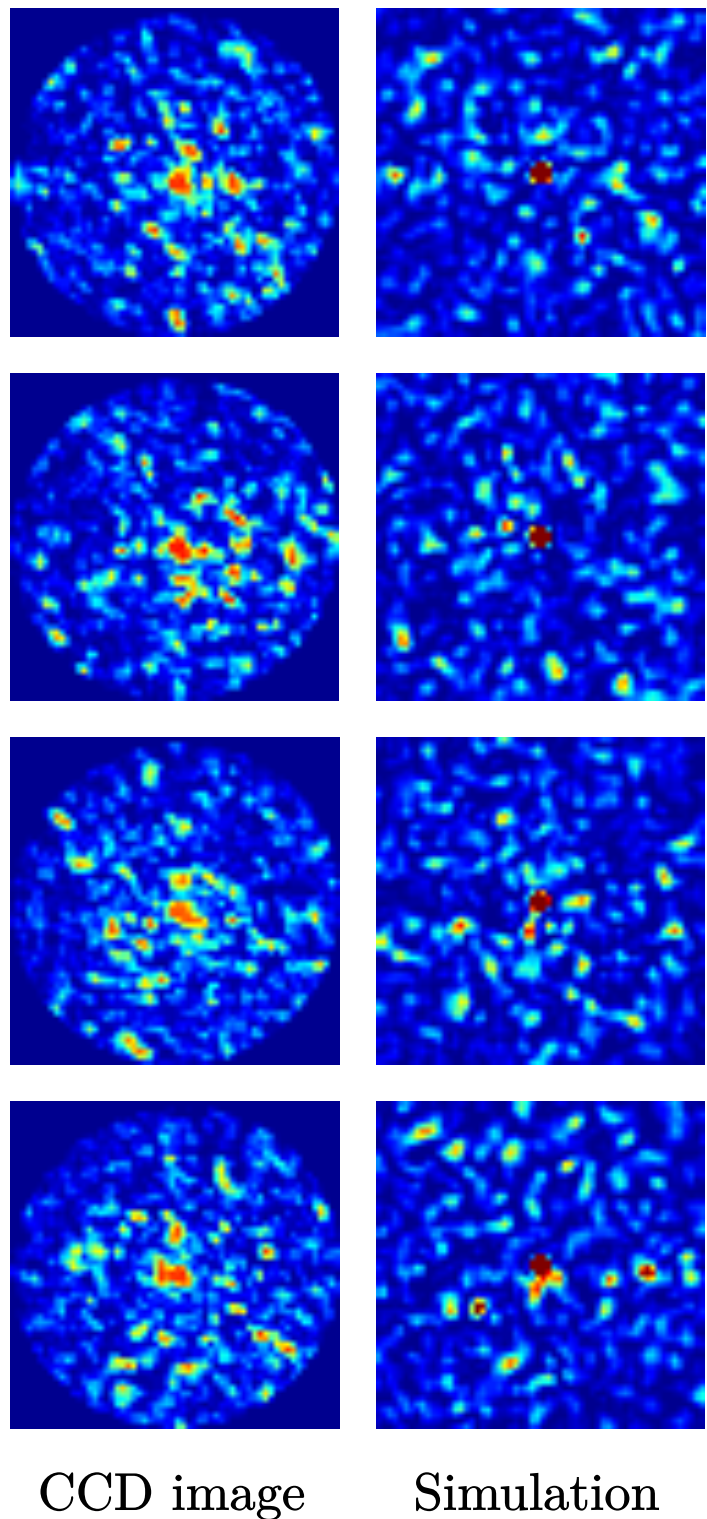


Figure 3-17: Sample speckle patterns acquired by a CCD array (left) and the corresponding computational simulation results (right). We attribute the large discrepancy to imperfections in the SLM array.

# Chapter 4

## Single-photon imaging

While implementing our phase-sensitive ghost imager described in the previous chapter, we learned that averaging measurements over long dwell times is not the most efficient approach to imaging objects which have spatial structure. In particular, by taking a small number of measurements and treating the results as an underdetermined linear system, and using computational optimization techniques to iteratively find the most sparse solution in a suitable basis, it is possible to produce a high-quality image much faster or using a smaller number of realizations than is necessary for high quality images using traditional averaging.

Ghost imaging and single-pixel cameras are non-traditional active imagers that are conceptually interesting and offer advantages in certain specific imaging scenarios, as described in the previous chapter. However, we also pose the question of whether mainstream imaging methods can benefit from similar computational reconstruction techniques to reduce their acquisition times. In particular, capturing three-dimensional structure and reflectivity using a pulsed active illumination has many applications [51] but often difficult to accomplish in scenarios where illumination power must be limited or return photon flux is limited. For example, in biological imaging it is often necessary to limit the active illumination power to avoid heating up and affecting the sample. Similarly, fluorescence lifetime imaging [52] is also limited in photon flux, requiring very long acquisition times to obtain an image.

Remote sensing also has many applications for imaging using pulsed active illumination.

In particular 3D light detection and ranging (LIDAR) systems are often limited due to  $1/r^2$  falloff for spatially-resolved objects with Lambertian reflectivity, severely limiting their range and simultaneously requiring very high illumination power level. In LIDAR imaging, the scene is illuminated with a pulsed laser beam and the back-reflected light is measured by a time-resolving detector. Direct-detection LIDAR typically uses Geiger-mode avalanche photodiodes (APDs) which resolve individual photon arrivals to within tens of picoseconds [53], and obtain transverse spatial resolution either by using a single detector and raster-scanning the illumination one pixel at a time [54] or by flood-illuminating the scene and using a detector array [55]. However, in either case, it is typically necessary to collect hundreds of photon arrivals per pixel in order to perform accurate reflectivity imaging and tens of photons per pixel to perform accurate depth mapping [56, 57, 58, 59, 60, 61] even at negligible background light levels. In the presence of background noise, even more data needs to be collected in order to produce high-quality range images, necessitating long acquisition times.

In this chapter we pose the question of whether we could perform accurate reflectivity and depth mapping using a much shorter dwell time and fewer photon detections, which would greatly speed up acquisition for many of these applications. We established a collaboration with A. Kirmani, A. Colaco, D. Shin, and V. Goyal of the Signal Transformation and Representation Group at MIT to explore first-photon imaging, in which we pose the question of what would happen if we only took a single photon arrival worth of data at each pixel of a LIDAR imager before immediately moving to the next pixel, and whether a high-quality computational reconstruction is possible using such a constrained set of data. In the ideal scenario of zero background noise, we would normally expect to have a range resolution equal to the pulse width, and a featureless reflectivity image since we only measure one arrival at each pixel. In the presence of background noise, the range information would be severely corrupted by any background photons. We devised an algorithm which we describe in this chapter, along with an experimental implementation of our new imaging paradigm.

We then established a collaboration with the Zappa group at the Politecnico di Milano,

who are developing a single-photon APD arrays [62, 63, 64] which can be used for reflectivity and depth imaging applications, and adapted our method to a prototype SPAD array that was brought to MIT.

## 4.1 First-photon imaging

Traditional imaging by histogramming a large number of arrivals at each pixel does not take into account the spatial correlations found in real-world scenes, which both in depth and intensity typically feature smoothly-varying surfaces punctuated by few sharp edges compared to the number of pixels in the scene. Similar to our work in compressed ghost imaging, we expect that drastically reducing our solution space combined with knowledge of the physics of low-flux measurements would make it possible to computationally recover a clean image from a relatively small number of measurements. Hence, we devise an experiment to raster scan a scene in a fashion similar to LIDAR, but returning only the first photon arrival at each pixel. Using traditional imaging techniques, the depth maps generated by such a device would have errors as large as the pulse width, and the reflectivity image would be featureless. However, in this case, we apply our knowledge of the properties of the active illumination system, the physics of single-photon detection, and spatial correlations in real-world scenes to try to recover high-quality reflectivity and depth maps from this first-photon data.

### 4.1.1 Experimental setup and calibration

In the early stages of the experiment, we performed raster scanning using a Discovery 4100 digital micromirror device (DMD) kit and a diode laser with a 1-ns pulse width. However, we found that raster scanning using a DMD resulted in too much loss of power (flood-illuminating a scene and selecting only 1 pixel on a megapixel array would imply a power loss on the order of  $\sim 10^6$ , putting our signal counts lower than the dark count rates of most single-photon APDs). Thus, with DMD-based raster scanning we were limited to

operation only at very low resolutions. In addition, high-power laser diodes operating on sub-nanosecond time scales were not widely available. Although a mode-locked laser or optical amplification would be a viable solution to obtaining high power with short pulses, it would be a much more expensive solution.

In addition, the DMD application programming interface was poorly documented and not easy to synchronize with photon-counting hardware at time scales shorter than  $\sim$ 1 second per realization which is too slow for our purposes. Although the DMD can in principle update patterns much faster, up to rates of over 30 kHz, this mode of operation required preloading a full set of patterns onto the device with a limit of 2048 patterns before a software crash would occur, which is insufficient to raster-scan an image at square resolutions higher than  $45 \times 45$ .

We opted instead to not use a DMD-based setup but instead perform raster scanning using a low power, collimated short pulse diode laser and a two-axis scanning galvo which yielded much higher power at each pixel, faster acquisition times, and simpler experimental design, as shown in Figure 4-1. Since the galvo mirrors accepted analog voltage inputs, it was easy to design a setup that synchronized them with photon-timing hardware, and with power independent of resolution, allowing us to easily scale our acquisition to megapixel levels of resolution.

A diagram of our raster-scanning active imager is shown in Figure 4-1. The illumination source is a PicoQuant LDH series pulsed laser diode with a center wavelength of 640 nm, a tunable repetition rate of 5 - 80 MHz and set at 10 MHz for this experiment. As with most pulsed laser diode sources, the pulse shape and duration is dependent on the power, so we fix our power setting at 0.6 mW average, which gives us pulses with 226 ps RMS duration, as shown in Figure 4-4.

The laser output is reflected off a Thorlabs GVS012 two-axis scanning galvo system which is used to raster scan the beam over the target. The maximum mechanical scan angle is  $\pm 20^\circ$  which is the limit on our field of view. The galvo system takes two analog voltage inputs (one for each axis, 0.5 V/deg) which we supply using a National Instruments NI USB-6008

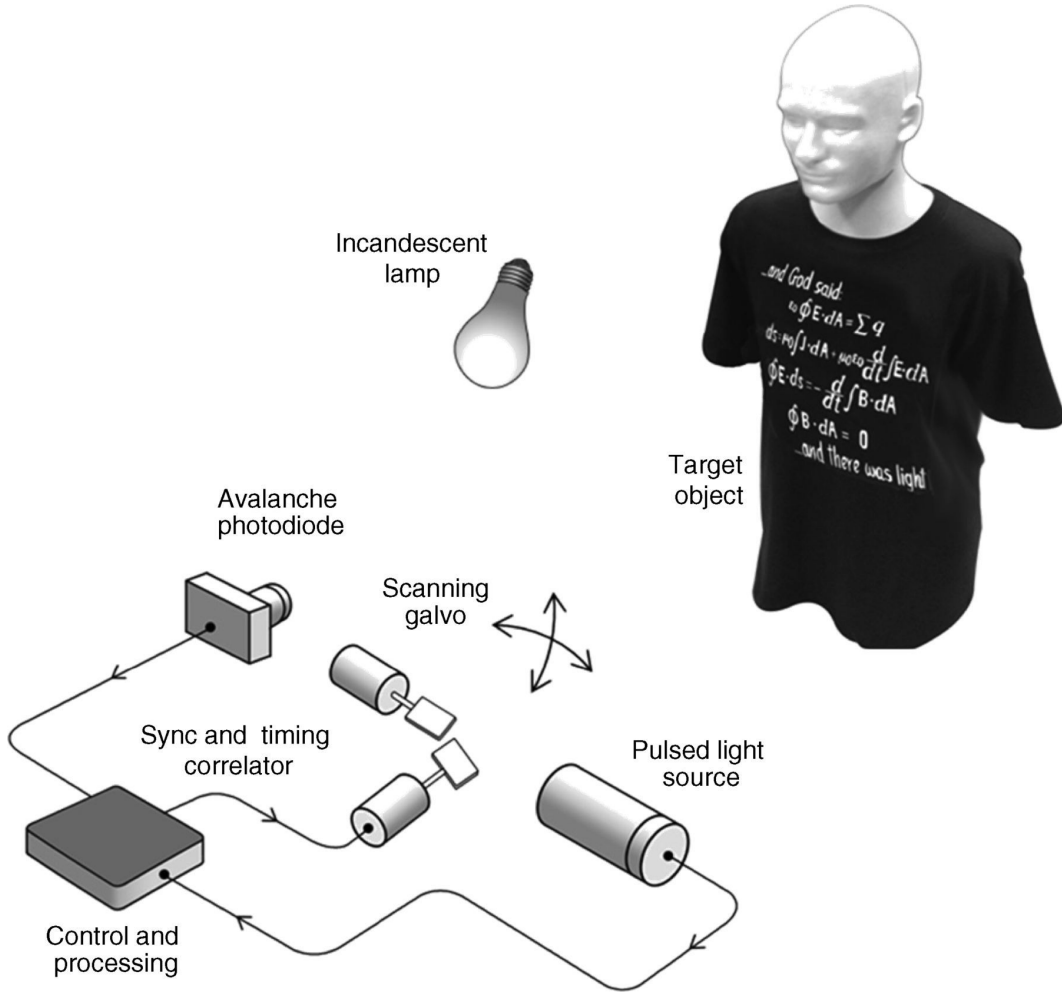


Figure 4-1: Schematic of the raster-scanning imager used for first-photon imaging.

module which contains two 12-Bit analog outputs with a maximum sample rate of 1 kHz.

We placed our objects at a distance of 1.5 to 2 m from the illumination source. The diameter of the spot size at 2 m distance was measured to be  $\sim 1.5$  mm. Prior to detection, the light was filtered using an Andover custom free-space interference filter with 2 nm bandwidth centered at 640 nm and whose peak transmission was 49%. The Geiger-mode APD was a Micro Photon Devices PDM series detector with  $100 \mu\text{m} \times 100 \mu\text{m}$  active area, 35% quantum efficiency, less than 50 ps timing jitter, and less than  $2 \cdot 10^4$  dark counts per second. The photon detection events were time stamped relative to the laser pulse with 8 ps resolution using a PicoQuant HydraHarp TCSPC module. The laser and the single-photon detector

were placed in the same horizontal plane, at a separation of 7 cm, making our imaging setup effectively monostatic.

Prior to measurement, a HydraHarp time-tagged time-resolved (T3) measurement was initiated remotely over a network connection. We performed the raster using a custom Visual C# program that includes correction to the perspective distortion caused by the mounting of the galvo mirror. In addition, the custom program the raster scanning direction, as shown in Figure 4-2, to smooth scanning and avoid abrupt mechanical transitions between rows. Before each movement of the galvo mirror position, a pixel marker pulse was simultaneously output to a designated digital output of the USB-6008 which was connected to a Stanford Research Systems delay generator. The delay generator then generated a pulse compatible with the HydraHarp marker input in order to insert a marker into the data stream indicating a pixel position change. A final marker signal was output after the last pixel as well, accounting for a total of  $N^2 + 1$  markers in each file for an  $N \times N$ -pixel image. The resulting HT3 files are read using a custom GNU C program (see Appendix A) based on PicoQuant file specifications, which discards the data prior to the first pixel and after the end of the measurement, and outputs a MATLAB-friendly ASCII file describing all the marker and photon detection events. For photon detection events, the C program additionally outputs the laser pulse number and the time bin in which the detection was received. For marker events, the C program outputs the total number of photons detected since the last marker and the sum of the time bin values since the last marker, allowing for convenient retrieval of the traditional averages (ground truth) measurement. The C program also has an option to only output the first few photon detections after each marker, to reduce data storage as converting the entire .ht3 file to ASCII format would occupy several tens of gigabytes. The output ASCII format is illustrated in Figure 4-3.

## Focusing of laser beam

As with most diode lasers, the output of the PicoQuant LDH series laser diode is multimodal and not very well collimated beyond a range of several tens of centimeters. Since a large

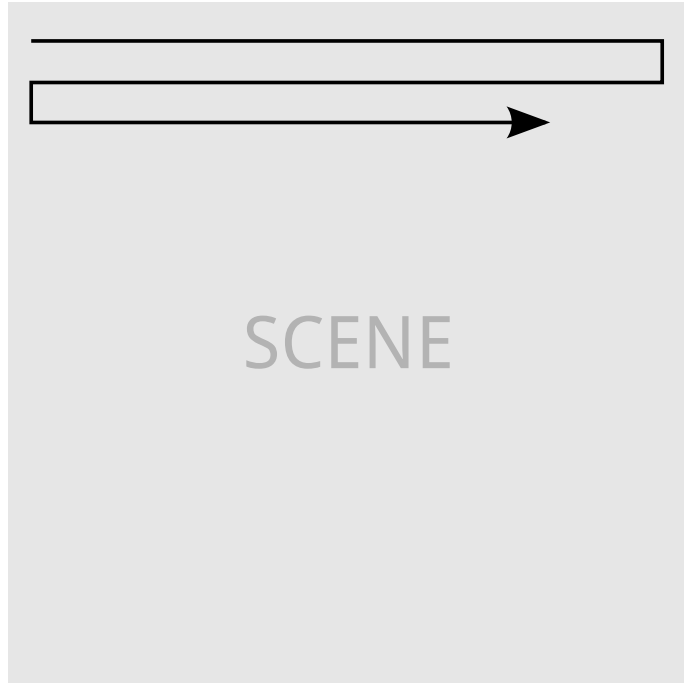


Figure 4-2: Raster scanning was performed in alternating directions for each row in order to avoid abrupt transitions in translating the galvo mirrors.

spot size would reduce our transverse resolution, we mitigate this problem by using a pair of 12-cm focal length lenses to loosely focus the beam such that the spot size is small ( $\sim$ 1 mm) over the 1.5-m to 2-m range where we place the object.

### Addition of background noise

In order to simulate a realistic imaging scenario with background noise, we placed an incandescent lamp in the room pointed at the detector, and set the background noise level equal to the signal level (i.e. the probability of any detection being due to background noise would be around 50%). We set this level by first turning off the incandescent source and using the laser to illuminate a reference point on a highly-reflective Lambertian surface at a distance of 2 m, measuring the average detected photon rate, and then matching that rate by adjusting the current input to the incandescent source.

—	Event # in original .ht3 file					
—	Event type (0=marker, 1=photon)					
—	Marker or APD input channel #					
—	For marker events:					
—	total # of detections since last marker					
—	For detection events:					
—	Total # of laser pulses emitted thus far					
—	For marker events:					
—	sum of time bin values since last marker					
—	For detection events:					
—	time bin at which detection was received					
1595847	0	01	43689	223482557	(Marker)	
1595848	1	01	153602651	5000	(Detection)	
1595849	1	01	153602665	5067	(Detection)	
1595850	1	01	153602947	5428	(Detection)	
1595852	1	01	153603168	5009	(Detection)	
1595853	1	01	153603230	5064	(Detection)	
...						

Figure 4-3: Description of the MATLAB-friendly .out format generated by our custom GNU C .ht3 file reader.

### Photon flux waveform measurement

For range estimation, our computational imager requires knowledge of the photon-flux waveform of the laser pulses. We use  $s(t)$  to denote the normalized ( $\int s(t)dt = 1$ ) version of this waveform for a laser pulse emitted at  $t = 0$ . This pulse shape was measured by directly illuminating the detector with highly attenuated laser pulses and binning the photon arrival times to generate a histogram of photon counts. Fitting a skewed Gamma function to this histogram yielded:

$$s(t) \propto A(t - T_s)^4 \exp\left(-\frac{t - T_s}{T_c}\right) \quad (4.1)$$

where  $T_s = 80$  ps and  $T_c = 40$  ps, as shown in Figure 4-4.

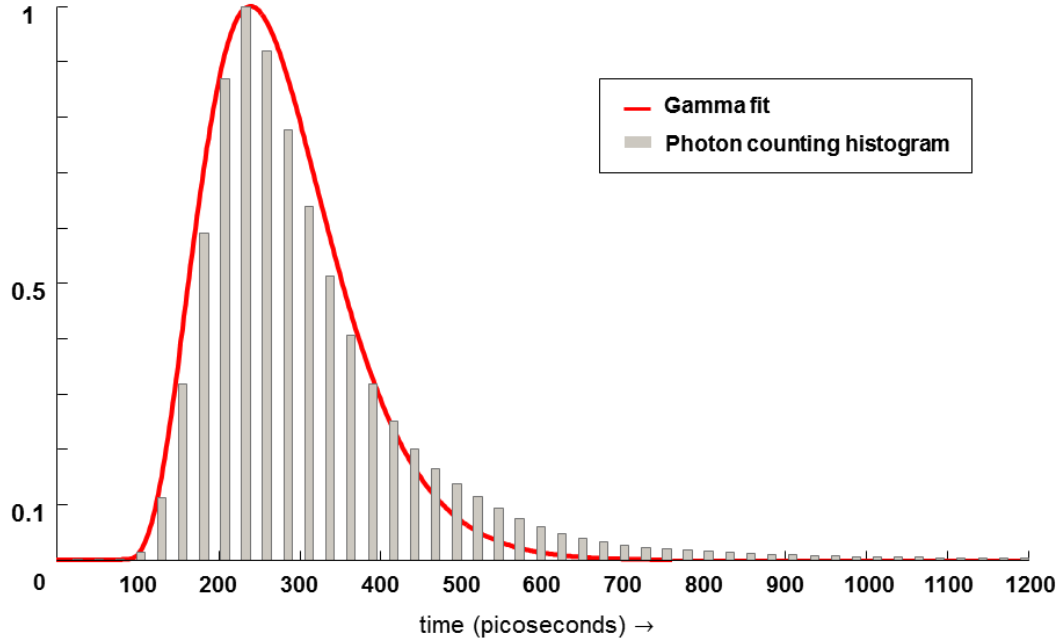


Figure 4-4: Pulse shape of the PicoQuant LDH series laser diode obtained by histogramming, and skewed Gamma function fit.

### Acquisition procedure

To generate one complete data set, we raster scan over  $1000 \times 1000$  pixels with the two-axis galvo. At transverse pixel location  $(x, y)$ , we implement a first-photon imager that records only two values:  $n(x, y)$ , the number of laser pulses transmitted prior to the first detection event; and  $t(x, y)$ , the timing of the detection relative to the pulse that immediately preceded it. An ideal first-photon imager would move to the next pixel immediately after a single detection event. In our case, it is not possible to build such a fast system since we are physically limited by the mechanical speed of our galvo mirror system; at the fastest scanning rate we typically observe tens or even hundreds of photon arrivals at each pixel. Faster scanning may be achievable using smaller galvo mirrors or digital micromirror arrays. We are also limited by the 1 kHz sampling rate of our digital-to-analog converter, which permits a fastest acquisition of a little under 17 minutes for a 1-megapixel image. Without these physical raster scanning limitations, our photon flux is high enough for much faster acquisition.

In order to compare our first-photon imaging method with traditional acquisition techniques, we need to perform a baseline measurement with traditional histogramming. In order to do this we deliberately slow down the acquisition to approximately 3 hours per image in order to collect enough photon arrivals at each pixel to obtain a clean histogram of a few thousand arrivals at each pixel. Our reference images are constructed from averaging over  $\sim 1000$  arrivals at each pixel, and are generated only for comparison purposes. For our novel first photon imaging method, we only utilize the first arrival at each pixel and discard all subsequent data.

Because our entire scene was contained within a few meters of the imaging setup, our 100 ns pulse repetition period guaranteed that each non-background photon detection came from the immediately preceding laser pulse.

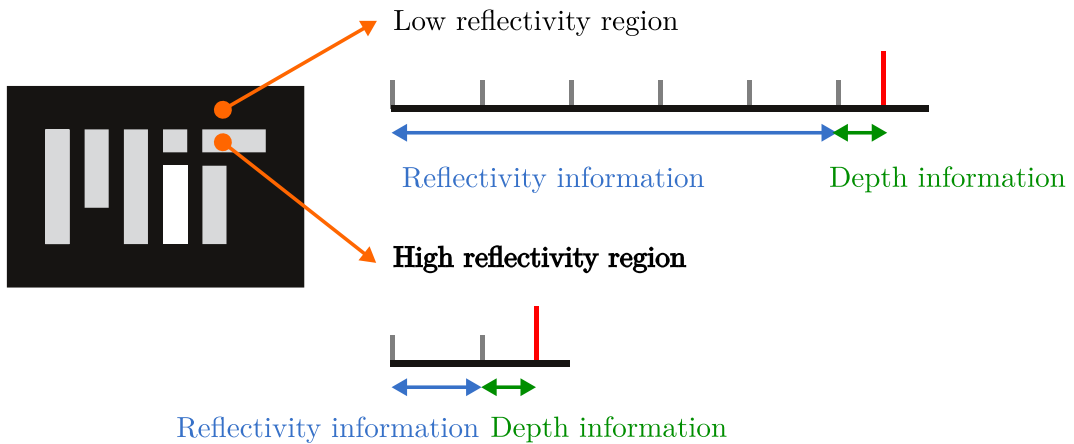


Figure 4-5: Reflectivity and depth information obtained from a single photon arrival: the depth information is obtained by measuring the time difference between the photon arrival and the laser pulse sync signal, while the reflectivity information is obtained by the number of laser pulse periods elapsed until the first photon detection.

#### 4.1.2 Computational reconstruction procedure

In this section we present a 3-step computational reconstruction procedure that we use to recover high quality scene reflectivity and depth data from the first photon arrival data. A. Kirmani, D. Shin, A. Colaco, V. Goyal, and J. Shapiro developed the theoretical framework

outlined below [65, 66] with feedback from early experimental data.

## Reflectivity reconstruction

Traditional imaging techniques typically count photon arrivals to measure reflectivity. However, given only a single arrival, the only information we obtain about reflectivity is the time duration (i.e. number of laser pulse repetition periods) until a photon is detected, as shown in Figure 4-5. Since brighter regions reflect a greater number of photons, the mean time duration until a photon is detected is shorter. This is characterized by Poisson statistics. Let  $S$  be the average photon number in the back-reflected signal from a hypothetical unity-reflectivity spatial location illuminated by the laser pulse,  $\alpha(x, y)$  denote the scene reflectivity at pixel location  $(x, y)$ ,  $B$  denote the background photon arrival rate,  $T_r$  be the pulse repetition period, and  $\gamma$  be the efficiency of the detector. The probability of not detecting a photon is then

$$P_0(x, y) = \exp(-\gamma[\alpha(x, y)S + BT_r]) . \quad (4.2)$$

Since these probabilities are independent and identically distributed (iid) for each pulse, it follows that the number of pulses until a detection, denoted by  $n(x, y)$ , is geometrically distributed:

$$\Pr[n(x, y) = k] = P_0(x, y)^{k-1} [1 - P_0(x, y)] . \quad (4.3)$$

When there is no background light present, it follows that the maximum likelihood (ML) estimate of the reflectivity at each pixel  $\hat{\alpha}_{ML}(x, y)$  is proportional to  $1/n(x, y)$  for  $n(x, y) \gg 1$ . In the presence of high background light ( $BT_r > \alpha(x, y)S$ ) this estimate becomes severely corrupted since it is much more likely that a background photon will reach the detector before a signal photon.

In order to perform a sparsity-promoting computational reconstruction of the reflectivity from this data, we first compute the log-likelihood of the ML estimate above, which is derived

in [65]:

$$\mathcal{L}(\alpha(x, y) | n(x, y)) = \gamma [\alpha(x, y)S + BT_r] [n(x, y) - 1] - \log [\gamma\alpha(x, y)S + BT_r] . \quad (4.4)$$

We must also choose a sparsity-promoting basis for reconstruction. Most objects are characterized by smoothly-varying surfaces punctuated by sharp edge transitions; this type of sparsity is captured well by most wavelet bases which are localized in both space and frequency. Bases such as the Fourier Transform or Discrete Cosine Transform which only localize frequency and not space require a large number of nonzero basis elements to describe sharp edges and are not typically the best choice for these types of objects, but may be a more suitable choice for imaging scenarios that do not contain edges. In our case we use the discrete wavelet transform (DWT) derived from Debauchie's 4-tap filters [67]. Representing the wavelet transform as  $\Phi(\cdot)$  which is implemented in the form of matrix multiplication, we denote the wavelet coefficients as  $\{w(x, y)\} = \Phi(\{\alpha(x, y)\})$  for the collection of reflectivity estimates  $\{\alpha(x, y)\}$  for all pixel coordinates  $(x, y)$ . A standard measure of sparsity, similar to that which we used in compressed sensing in the previous chapter, is the  $\ell_1$ -norm of these coefficients, defined by:

$$||\Phi(\{\alpha(x, y)\})||_1 = \sum_x \sum_y |w(x, y)| . \quad (4.5)$$

We would like to reconstruct the reflectivity estimate by minimizing a weighted sum of both the negative log-likelihood and the sparsity measuring function over the set of all possible images  $\{\alpha(x, y)\}$ . This enforces that the estimate cannot deviate too far (quantified by the probability distribution itself) from the measured data, and that the estimate needs to be as spatially sparse as possible (quantified by the chosen DWT basis). The optimization program can be written as the minimization of

$$\{\hat{\alpha}(x, y)\} = \arg \min_{\{\alpha(x, y)\}} (1 - \beta) \left[ \sum_x \sum_y \mathcal{L}(\alpha(x, y) | n(x, y)) \right] + \beta ||\Phi(\{\alpha(x, y)\})||_1 \quad (4.6)$$

enforcing that  $\hat{\alpha}(x, y) \geq 0$  for all  $(x, y)$ . Since the log-likelihood function is convex in  $(x, y)$ , and that the sparsity-promoting function is also convex [68], their nonnegative weighted sum also becomes strictly convex. This enables us to efficiently find the global minimum solution to  $\{\alpha(x, y)\}$  by iteratively searching for a local minimum.

### Background noise censoring

Before reconstructing the depth map of our object, we wish to eliminate the photon arrivals that are due to the background light and provide no information about depth. We do this by taking advantage of the fact that anomalous detections due to background light are independently and uniformly distributed over  $[0, T_r]$  with a high variance of  $T_r^2/12$  (following from the uniform probability distribution), whereas detections from back-reflected signal pulses are temporally concentrated and spatially correlated with signal detections from nearby pixels.

We approach the censoring of noise photons by computing the rank-ordered absolute differences (ROAD) statistic [69] for each pixel. For each photon, we use the photon arrival times of the eight nearest neighbors and then perform a binary hypothesis test to decide whether the photon is due to background or noise with high probability. This binary hypothesis test is dependent on the reflectivity of the object at that pixel, which we recovered in the previous step (this is the reason why noise censoring cannot be done prior to reflectivity reconstruction, although it may be possible to consider an iterative procedure). We then delete the anomalous range values and replace them with averages of the neighbors before performing depth reconstruction.

The ROAD statistic is calculated as follows: for each pixel  $(x, y)$ , we take the eight neighboring pixels  $(x_1, y_1) \dots (x_8, y_8)$  and compute the time-of-arrival differences with the current pixel:

$$|t(x_1, y_1) - t(x, y)|, \dots, |t(x_8, y_8) - t(x, y)| \quad (4.7)$$

We then sort these values in ascending order, and define  $\text{ROAD}(x, y)$  to be the sum of the first four values in the sorted list.

We then use a binary hypothesis test to classify whether the photon arrival at  $(x, y)$  is due

to signal light or background light. We combine our knowledge of the reflectivity estimate  $\hat{\alpha}(x, y)$  which we obtained in the previous step with theory of merged Poisson processes [70] to obtain the probabilities:

$$\Pr[\text{background}] = \frac{BT_r}{\hat{\alpha}(x, y)S + BT_r} \quad (4.8)$$

$$\Pr[\text{signal}] = 1 - \frac{BT_r}{\hat{\alpha}(x, y)S + BT_r} \quad (4.9)$$

We then generate the threshold  $C$  used for a binary hypothesis test as follows:

$$C = 4T_p \frac{BT_r}{\hat{\alpha}(x, y)S + BT_r} \quad (4.10)$$

where if  $\text{ROAD}(x, y) \geq C$ , we decide that the photon arrival is due to background light, delete the photon arrival and replace it with an average of its eight neighbors, and if  $\text{ROAD}(x, y) < C$ , we keep the data point. This method works with high reliability [69] as long as the pulse width is much shorter than the repetition period. (TODO: Analyze  $P_D$  and  $P_{FA}$ )

## Depth reconstruction

The approach to reconstruction of the depth map of the object is similar to that of the reflectivity reconstruction approach. For each pixel  $(x, y)$  we first compute the log-likelihood function relating the signal photon's arrival time  $t(x, y)$  to the depth map of the scene  $Z(x, y)$  in distance units. This is given by:

$$\mathcal{L}(Z(x, y)|t(x, y)) = -\log \left[ s(t(x, y) - \frac{2Z(x, y)}{c}) \right] \quad (4.11)$$

where  $s(\cdot)$  is the pulse shape given earlier,  $c$  is the speed of light, and the factor of 2 is incurred due to the round-trip distance from the emitter to the object and back to the detector. We insert the fitted  $s(\cdot)$  we determined earlier to obtain:

$$\mathcal{L}(Z(x, y)|t(x, y)) = -4 \log \left[ t(x, y) - \frac{2Z(x, y)}{c} \right] - \frac{t(x, y) - T_s - 2Z(x, y)/c}{T_c} \quad (4.12)$$

This negative log-likelihood function is strictly convex in  $Z(x, y)$  which we again require for efficient computational reconstruction.

Similar to the reflectivity construction, we measure sparsity using the  $\ell_1$ -norm of the wavelet transform of  $Z(x, y)$  and form a reconstruction of the depth image by solving

$$\{\hat{Z}(x, y)\} = \arg \min_{\{Z(x, y)\}} (1 - \beta) \left[ \sum_x \sum_y \mathcal{L}(Z(x, y) | t(x, y)) \right] + \beta \|\Phi(\{Z(x, y)\})\|_1 \quad (4.13)$$

subject to  $\hat{Z}(x, y) \geq 0$  for all  $(x, y)$ .

## Software implementation

We employ the SPIRAL-TAP package for MATLAB [71] to implement the optimization programs described in steps 1 and 3 above. Step 2 (background noise censoring) is implemented directly in MATLAB. For the starting point of the convex optimizer used for step 1, we use the pointwise ML estimate as a starting point:

$$\alpha_{ML}(x, y) = \max \left\{ \frac{1}{\gamma S(n(x, y) - 1)} - \frac{BT_r}{S}, 0 \right\} \quad (4.14)$$

For the starting point of the depth estimator, we use the ML estimate

$$Z_{ML}(x, y) = (t(x, y) - T_m)c \quad (4.15)$$

where  $T_m = \arg \max s(t)$  as long as the detection at pixel  $(x, y)$  was determined in step 2 to be due to a signal photon. For noise pixels we input  $Z(x, y) = 0$  as the starting point to the optimization routine. Full code and sample data are available as supplementary materials online [65].

### 4.1.3 Results

#### Mannequin

Our main imaging target was a life-size plastic mannequin wearing a black T-shirt with white text. We chose this not only as an example of a realistic target, but also as one which has both depth and intensity features on multiple scales.

Figure 4-6 shows separate reflectivity and depth images of an early measurement scanned at a lower resolution of  $300 \times 300$  with the mannequin placed next to a sunflower without added background noise, including a reference ("ground truth") measurement, raw ML estimates from a first-photon acquisition, and the result of our computational reconstruction. We see that our algorithm is able to recover fine features, particularly the petals of the flower and facial features of the mannequin seen in the reference image.

We then switched on the incandescent lamp to the level described earlier and found our reconstruction method to perform surprisingly well under such high levels of background noise. Figure 4-7 shows the results of this measurement, displayed as reflectivity superimposed on a 3D scatter plot of the depth data from raw data to each step of data processing described above; all pictures are generated from the same data set consisting of one photon detection per pixel. We notice that the reflectivity reconstruction is able to recover sufficient detail to resolve fine text on the T-shirt, a close-up of which is shown in Figure 4-8. Background noise censoring and depth reconstruction is also able to recover many facial feature details almost impossible to make out in the raw data.

#### Depth chart

To independently analyze the depth-resolving capabilities of our computational reconstruction technique, we constructed and imaged a depth chart consisting of a flat board with  $5 \times 5$  embossed rectangular plastic squares, as shown in Figure 4-9. Each square had transverse dimensions of  $5 \times 5$  cm and the axial heights linearly increased in steps of  $\sim 3.2$  mm along both axes. The entire board was spray-painted using a single color of matte-finish paint for near-constant and Lambertian reflectivity. We first took a reference ("ground truth")

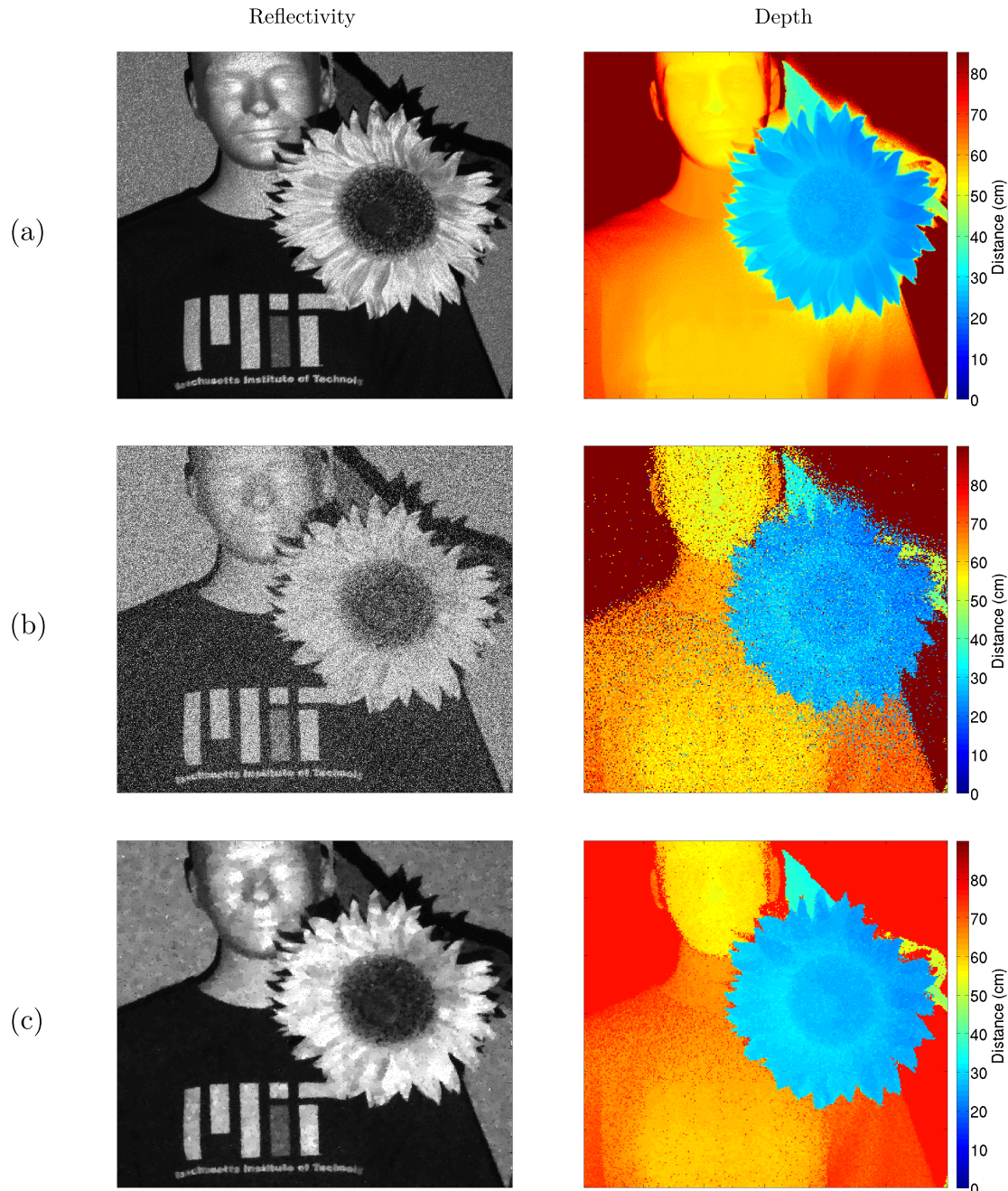


Figure 4-6: Early reflectivity and depth images of a mannequin and flower scene imaged using a  $300 \times 300$ -pixel raster scan without added background noise. (a) Reference ("ground truth") measurement obtained using several hundred photon arrivals at each pixel, averaged. (b) Raw ML estimates obtained using only the first photon arrival at each pixel. (c) Our computational reconstruction method applied to the data in (b).

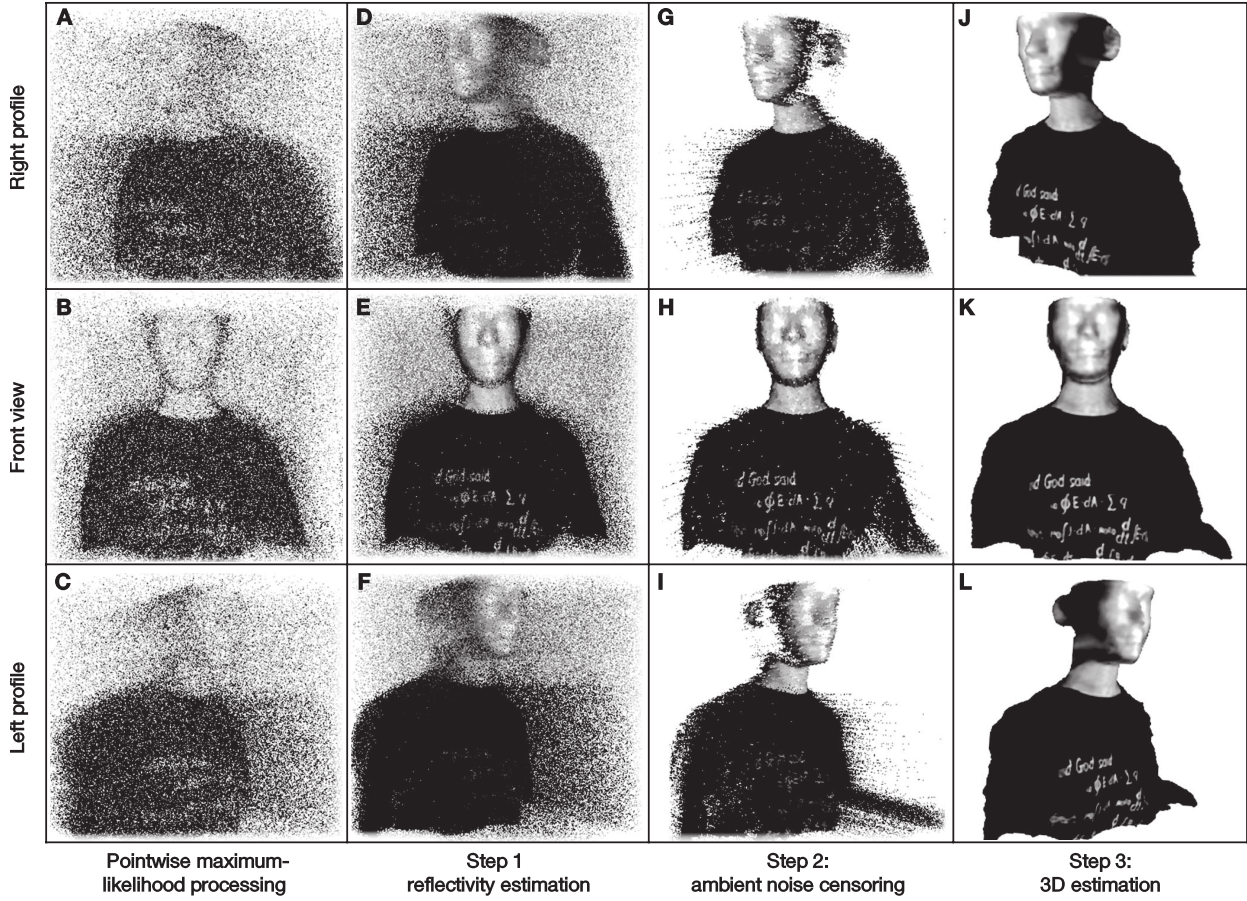
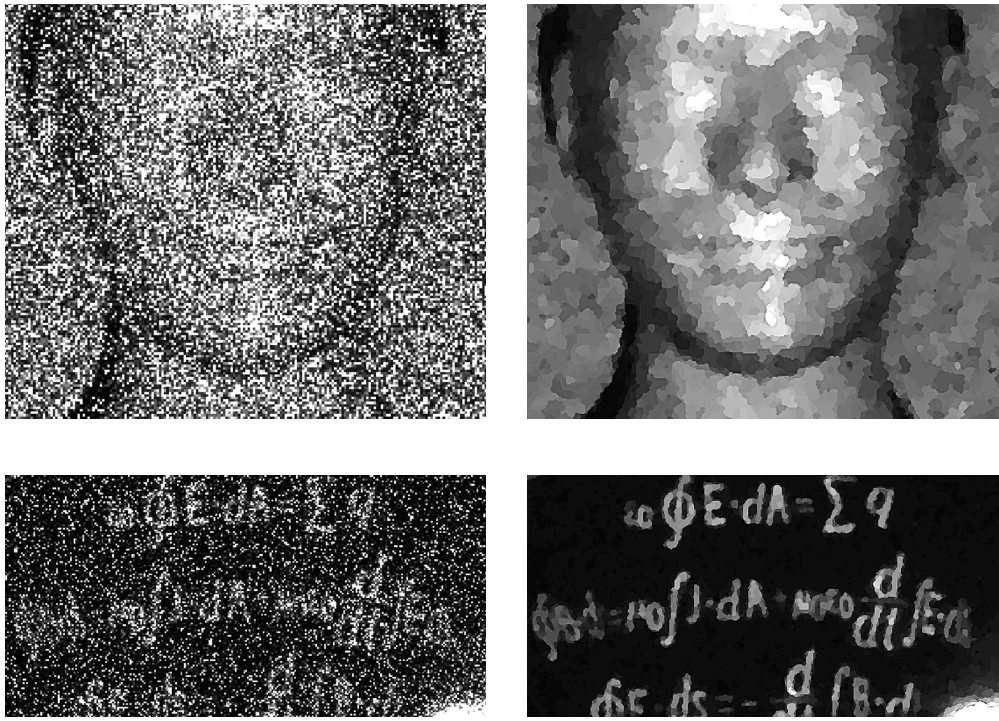


Figure 4-7: 3D mesh views of a single first-photon acquisition with added background noise after various stages of processing. (A)-(C): Raw reflectivity ML estimate  $\alpha_{ML}(x, y)$  superimposed over depth ML estimate  $Z_{ML}(x, y)$  from first photon data, (D)-(F): after reflectivity reconstruction of  $\alpha(x, y)$ , (G)-(I): after background noise censoring, (J)-(L): after depth reconstruction of  $Z(x, y)$ .

measurement by accumulating and averaging hundreds of arrivals at each pixel, as shown in Figure 4-9(a), which clearly shows all 25 squares. Although the board itself was flat, the depth images incur spherical distortion due to angular raster scanning.

Figure 4-9(b) shows the ML estimate of the depth taken only from the first photon arrival at each pixel. Since our axial feature size is on the order of  $\sim 3.2$  mm and our RMS pulse duration is  $\sim 226$  ps which multiplied by the speed of light corresponds to 67 mm, it is natural to expect that objects significantly smaller than the pulse width would be almost impossible to resolve without averaging; this is indeed the case with the raw ML estimate.



(a)

(b)

Figure 4-8: Close-up of two regions of reflectivity data for mannequin target. (a) ML estimate using only 1 photon per pixel and (b) the same data after processing using our computational reconstruction technique.

However, as we see in Figure 4-9(c), the same data processed through our computational reconstruction technique demonstrates the ability to resolve squares as small as 6.4 mm, which demonstrates sub-pulse depth resolution by over a factor of 10. This is explained by the fact that the ML estimates do not take into account spatial regularity, whereas our computational reconstruction approach promotes smooth surfaces with few sharp transitions, making use of data from several pixels at once to extract these features that are otherwise almost invisible.

## Reflectivity chart

We also constructed a chart to independently analyze the reflectivity-resolving capabilities of our imager. As shown in Figure 4-10, the chart consists of printed greyscale squares arranged in rows of 2, 4, 8, and 16 shades on linear scales, corresponding to 1, 2, 3, and 4 bits of reflectivity resolution, respectively. Figure 4-10(a) shows the ground truth measurement obtained by averaging the number of photon arrivals over a long dwell time, and is essentially a greyscale photograph in the traditional sense. Figure 4-10(b) shows the ML estimate of the reflectivity from only the first photon arrival, which results in an extremely noisy image since the error on the ML estimate is high. Figure 4-10(c) shows the same first-photon data processed using our reconstruction technique. We see that we can clearly resolve between 8 and 16 shades of grey, corresponding to  $\sim 3$  to 4 bits of reflectivity resolution. Again, although it may seem counterintuitive to obtain such high reflectivity resolution using only 1 photon arrival at each pixel, we are exploiting sparsity in the scene and promoting spatially-smooth objects, making use of several nearby pixels of data at once, in contrast to traditional averaging methods which treat each pixel as an independent object.

## 4.2 Reflectivity from depth data

We also noted a curious phenomenon in which in the presence of background noise, the first-photon depth data alone yielded some information about reflectivity, without knowledge of the number of pulses until the first detection. We make use of the fact that for pixels in spatially-correlated regions of high reflectivity, signal photons are more likely to reach the detector first, whereas for pixels in regions of low reflectivity, background photons are more likely to reach the detector first. This fact is captured by taking local variances of the depth data; higher variances are the result of first-photon contributions from the uniform time distribution of the background photons, whereas lower variances are the result of increased first-photon contributions from the laser pulse. Figure 4-11 shows an example of such an image obtained by taking the  $1000 \times 1000$ -pixel raw depth data and estimating each pixel's

reflectivity  $\alpha(x, y)$  with

$$\hat{\alpha}(x, y) = 1/\sqrt{\text{var}(\{Z(x-1, y-1), Z(x, y-1), Z(x+1, y-1), \dots Z(x+1, y+1)\})} \quad (4.16)$$

Spatial regularization applied to this scheme may be able to further improve the quality of the image; conversely, it may be possible to make use of this additional information in improving the quality of the first-photon images obtained earlier instead of censoring all background noise photons. It is worth noting that this method of garnering reflectivity data works only in the case where background and signal levels are similar; it would not be possible to apply this to a scenario without background noise.

### 4.3 Imaging using a SPAD array

We now turn to the question of single-photon imaging without raster scanning. Although there are no high-resolution commercially-available single photon detector arrays as of the time of this writing, necessitating raster scanning, it would be highly desirable to be able to image an entire scene in parallel, enabling an acquisition speedup by as much as a factor of the number of pixels and enabling possibilities for real-time high-speed video and other commercial, scientific, or military applications.

Although not yet commercially available, single-photon avalanche photodiode (SPAD) arrays are currently a popular topic of research. F. Villa et al. at the Politecnico di Milano researched and developed an  $32 \times 32$ -pixel SPAD array [72] that features 6-bit photon-counting and 10-bit time-of-flight ranging modes. We formed a collaboration with principal investigator F. Zappa and invited graduate student R. Lussana to bring two prototypes of the SPAD array to MIT to test with our computational reconstruction method.

### 4.3.1 Hardware specifications

The SPAD array developed by the Zappa group is a  $32 \times 32$ -pixel array of fully independent CMOS SPAD detectors. Each pixel is  $150 \times 150 \mu\text{m}$  in size, comprising a total array size of  $4.8 \times 4.8 \text{ mm}$ . Each pixel has a circular active region with diameter  $30 \mu\text{m}$ , giving a fill factor of 3.14%. The photon detection efficiency at 640 nm is  $\sim 20\%$  which gives a combined detection efficiency of 0.63%. Although the efficiency of detection is extremely low, we understand that this is an early-stage prototype device and expect that future research in SPAD arrays will be able to achieve higher fill factors and detection efficiencies.

The dark count rate of the SPAD array is specified at  $\sim 100$  cps, but we found that in reality the dark count rate varies across pixels. In particular a small number of "hot" pixels have extremely high dark count rates which we attribute to the reliability and reproducibility of the fabrication process, as described in [72].

### Modes of operation

The array has two modes of operation: counting mode and timing mode. In counting mode, the 6-bit registers located at each detector site are incremented each time a photon arrival is detected, allowing for up to 63 photon arrivals (binary 111111) before rolling over to 0. Hence in counting mode it is important to keep the power level low enough to avoid this rollover. Alternatively, in the case of smoothly-varying objects, it may be possible to unwrap the rollover, similar to 1-dimensional phase-unwrapping algorithms.

In timing mode, SPAD array outputs a digital signal at the start of each acquisition window which can be used to synchronize a laser diode. Figure 4-14 illustrates the terminology and time scales we will use to describe the timing mode acquisition process. The 6-bit registers at each pixel are used for recording the time of arrival of the first photon arrival at each pixel with a global electronic shutter. Additional 4-bit register at each pixel using a timing interpolation scheme [72] provide for a total of 10 bits of timing resolution (1024 bins). The time bin size is  $\sim 389.9 \text{ ps}$ , governed by the hardware clock rate of 160.3 MHz with  $16 \times$  multiplication in half-coarse mode [72]. Multiplying the time bin size by 1024 gives

an acquisition window of 399 ns. It should be noted that unlike the single photon detector and HydraHarp setup, the SPAD array needs additional time for data readout, which takes a minimum of 10  $\mu$ s per frame. This limits the maximum frame rate of acquisition to around 100 kfps in burst mode, in which a short number of frames are acquired and data stored on the SPAD array itself until subsequent offloading to a PC. In continuous acquisition mode, the USB link limits us to an acquisition rate of around 10 kfps.

Since the acquisition window is 399 ns but the length of one frame of data acquisition can be no shorter than 10  $\mu$ s, this severely impacts our measurement duty cycle. However, the SPAD array also features a “refolding mode” in which continuous measurements of 1024 time bins (399 ns) are performed back-to-back in a single frame but without resetting the registers; whenever a photon is detected at a particular pixel, that pixel will no longer record any more data until the registers are reset at the start of next frame. However, to avoid overheating, it was advised to maintain the active acquisition duty cycle (gate-on time) under 1/4. In our measurements, we used this refolding mode acquisition, extending the frame length to 65  $\mu$ s and acquiring continuously in for 16  $\mu$ s within that 65  $\mu$ s. The remaining 49  $\mu$ s is for cool-off and data transfer.

The SPAD array also includes a feature that enables multiple laser pulses to be fired within each acquisition window. Since our 1024-bin, 399-ns acquisition window is much larger than our laboratory in speed-of-light units, we configured the SPAD array to fire 8 laser pulses per window (i.e. one pulse per 128 time bins).

Note that in refolding mode the SPAD hardware does not reset any registers until a readout, and thus does not provide information about which pulse a particular photon detection corresponds to; thus, for reflectivity measurements it is important to ensure that the refolding factor is low enough such that we are not saturating each pixel with a photon at every frame. If most of the 32 $\times$ 32 pixels register detections at each frame, our reflectivity ML estimates would be featureless and it would be impossible to use Poisson statistics to infer any information. (An alternate approach would be to simply switch the SPAD array to counting mode to perform reflectivity measurements; however, changing the SPAD ac-

quisition mode is not instantaneous, requires reprogramming the on-board FPGA, making high-speed alternating acquisition impossible with the current hardware design.)

### 4.3.2 Experimental setup

A diagram of the experimental setup is shown in Figure 4-12. The illumination used the same PicoQuant LDH-series laser but configured for flood illumination using two ground-glass diffusers in series (one single layer preserved too much coherence and created large-size speckles on the target). The laser diode was operated in external clock mode, driven by the laser trigger output of the SPAD array.

The SPAD array has a total array size of  $4.8 \times 4.8$  mm with  $32 \times 32$  pixels. In principle we would like both a larger imaging area as well as a higher number of pixels in order to experiment with computational reconstruction methods. Given the limited size of the current SPAD array, we opted to use multiple image scans to form a larger-size composite image. We mounted the SPAD array on a feedback-controlled, two-axis motorized translation stage and translate over exactly  $6 \times 6$  tiles of the  $4.8 \times 4.8$  mm array, as shown in Figure 4-13(a), giving us a total imaging area of  $28.8 \times 28.8$  mm and a resolution of  $192 \times 192$  pixels. However, since the active area of each pixel is only  $30 \mu\text{m}$  in diameter, which is less than  $1/4$  of the pixel pitch, we were able to multiply this resolution through factor-of-4 subsampling at each pixel, translating the SPAD array along both axes to all combinations of fractional pixel pitch distances ( $0, 1/4, 1/2$ , and  $3/4$ ) along both x- and y-axes before moving onto the next tile, as shown in Figure 4-13(b)-(d). In other words, we translated the SPAD array to all combinations of positions  $(x, y) = (L_i + \Delta_j, L_k + \Delta_l)$  for all combinations of  $L_i, L_k \in \{0, 4.8, 9.6, 14.4, 19.2, 24\}$  (tile positions) and  $\Delta_j, \Delta_k \in \{0, .0375, .0750, .1125\}$  (sub-pixel sampling) where all dimensions are in mm. This gave us a total imaging resolution of  $32 \times 5 \times 4 = 768$  pixels along each axis and required a total of  $5 \times 5 \times 4 \times 4 = 400$  total acquisitions to produce a resulting  $768 \times 768$  image. Although this required scanning, it was still significantly faster than raster scanning over single pixels which would require a total of  $768^2 = 518400$  acquisitions for the same resolution image; in addition, higher-resolution

SPAD arrays may be available once the technology is commercialized.

In order to obtain sufficient data for future analysis work in the short period of time with the SPAD array, we configured the SPAD to output a total of 16384 frames of data for each acquisition, which at  $65 \mu\text{s}$  per frame took 1.06 seconds.

The MATLAB user interface for the SPAD array was modified to automate the acquisition procedure and synchronously drive the translation stages to each of the 400 positions, outputting a separate data file for each position containing photon arrival data.

The original software for the SPAD array was configured to output the values of all SPAD registers at each acquisition frame, even in the event of no photon arrivals. However, since we operate in a low-flux regime where in any given frame, most pixels do not contain arrival data, this is an inefficient method of data storage, with each single acquisition occupying several gigabytes. In addition, the output of the SPAD array pixel data is not in logical pixel order due to limitations in the design of the electronics [72]. In order to speed up data processing, we developed a custom GNU C program (see Appendix B) to read the SPAD array binary files and output a cleaner, MATLAB-friendly file containing only a sequence of photon detections tagged by pixel number and time frame number. The C program also has both ASCII and binary output modes, that are conveniently and efficiently readable in MATLAB.

Mounted in front of the translatable SPAD array was a standard Canon FL-series photographic lens with a focal length of 55 mm and a maximum photographic aperture of f/1.2. We set the aperture of the lens to f/2.8 which provided the necessary depth of field to capture sufficient detail from various depth ranges of our object, increase sharpness, and reduce vignetting. The lens, designed for 35 mm film cameras, had an image circle of slightly larger than 35 mm, allowing us to mount the lens at a fixed position and conveniently fit our  $24 \times 24$  mm square imaging area entirely within the image circle of the lens. Basic tests in counting mode showed that at f/2.8, the lens was able to easily and clearly resolve objects as small as one single pixel in the  $768 \times 768$  pixel image with almost zero cross-talk, provided that the lens was manually focused correctly.

### 4.3.3 Computational reconstruction approach

Unlike first-photon imaging where we guarantee an arrival at every pixel, single-photon imaging using a SPAD array must use a single deterministic dwell time for the entire image. This has the following implications: for very dark regions it is possible that no photon arrivals will be measured (unlike first-photon imaging where an arrival is guaranteed by definition), while on the other hand, it is also possible that for bright regions, multiple arrivals will be measured in one dwell time period which can be used to gain additional information. Kirmani et. al. [66] adapted the same three-step algorithm above to the fixed-dwell time case which we briefly summarize here.

#### Reflectivity reconstruction

In first-photon imaging we reconstruct reflectivity using the number of laser pulses  $n(x, y)$  before the first detected photon and the fact that the maximum-likelihood estimate of the intensity based on this information is proportional to  $1/n$  based on Poisson statistics. In the case of a fixed dwell time of  $N$  laser pulses per pixel, we simply measure the total number of photon detections  $k(x, y)$  for each pixel and set adjust our log-likelihood function to

$$\mathcal{L}(\alpha(x, y)|k(x, y)) = \gamma [\alpha(x, y)S + BT_r] [N - k(x, y)] - k(x, y) \log [1 - \exp [-\gamma\alpha(x, y)S + BT_r]] \quad (4.17)$$

This function is also strictly convex in  $\alpha(x, y)$  and we proceed normally using the same computational reconstruction program for  $\hat{\alpha}(x, y)$  using the modified log-likelihood above.

#### Background noise rejection

Since for each pixel we obtain not exactly one arrival, but anywhere from 0 to several arrivals (in the low-flux regime we neglect the possibility that multiple arrivals occur in a single laser pulse), our background noise censoring needs to be adjusted accordingly. Kirmani et. al. [66] suggest that given a set of arrivals  $\{t_\ell(x, y)\}$  at pixel  $(x, y)$ , we compute the rank-ordered mean (ROM)  $t_{ROM}(x, y)$  which is the median value of the detection times of all the detections

acquired in the neighboring 8 pixels, setting  $t_{ROM}(x, y) = \infty$  in the case of missing data. Following this, the set of indices of uncensored detections  $U(x, y)$  at pixel  $(x, y)$  is defined by

$$U(x, y) = \left\{ \ell : |t_\ell(x, y) - t_{ROM}(x, y)| < 2T_p \left( \frac{BT_r}{\gamma\alpha(x, y)S + BT_r} \right), 0 \leq \ell < k(x, y) \right\} \quad (4.18)$$

Similar to first-photon imaging, this is dependent on the reflectivity estimate  $\hat{\alpha}(x, y)$  obtained from the result of the optimization in the first step.

### Depth reconstruction

We now proceed to depth reconstruction. If  $U(x, y)$  is non-empty, we set the log-likelihood function for depth reconstruction by summing over the log likelihoods of all uncensored detections:

$$L(Z(x, y) | \{t_\ell(x, y) | \ell \in U(x, y)\}) = - \sum_{\ell \in U(x, y)} \log \left[ s(t_\ell(x, y) - \frac{2Z(x, y)}{c}) \right] \quad (4.19)$$

If  $U(x, y)$  is empty, i.e. if after background censoring, no data is available for pixel  $(x, y)$ , we set the value of the log-likelihood function to 0 so that it does not contribute to the scene's overall log-likelihood cost function [66]. We then proceed with the optimization program for  $\hat{Z}(x, y)$  as before. Implementation of the optimization procedures for fixed dwell time imaging were also performed using the SPIRAL-TAP package for MATLAB.

#### 4.3.4 Preliminary results

Figures 4-15 shows the results of our reconstruction approach for data taken with the same mannequin used for first-photon imaging but wearing a T-shirt with larger text and a colored background. Figure 4-16 and 4-17 show results from two other scenes among several that were imaged. Although we took data with full  $4 \times 4$  subpixel scans ( $768 \times 768$  total image pixels), for this thesis we only analyzed data from  $2 \times 2$  subscans ( $384 \times 384$ ) as in the full

subscan data hot pixels appear in groups of  $4 \times 4$ ; this interferes with our sparsity-promoting regularization as they effectively get recognized and emphasized as  $4 \times 4$ -pixel features. A more advanced algorithm may be able to specifically recognize and mitigate this situation by performing aggressive range gating based on nearby pixel data when a  $4 \times 4$ -pixel group of hot pixels is detected.

#### 4.3.5 Comparison to first-photon imaging

We notice that for the reflectivity measurements, we see that similar to first-photon imaging, we obtain cleaner images. However unlike first-photon imaging, the dynamic range of reflectivity measurements using the SPAD array is limited, since in fixed dwell-time operation, if we tune the dwell time such that the bright regions receive on the order of  $\sim 1\text{-}5$  photons, we obtain almost no data for darker regions (including, for example, the black background cloth behind the mannequin) since the lack of any signal photon arrivals prevents us from gaining any information about reflectivity variations. This is in stark contrast to first-photon imaging in which an arrival at each pixel is guaranteed by definition (each pixel has a variable dwell time that ends upon a detection event). If we extend the dwell time long enough such that we receive at least one arrival for most pixels, we obtain clean images, but also note that in this case, there are sufficient arrivals in the bright regions to simply use traditional averaging with excellent results, reducing the need for a sparsity-based approach to reconstruct images.

The level of improvement obtained in fixed dwell time imaging is much less than that of first-photon imaging. We also confirmed this by post-processing data from the SPAD arrays to simulate first-photon imaging, in which we gather data for an extended period of time but only keep the first photon arrival at every pixel; the results are shown in Figure 4-18 for two scenes, demonstrating again the level of improvement seen using the raster scanning equipment earlier, including the ability to recover text that is almost illegible from the raw ML estimates.

Although the reflectivity images demonstrated some level of improvement using compu-

tational reconstruction, we found that with our imaging parameters and object size, it was difficult to obtain significant improvements in the depth maps. As shown in Figure 4-19, at a dwell time of 25 frames, there was simply not enough data in the image to obtain a depth map. This is because although pixels with no data provide us with valid information about reflectivity (the lack of arrivals at a pixel during a particular dwell time period can be interpreted as reflectivity information using Poisson statistics), in the case of depth ranging, no information is gained at all, causing the depth reconstruction stage to suffer.

On the other hand, when the dwell time was increased to  $\sim$ 400 frames or more, we obtained enough counts to form a higher-quality depth map, but computational reconstruction failed to extract significant features unseen in the raw data. We attribute this to a mismatch between the SPAD specifications, laser pulse width, and the imaging target. In contrast to our first-photon imaging experiment in which the time bin size of the HydraHarp is much smaller than the width of the laser pulse, in the SPAD imaging setup, the time bin size of the SPAD array was actually much longer than the laser pulse. This means that  $s(\cdot)$  is effectively only 1-2 time bins in size (in contrast to  $\sim$ 28 bins for our raster-scanning experiment) and an object with small features in the axial direction becomes nearly obliterated by the quantization error of the bin size. We expect that the particular SPAD array we used would lend itself to more fruitful depth reconstruction experiments if we used a laser pulse much longer than the time bin size, e.g. at least 1-2 ns, and a large object with depth features at least 1/10 of the pulse width. Under these conditions we expect to see a stronger difference between the depth-resolving capabilities of traditional imaging and our sparsity-based reconstruction technique.

## 4.4 Conclusions

In this chapter we explore imagers that use extremely low photon fluxes to capture three-dimensional structure and reflectivity information about an object. Such imagers have wide commercial applications including in medicine, military, and mobile applications. Current imaging technologies, including LIDAR, typically acquire and histogram hundreds of photon

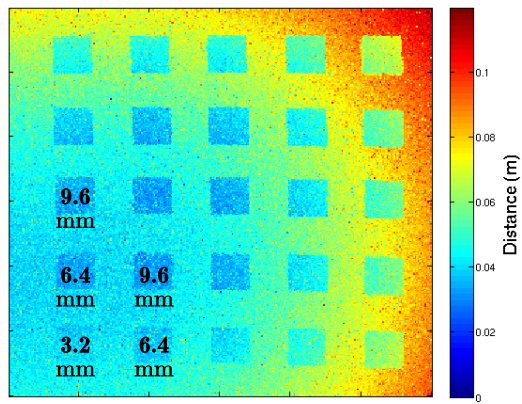
arrivals per pixel in order to accumulate a clean image.

These traditional imagers treat each pixel as an independent statistical process and ignore the spatial correlations between pixels that arise from piecewise smoothly-varying structures in real-world scenes. We present a novel imaging paradigm which is designed to take advantage of this property, captured well by sparsity in a wavelet transform basis, and computationally reconstructs the most likely image given a much smaller set of data.

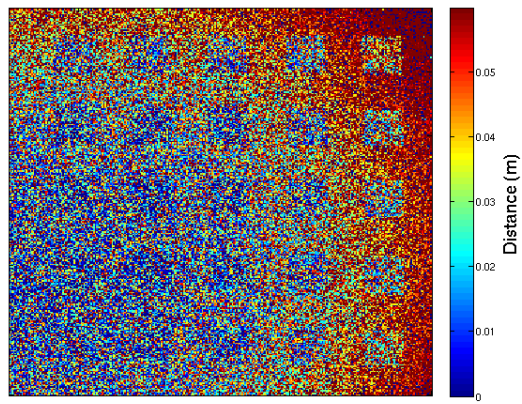
We experimentally demonstrate first-photon imaging, an active imaging method by which we only acquire the first photon arrival at every pixel before moving on to the next pixel. We demonstrate a similar level of resolution in both reflectivity and depth to images obtained using hundreds of photon arrivals, effectively improving the photon efficiency of our imager by a factor of  $\sim 100$ , which is crucial for remote sensing at longer distances with power-limited transmitters. It also enables us to reduce the active illumination power, which is of value in imaging sensitive biological samples, fluorescence-lifetime imaging, mobile devices, robotics, and military applications.

We also adapted our first-photon imaging technique to the case of fixed, deterministic dwell times in order to take advantage of recent developments in SPAD arrays with time-resolving photon detectors at every pixel, which enable an entire image to be acquired in parallel without raster scanning. We established a research collaboration with the Zappa group at the Politecnico di Milano using a prototype SPAD array. Preliminary results show improvements in reflectivity estimation. but we find that due to a mismatch between our laser pulse, SPAD array time resolution, and object size, we were not able to perform a thorough test of the method's capabilities.

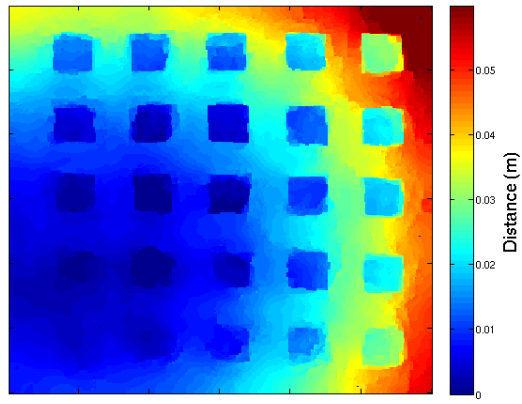
Future research in single-photon imaging may improve upon our methods in background light suppression, intelligent range gating, advances in detector technologies, as well as considering computational reconstruction to other forms of imaging or sensing in which sparsity and spatial structure can be exploited.



(a)

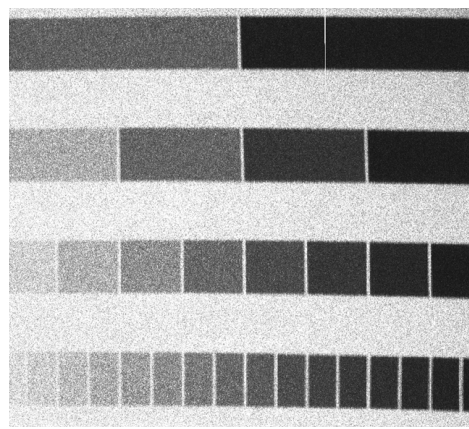


(b)

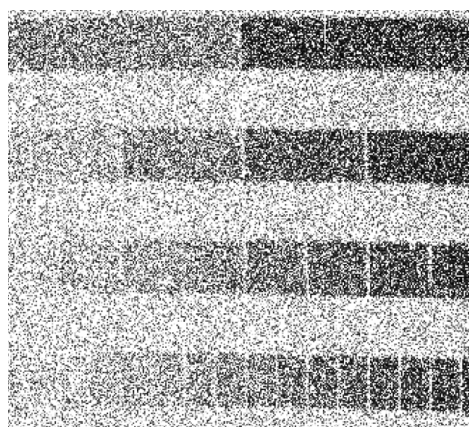


(c)

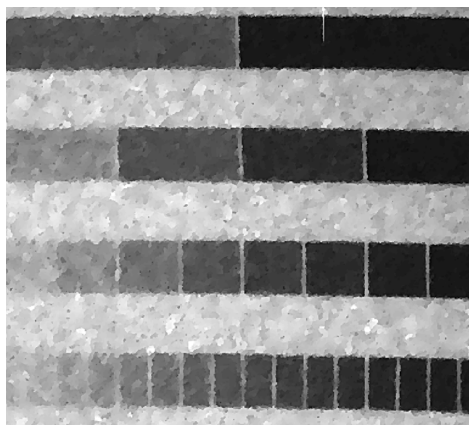
Figure 4-9: Depth chart test consisting of square features of linearly increasing height. (a) Image produced by traditional averaging with several hundred detections per pixel, (b) ML estimate using only the first photon arrival, and (c) data in (b) processed using our computational reconstruction method.



(a)

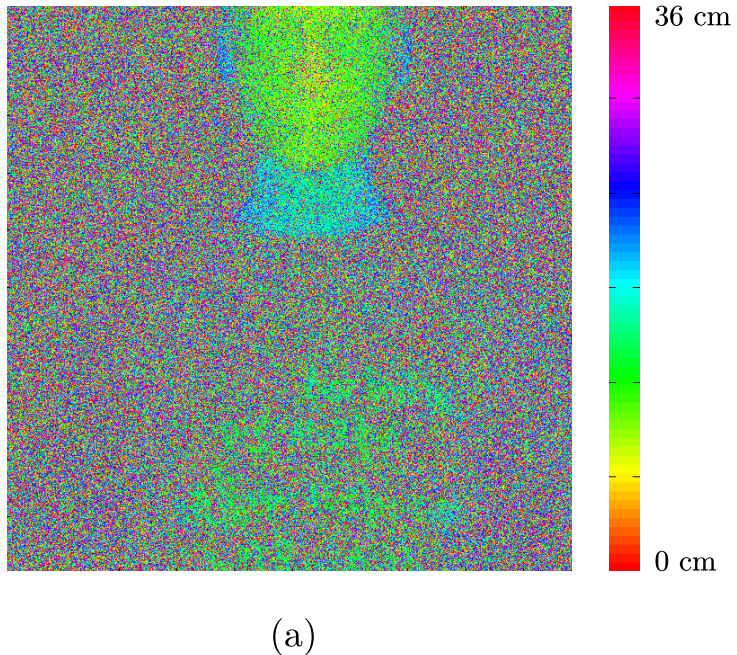


(b)



(c)

Figure 4-10: Reflectivity chart test. (a) Image produced by traditional averaging with several hundred detections per pixel, (b) ML estimate using only the first photon arrival, and (c) data in (b) processed using our computational reconstruction method.



(a)



(b)

Figure 4-11: (a) Raw depth values from a  $1000 \times 1000$ -pixel first-photon acquisition in the presence of high background noise, but range-gated to the indicated scale for visualization purposes. Evidence of high-reflectivity features on the T-shirt and face visually manifest as regions of coherent regions of color, which are the result of low variances in depth. (b) Reflectivity information gained from a version of (a) without range-gating. The number of pulses until the first detection was not used in this method.

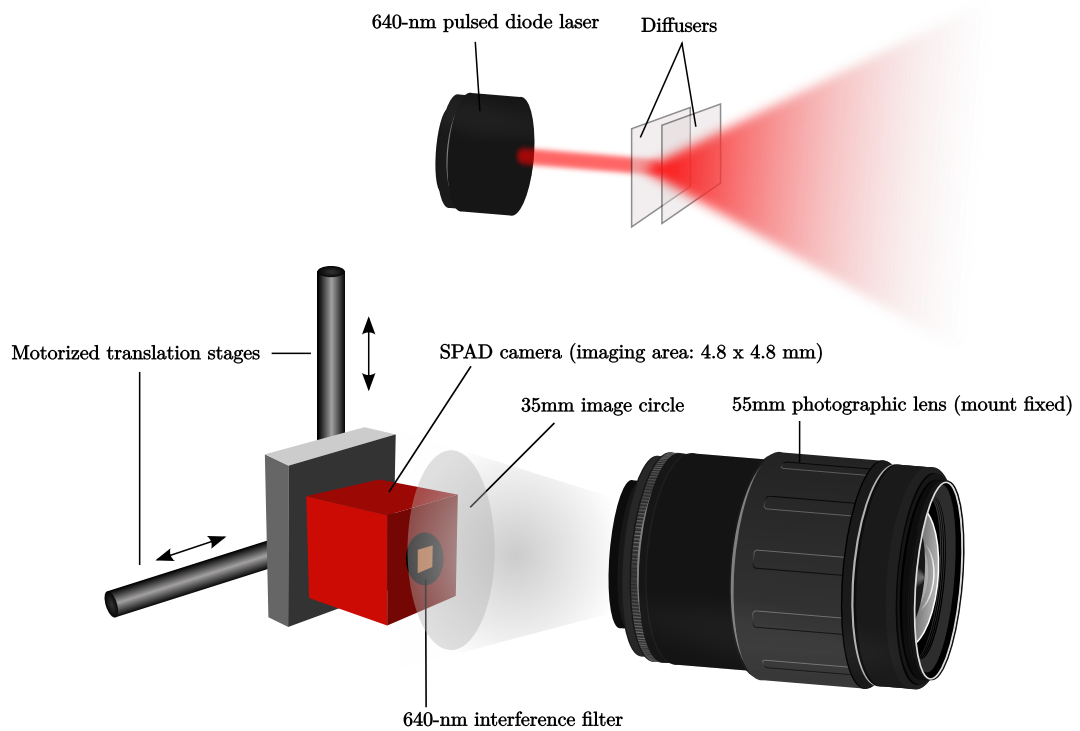


Figure 4-12: Experimental setup for single-photon imaging with a SPAD array. (TODO: Increase font size)

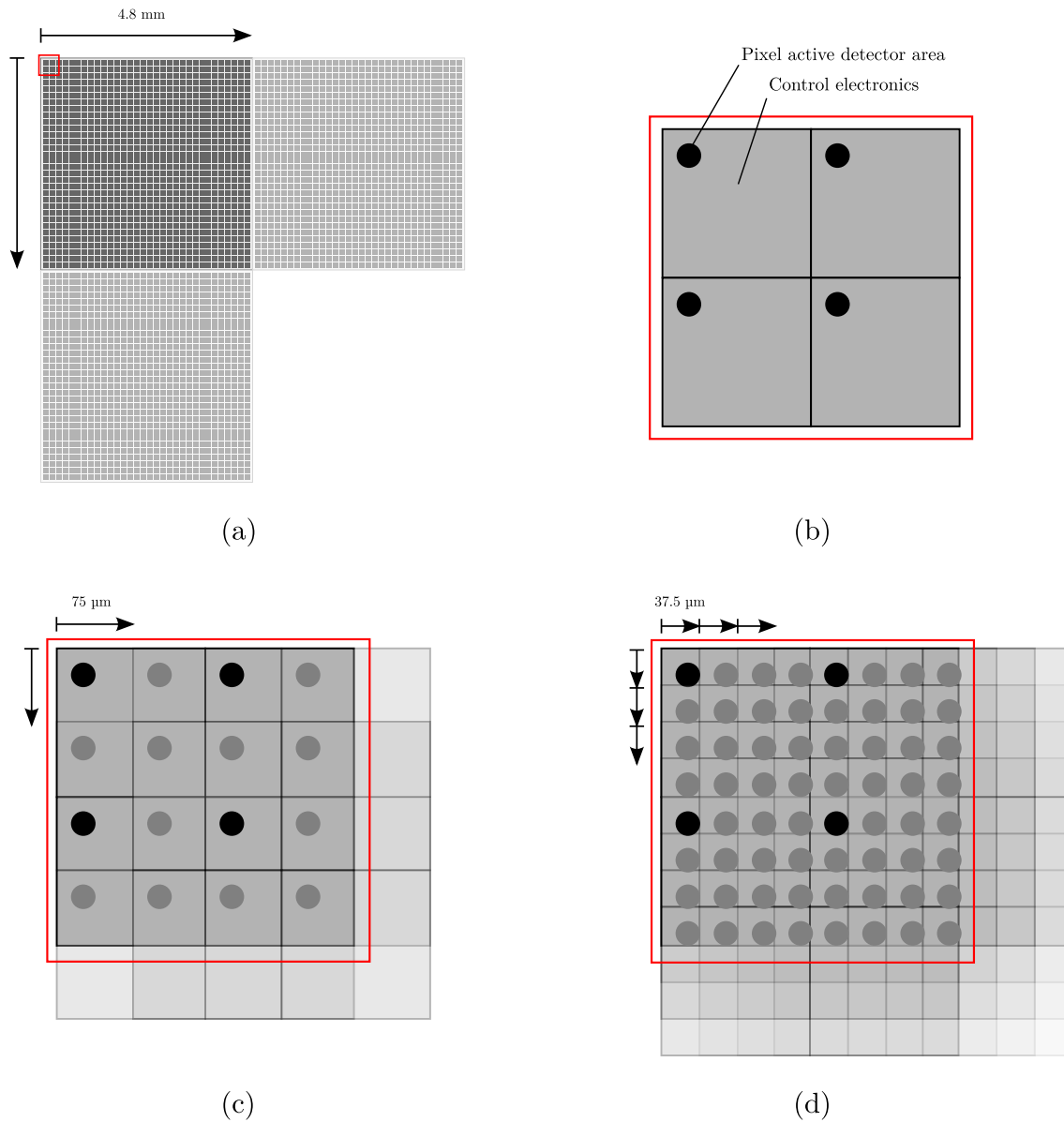


Figure 4-13: Scanning scheme to obtain high-resolution images using the  $32 \times 32$ -pixel SPAD array. (a) We translate the array by increments of a full array size (4.8 mm) along both axes to image multiple "tiles" of the entire array. (b) Zoom-in view of individual SPAD pixels showing the active area with no subpixel scanning, (c)  $2 \times 2$  subpixel scanning by translating along each axis by 75  $\mu\text{m}$ , multiplying the resolution by 2 and (d)  $4 \times 4$  subpixel scanning by translating along each axis by 37.5  $\mu\text{m}$ , 75  $\mu\text{m}$ , and 112.5  $\mu\text{m}$ , multiplying the resolution by 4.

1 image = 36 tiles



1 tile = 16 subpixel acquisitions



1 acquisition (1.06 s) = 16384 frames (each 65  $\mu$ s)



1 frame (65  $\mu$ s) = gate-on period (16  $\mu$ s) + gate-off period (49  $\mu$ s)



1 gate-on period (16  $\mu$ s) = 40 refolding windows (each 399 ns)



1 window (399 ns) = 1024 time bins (each 389.9 ps)



(8 laser pulses per window)

Figure 4-14: Terminology used in the describing the SPAD array imaging acquisition scheme.

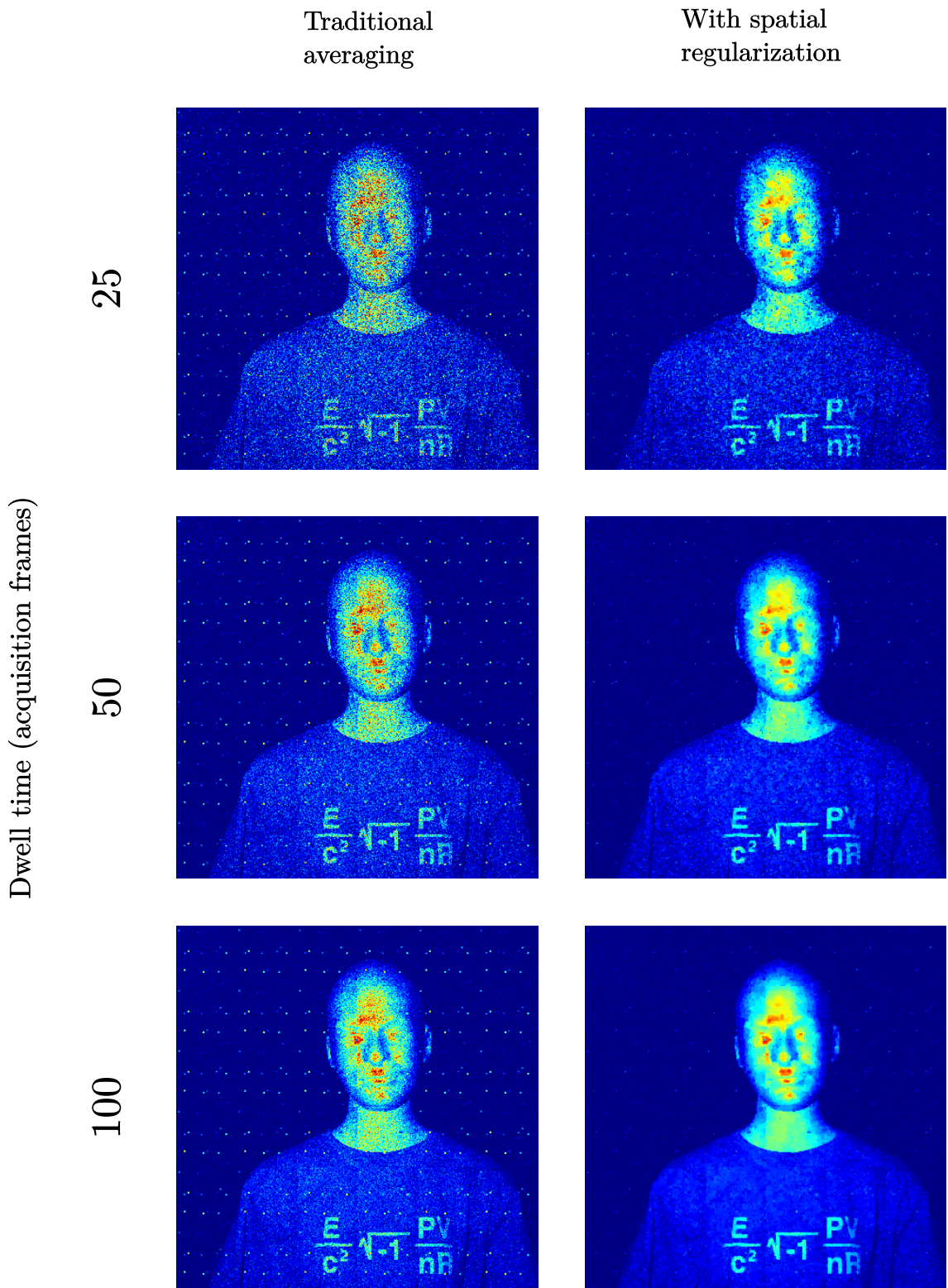


Figure 4-15: SPAD array imaging results for  $360 \times 360$ -pixel reflectivity images of a mannequin comparing traditional averaging with spatial regularization. Dwell times are in time units of acquisition frames (65  $\mu$ s).

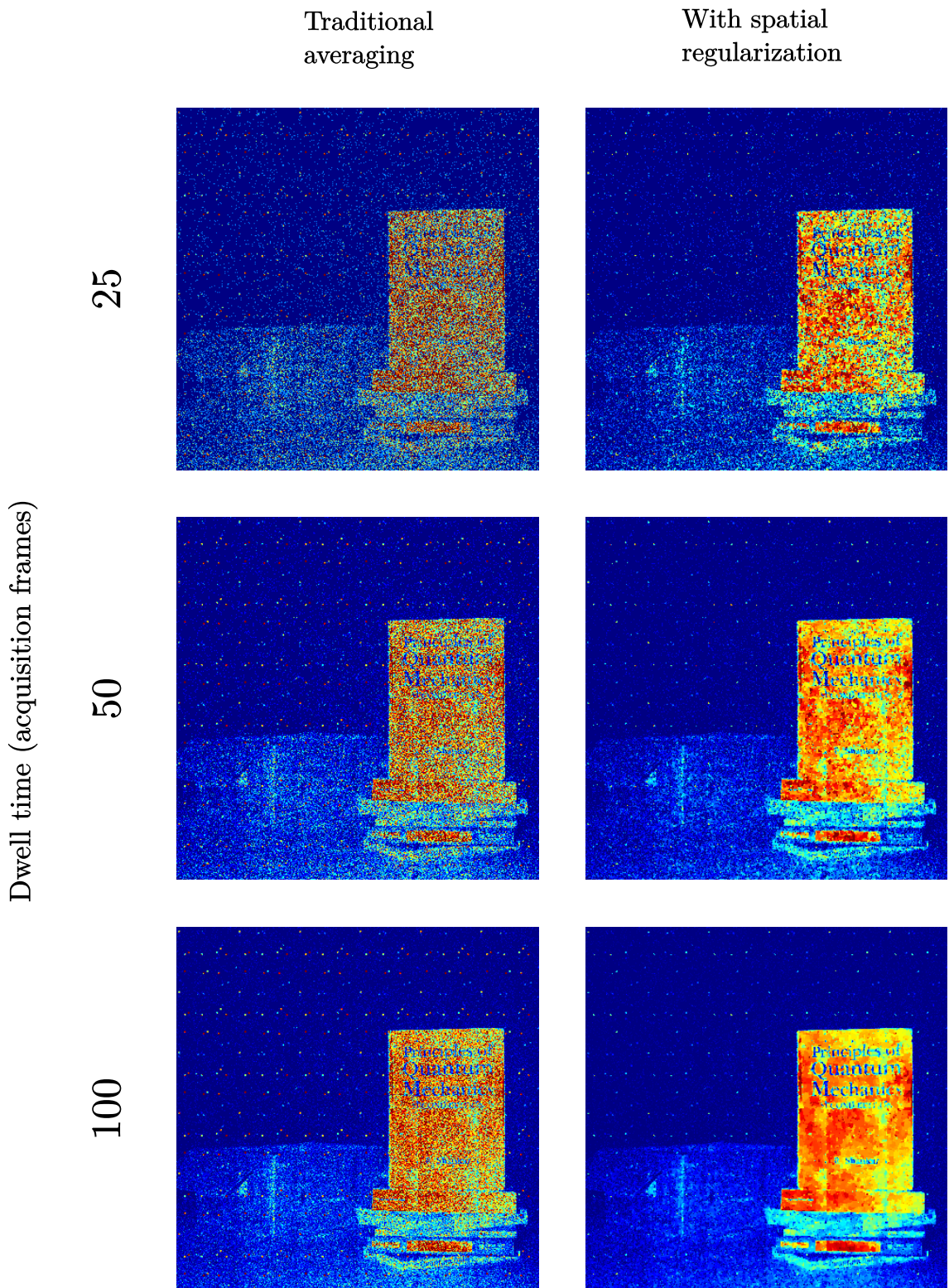


Figure 4-16: SPAD array imaging results for 360×360-pixel reflectivity images of a table, cardboard box, and books comparing traditional averaging with spatial regularization. Dwell times are in time units of acquisition frames (65  $\mu$ s).

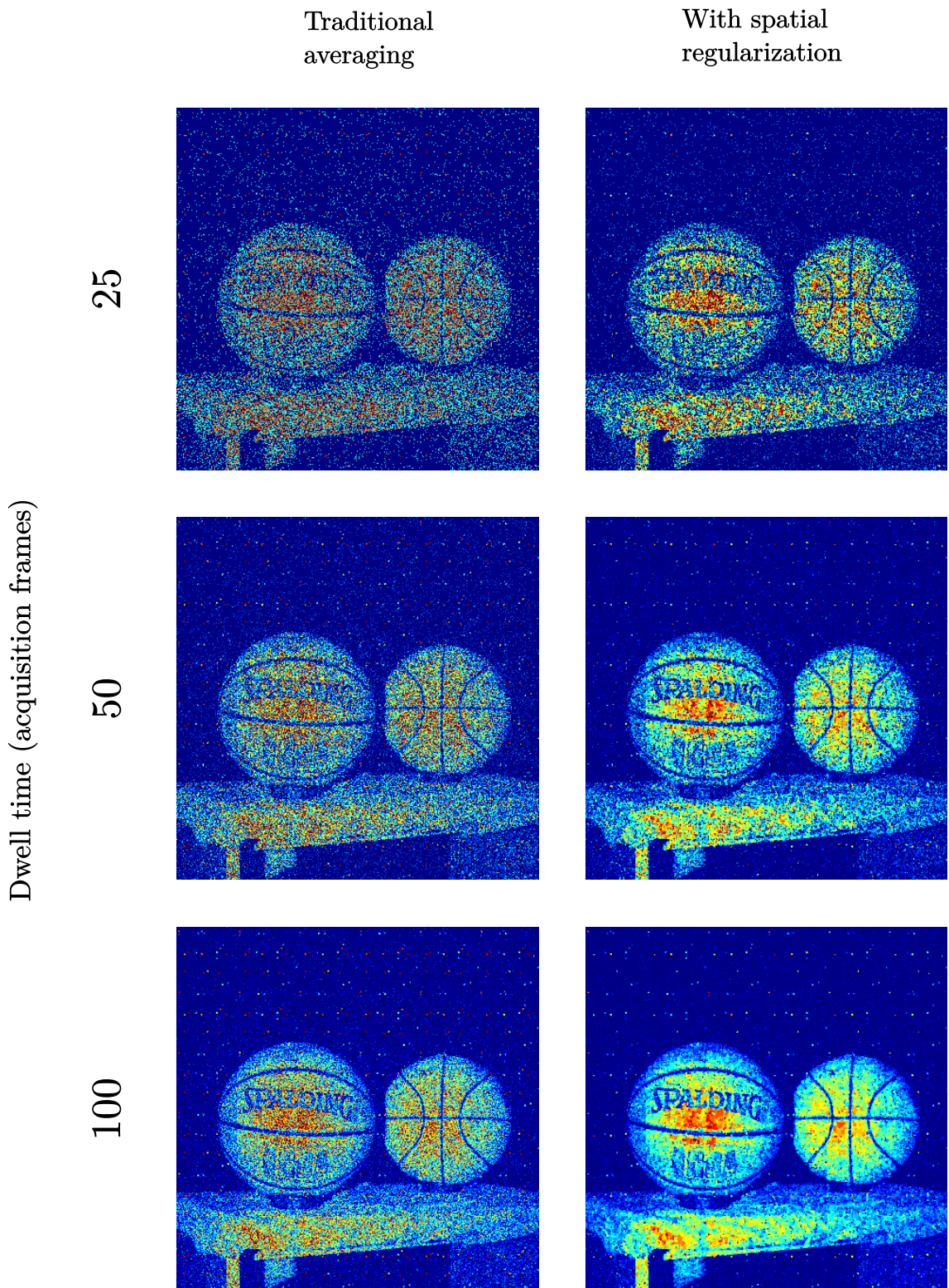


Figure 4-17: SPAD array imaging results for 360×360-pixel reflectivity images of two basketballs comparing traditional averaging with spatial regularization. Dwell times are in time units of acquisition frames (65  $\mu$ s).

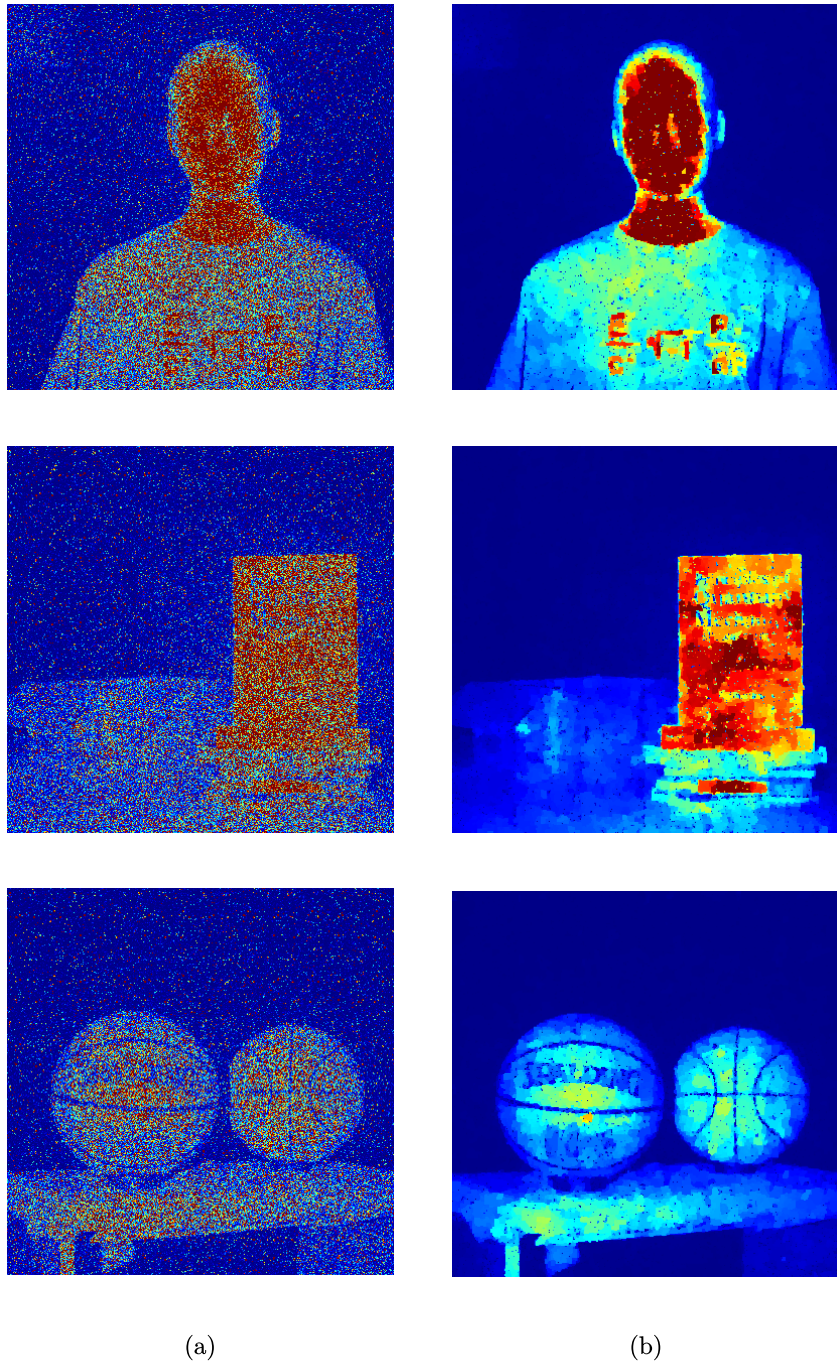


Figure 4-18: First-photon reflectivity imaging of three scenes simulated using the SPAD array, in which only the first arrival at each pixel is used regardless of subsequent arrivals within a fixed dwell time. (a) Traditional ML estimate of the reflectivity and (b) the same data after processing using our first-photon imaging technique described in the previous section. Depth results are not generated since  $s(\cdot)$  is nearly a delta function for the laser pulse width and time bin size used.

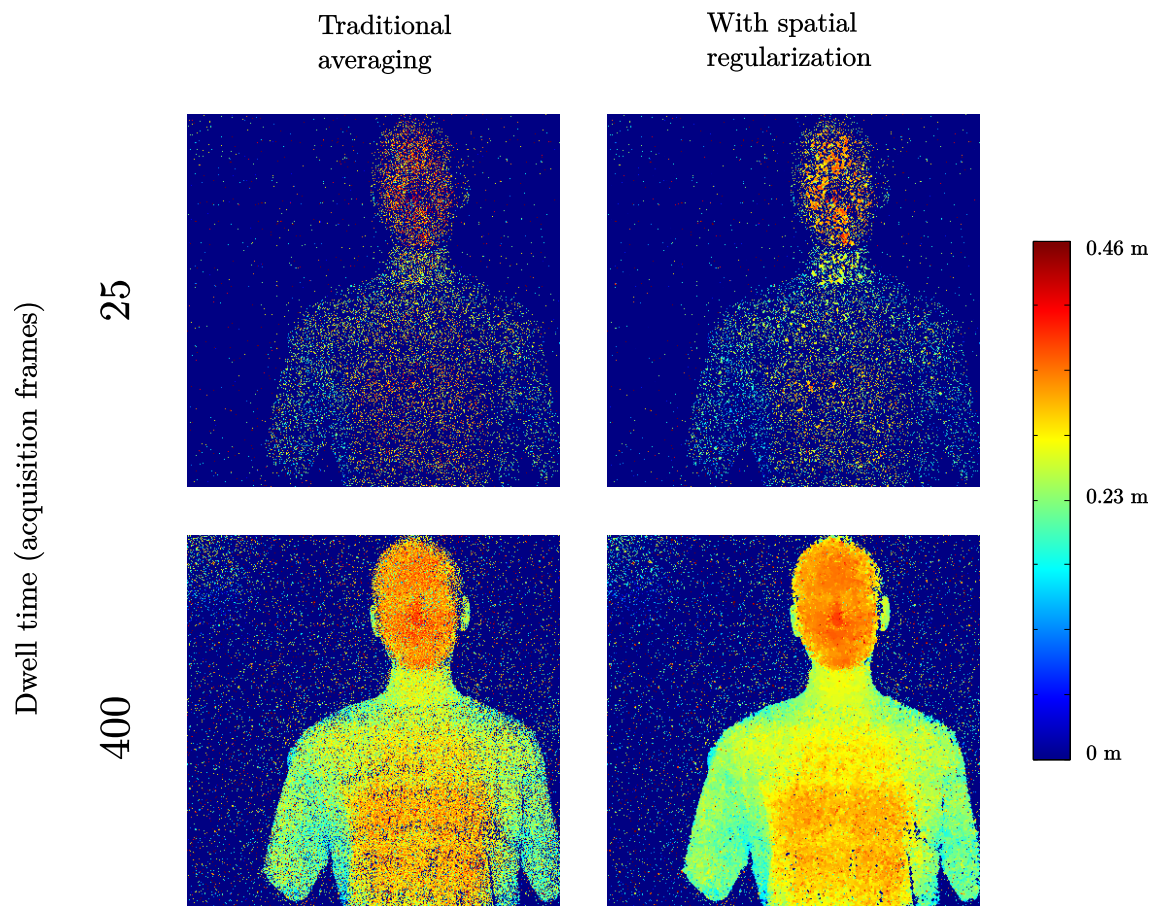


Figure 4-19: SPAD array imaging results for 360×360-pixel depth maps of a mannequin comparing traditional averaging with spatial regularization. Dwell times are in time units of acquisition frames ( $65 \mu\text{s}$ ). Pixels with no data are represented as depth values of 0.



# Chapter 5

## Conclusions

Quantum metrology, sensing, and imaging involve the use of nonclassical optical states or nonclassical detection schemes to obtain information about an object. Many of these configurations involve the use of entangled biphoton states in which the signal and idler arms, which cannot be described using semiclassical theories of light. Since the advent of quantum mechanics, a number of such configurations have been proposed and implemented, typically claiming measurement advantages over their classical counterparts, including resolution improvements, dispersion cancellation, and higher signal-to-noise ratios.

However, it is important to understand the fundamental principles that give rise to these advantages. In particular, although a particular experimental configuration may only be described by a strictly quantum description of light, that alone is not sufficient to justify that the claimed advantages are fundamentally quantum in nature, and that there does not exist a different, non-traditional classical experiment to achieve the same results. Such non-traditional experiments, which we refer to as quantum-mimetic, have been extensively analyzed over the past decade.

The primary motivation of this thesis has been to experimentally implement two of these quantum-mimetic configurations. In Chapter 2, we realized phase-conjugate OCT, which focuses on two advantages claimed of quantum OCT over classical OCT: a factor-of-2 axial resolution improvement and dispersion cancellation. As earlier theories showed that

these improvements arise not from the quantum nature of entangled photons but simply the phase-sensitive cross-correlations between the signal and idler beams, we used SPDC in the amplified regime to construct a classical phase-sensitive light source that did not have any entanglement, and successfully realized these two advantages. Future experiments in PC-OCT may add a transverse scanning mechanism as well as image targets with features at multiple depths. Experimentally, the most difficult aspect of this would be to perform the phase conjugation, which requires both precise transverse alignment as well as a pulsed pump that is aligned with the back-reflected signal in time. In addition, multi-path reflections within the target may necessitate additional signal processing steps before an OCT image can be recovered.

In Chapter 3, we turned to ghost imaging, another type of imaging initially thought to be exclusive to the quantum nature of entangled photons. Although earlier theoretical and experimental works showed that ghost imaging is possible to implement using thermal light and classical detectors, no prior works have attempted to perform ghost imaging using phase-sensitive classical light. We implemented such a phase-sensitive source using a pair of spatial light modulators driven deterministically with pseudorandom phase patterns, creating a new type of phase-sensitive classical light source different from the SPDC-based source used for ghost imaging. We successfully demonstrated the inverted image signature characteristic of far-field ghost images produced by quantum phase-sensitive sources, and also demonstrated that using classical sources and detectors it was possible to operate at much higher fluxes, speeding up acquisition from several hours to mere minutes.

Imaging using spatial light modulators driven with deterministic phases also provided us with an opportunity to replace the entire reference arm with a computational simulation, which we successfully demonstrated. In addition, we realized that ghost imaging using a spatial light modulator is conceptually similar to the a single-pixel camera, except that we use structured active illumination rather structured detection. Noting that our transmission masks were spatially sparse, having large continuous regions with few edges, we implemented compressive sensing methods on a simple beamsplitter-based, phase-insensitive ghost imaging

experiment, which afforded high-quality images while speeding up acquisition by up to a factor of 10 from traditional averaging methods.

Compressive sensing makes use of the fact that most real-world objects are piecewise continuous, and exploits the spatial correlations between adjacent pixels to computationally reconstruct an image using a small number of acquisitions. In Chapter 4, extended this concept beyond ghost imaging and considered its applications to mainstream imaging techniques. In particular, much attention recently has been focused on low-light reflectivity and depth imaging using Geiger-mode single photon counters, either by raster scanning the active illumination, or by employing detector arrays and imaging lenses in a camera-like configuration. In either case, current imaging technology requires collecting tens to hundreds of photon arrivals at each pixel in order to obtain a high-quality image. However, similar to what we discovered with ghost imaging, most real-world scenes contain spatial structure and correlations between adjacent pixels, making it inefficient to treat pixels as independent processes. We established a research collaboration with the Signal Transformation and Representation Group at MIT and jointly developed “first-photon imaging”, a novel low-light imaging paradigm in which we computationally reconstruct depth and reflectivity images using only the first photon arrival at each pixel, providing a factor-of-100 acquisition speedup over existing imagers using single-photon counters.

We also began the exploration of adapting our algorithm to the case of SPAD arrays, which are a current active area of research and may eventually replace the need to raster-scan an image. Since in this case an entire image has a constant dwell time across all pixels, in contrast to the variable dwell time used for first-photon imaging, our reconstruction algorithm needed to be adapted accordingly. We presented preliminary results using a prototype produced by the Zappa group at the Politecnico di Milano. However, noting that the time resolution of these detectors was not a good fit for our laser pulse width and object feature size, future experiments may consider tweaking these parameters and imaging more suitable objects to better demonstrate the potential of our fixed-dwell time algorithm. Future SPAD arrays may also consider improvements in fill-factor, either by array design or through the

use of microlenses, which would further improve acquisition speed. In addition, we hope that the future of SPAD array research brings higher-resolution arrays, both in number of pixels as well as time-bin resolution, which would hold immense possibilities for practical applications in biotechnology, medicine, mobile devices, space exploration, and military imaging, all of which have constraints on photon flux either in illumination or detection.

# Appendices



# Appendix A

## HydraHarp file converter

This GNU C-compatible code converts the raw output files of HydraHarp .ht3 files into a MATLAB-friendly ASCII format.

```
// File: ht3read.c
//
// Hydrapharp ht3 reader
// Based on sample Borland C code by PicoQuant
// Translated to GNU C by Dheera Venkatraman
// with additional features added for first-photon imaging
//
// Usage: ht3read [options] infile.ht3 outfile.txt
//
// Options:
// -nmax N      Only output N photon detections after each marker
// -tmin TMIN   Enable range-gating with minimum time bin TMIN
// -tmax TMAX   Enable range-gating with maximum time bin TMAX
// +s, -s       Enable/disable printing of arrivals before the first marker
// +m, -m       Print markers
// +o, -o       Print overflows
// +h, -h       Print headers with device and acquisition information

#include<stdio.h>
#include<string.h>
#include<stddef.h>
#include<stdlib.h>
#include<inttypes.h>

#define DISPCURVES 8 // not relevant in TT modes but needed in file header definition
```

```

#define MAXINPCHANS 8
#define T3WRAPAROUND 1024

#pragma pack(8) //structure alignment to 8 byte boundaries

typedef struct {
    float Start;
    float Step;
    float End;
} tParamStruct;

typedef struct {
    int MapTo;
    int Show;
} tCurveMapping;

typedef struct {
    int ModelCode;
    int VersionCode;
} tModuleInfo;

typedef union {
    uint32_t allbits;
    struct {
        unsigned nsync:10; // number of sync periods
        unsigned dtime:15; // delay from last sync in units of chosen resolution
        unsigned channel:6; // detection channel
        unsigned special:1;
    } bits;
} tT3Rec;

// The following represents the readable ASCII file header portion.

struct {
    char Ident[16];           // "HydraHarp"
    char FormatVersion[6];    // file format version
    char CreatorName[18];     // acquisition software name
    char CreatorVersion[12];  // acquisition software version
    char FileTime[18];
    char CRLF[2];
    char CommentField[256];
} TxtHdr;

```

```

// The following is binary file header information indentical to that in HHD files.
// Note that some items are not meaningful in the time tagging modes.

struct {
    int Curves;
    int BitsPerRecord; // data of one event record has this many bits
    int ActiveCurve;
    int MeasMode;
    int SubMode;
    int Binning;
    double Resolution; // in ps
    int Offset;
    int Tacq;           // in ms
    int StopAt;
    int StopOnOvfl;
    int Restart;
    int DispLinLog;
    int DispTimeFrom; // 1 ns steps
    int DispTimeTo;
    int DispCountsFrom;
    int DispCountsTo;
    tCurveMapping DispCurves[DISPCURVES];
    tParamStruct Params[3];
    int RepeatMode;
    int RepeatsPerCurve;
    int RepeatTime;
    int RepeatWaitTime;
    char ScriptName[20];
} BinHdr;

// Hardware information header

struct {
    char HardwareIdent[16];
    char HardwarePartNo[8];
    int HardwareSerial;
    int nModulesPresent;
    tModuleInfo ModuleInfo[10]; // upto 10 modules can be combined into a single file
    double BaseResolution;
    unsigned long long int InputsEnabled; // a bitfield
    int InpChansPresent; // determines the number of ChannelHeaders below!
    int RefClockSource;
}

```

```

int ExtDevices;      // a bitfield
int MarkerSettings; // a bitfield
int SyncDivider;
int SyncCFDLevel;
int SyncCFDZeroCross;
int SyncOffset;
} MainHardwareHdr;

// How many of the following array elements are actually present in the file
// is indicated by InpChansPresent above. Here we allocate the possible maximum.

struct {
    int InputModuleIndex; // module that corresponds to current channel
    int InputCFDLevel;
    int InputCFDZeroCross;
    int InputOffset;
} InputChannelSettings[MAXINPCHANS];

// Up to here the header was identical to that of HHD files.
// The following header sections are specific for the TT modes

// How many of the following array elements are actually present in the file
// is indicated by InpChansPresent above. Here we allocate the possible maximum.

int InputRate[MAXINPCHANS];

// the following exists only once

struct {
    int SyncRate;
    int StopAfter;
    int StopReason;
    int ImgHdrSize;
    unsigned long long int nRecords;
} TTTRHdr;

// how many of the following ImgHdr array elements are actually present in the file
// is indicated by ImgHdrSize above.
// Storage must be allocated dynamically if ImgHdrSize other than 0 is found.
//
        int ImgHdr[ImgHdrSize];

// The headers end after ImgHdr. Following in the file are only event records.
// How many of them actually are in the file is indicated by nRecords in TTTRHdr above.

```

```

int main(int argc, char* argv[]) {
    int result;
    FILE* fpin;
    FILE* fpout;
    int i;
    tT3Rec T3Rec;
    unsigned long long int lastmarker[20]={0,0,0,0,0,0,0,0,0,0,0,0,0,0,0,0,0,0,0,0};
    unsigned long long int n, truensync=0, oflcorrection = 0;

    unsigned long long int marker_total=0;
    unsigned long long int dtime_total=0;

    int print_headers=0; // print headers or not
    int print_overflow=0; // print overflows or not
    int print_marker=1; // print markers or not
    int print_start=0; // print counts arriving before first marker?
    long long int print_nmax=-1; // print first N counts after each marker (-1 for all)
    long long int print_n=-1;
    char infile[512];
    char outfile[512];

    long long int print_tmin=-1; // range-gating minimum time bin index
    long long int print_tmax=-1; // range-gating maximum time bin index

    unsigned long long int total_m=0; // total number of markers
    unsigned long long int total_o=0; // total number of overflows
    unsigned long long int total_c=0; // total number of counts

    if(argc<3) {
        fprintf(stderr,"Usage: ht3read [options] infile.ht3 outfile.txt\n\n");
        fprintf(stderr,"Options:\n");
        fprintf(stderr,"-nmax N      Only output N photon detections after each marker\n");
        fprintf(stderr,"-tmin TMIN   Enable range-gating with minimum time bin TMIN\n");
        fprintf(stderr,"-tmax TMAX   Enable range-gating with maximum time bin TMAX\n");
        fprintf(stderr,"+s, -s      Enable/disable printing of arrivals before the first marker\n");
        fprintf(stderr,"+m, -m      Print markers\n");
        fprintf(stderr,"+o, -o      Print overflows\n");
        fprintf(stderr,"+h, -h      Print headers with device and acquisition information\n");
        exit(-1);
    }

    for(i=1;i<argc-2;i++) {

```

```

if(strcmp(argv[i-1], "-nmax")==0) {
    print_nmax=atoi(argv[i]);
    if(print_nmax<-1) {
        fprintf(stderr,"error: number of counts out of bounds\n");
        exit(1);
    }
    fprintf(stdout,"(Printing only %lld counts per marker)\n",print_nmax);
}
else if(strcmp(argv[i],"-nmax")==0) {}
else if(strcmp(argv[i-1],"-tmin")==0) {
    print_tmin=atoi(argv[i]);
    if(print_tmin<-1) {
        fprintf(stderr,"error: tmin out of bounds\n");
        exit(1);
    }
    fprintf(stdout,"(Printing only time bins >= %lld)\n",print_tmin);
}
else if(strcmp(argv[i],"-tmin")==0) {}
else if(strcmp(argv[i-1],"-tmax")==0) {
    print_tmax=atoi(argv[i]);
    if(print_tmax<-1) {
        fprintf(stderr,"error: tmax out of bounds\n");
        exit(1);
    }
    fprintf(stdout,"(Printing time bins <= %lld)\n",print_tmax);
}
else if(strcmp(argv[i],"-tmax")==0) {}
else if(strcmp(argv[i],"-h")==0) print_headers=0;
else if(strcmp(argv[i],"+h")==0) print_headers=1;
else if(strcmp(argv[i],"-s")==0) print_start=0;
else if(strcmp(argv[i],"+s")==0) print_start=1;
else if(strcmp(argv[i],"-m")==0) print_marker=0;
else if(strcmp(argv[i],"+m")==0) print_marker=1;
else if(strcmp(argv[i],"-o")==0) print_overflow=0;
else if(strcmp(argv[i],"+o")==0) print_overflow=1;
else {
    fprintf(stderr,"error: invalid option %s\n",argv[i]);
    exit(1);
}

if((fpin=fopen(argv[argc-2],"rb"))==NULL) {
    fprintf(stderr,"error: input file cannot be opened, aborting.\n");
}

```

```

    exit(1);
}

if((fpout=fopen(argv[argc-1],"w"))==NULL) {
    fprintf(stderr,"error: output file cannot be opened, aborting.\n");
    exit(1);
}

fprintf(stdout,"Loading data from %s ...\\n", argv[argc-2]);
fprintf(stdout,"Writing output to %s ...\\n", argv[argc-1]);
result = fread( &TxtHdr, 1, sizeof(TxtHdr) ,fpin);
if(result!=sizeof(TxtHdr)) {
    fprintf(stderr,"error: cannot read text header\\n");
    exit(1);
}

if(print_headers) {
    fprintf(fpout,"%% Ident : %.*s\\n",
            (int)sizeof(TxtHdr.Ident),TxtHdr.Ident);
    fprintf(fpout,"%% Format Version : %.*s\\n",
            (int)sizeof(TxtHdr.FormatVersion),TxtHdr.FormatVersion);
    fprintf(fpout,"%% Creator Name : %.*s\\n",
            (int)sizeof(TxtHdr.CreatorName),TxtHdr.CreatorName);
    fprintf(fpout,"%% Creator Version : %.*s\\n",
            (int)sizeof(TxtHdr.CreatorVersion),TxtHdr.CreatorVersion);
    fprintf(fpout,"%% Time of Creation : %.*s\\n",
            (int)sizeof(TxtHdr.FileTime),TxtHdr.FileTime);
    fprintf(fpout,"%% File Comment : %.*s\\n",
            (int)sizeof(TxtHdr.CommentField),TxtHdr.CommentField);
}

if(strncmp(TxtHdr.FormatVersion,"1.0",3)&&strncmp(TxtHdr.FormatVersion,"2.0",3)) {
    if(print_headers) {
        fprintf(stderr,
                "error: File format version is %s. This program is for version 1.0 and 2.0 only.\\n",
                TxtHdr.FormatVersion);
    }
    exit(1);
}

result = fread( &BinHdr, 1, sizeof(BinHdr) ,fpin);
if(result!=sizeof(BinHdr)) {
    fprintf(stderr,"error: cannot read bin header, aborted.\\n");
    exit(1);
}

```

```

}

if(print_headers) {
    fprintf(fpout,"%% Bits per Record      : %d\n",BinHdr.BitsPerRecord);
    fprintf(fpout,"%% Measurement Mode   : %d\n",BinHdr.MeasMode);
    fprintf(fpout,"%% Sub-Mode           : %d\n",BinHdr.SubMode);
    fprintf(fpout,"%% Binning             : %d\n",BinHdr.Binning);
    fprintf(fpout,"%% Resolution          : %lf\n",BinHdr.Resolution);
    fprintf(fpout,"%% Offset              : %d\n",BinHdr.Offset);
    fprintf(fpout,"%% AcquisitionTime     : %d\n",BinHdr.Tacq);
}

// Note: for formal reasons the BinHdr is identical to that of HHD files.
// It therefore contains some settings that are not relevant in the TT modes,
// e.g. the curve display settings. So we do not write them out here.

result = fread( &MainHardwareHdr , 1, sizeof(MainHardwareHdr) ,fpin);
if(result!=sizeof(MainHardwareHdr)) {
    fprintf(stderr,"error: cannot read MainHardwareHdr, aborted.\n");
    exit(1);
}

if(print_headers) {
    fprintf(fpout,"%% HardwareIdent       : %.*s\n",
            (int)sizeof(MainHardwareHdr.HardwareIdent),MainHardwareHdr.HardwareIdent);
    fprintf(fpout,"%% HardwarePartNo      : %.*s\n",
            (int)sizeof(MainHardwareHdr.HardwarePartNo),MainHardwareHdr.HardwarePartNo);
    fprintf(fpout,"%% HardwareSerial        : %d\n",MainHardwareHdr.HardwareSerial);
    fprintf(fpout,"%% nModulesPresent      : %d\n",MainHardwareHdr.nModulesPresent);
}

// the following module info is needed for support enquiries only
for(i=0;i<MainHardwareHdr.nModulesPresent;++i) {
    if(print_headers) {
        fprintf(fpout,"%% Moduleinfo[%02d]      : %08x %08x\n",
                i, MainHardwareHdr.ModuleInfo[i].ModelCode, MainHardwareHdr.ModuleInfo[i].VersionCode);
    }
}

//the following are important measurement settings
if(print_headers) {
    fprintf(fpout,"%% BaseResolution        : %lf\n",MainHardwareHdr.BaseResolution);
    fprintf(fpout,"%% InputsEnabled         : %llu\n",MainHardwareHdr.InputsEnabled);
    fprintf(fpout,"%% InpChansPresent       : %d\n",MainHardwareHdr.InpChansPresent);
}

```

```

        fprintf(fpout,"%% RefClockSource      : %d\n",MainHardwareHdr.RefClockSource);
        fprintf(fpout,"%% ExtDevices        : %x\n",MainHardwareHdr.ExtDevices);
        fprintf(fpout,"%% MarkerSettings    : %x\n",MainHardwareHdr.MarkerSettings);
        fprintf(fpout,"%% SyncDivider       : %d\n",MainHardwareHdr.SyncDivider);
        fprintf(fpout,"%% SyncCFDLevel      : %d\n",MainHardwareHdr.SyncCFDLevel);
        fprintf(fpout,"%% SyncCFDZeroCross  : %d\n",MainHardwareHdr.SyncCFDZeroCross);
        fprintf(fpout,"%% SyncOffset         : %d\n",MainHardwareHdr.SyncOffset);
    }

for(i=0;i<MainHardwareHdr.InpChansPresent;++i) {
    if(print_headers) {
        fprintf(fpout,"%% -----\\n");
    }
    result = fread( &(InputChannelSettings[i]), 1, sizeof(InputChannelSettings[i]) ,fpin);
    if(result!=sizeof(InputChannelSettings[i])) {
        printf("\nerror reading InputChannelSettings, aborted.");
        exit(1);
    }
    if(print_headers) {
        fprintf(fpout,"%% Input Channel %1d\\n",i);
        fprintf(fpout,"%%   InputModuleIndex   : %d\\n",InputChannelSettings[i].InputModuleIndex);
        fprintf(fpout,"%%   InputCFDLevel      : %d\\n",InputChannelSettings[i].InputCFDLevel);
        fprintf(fpout,"%%   InputCFDZeroCross  : %d\\n",InputChannelSettings[i].InputCFDZeroCross);
        fprintf(fpout,"%%   InputOffset         : %d\\n",InputChannelSettings[i].InputOffset);
    }
}

if(print_headers) {
    fprintf(fpout,"%% -----\\n");
}
for(i=0;i<MainHardwareHdr.InpChansPresent;++i) {
    result = fread( &(InputRate[i]), 1, sizeof(InputRate[i]) ,fpin);
    if(result!=sizeof(InputRate[i])) {
        fprintf(stderr,"error reading InputRates, aborted\\n");
        exit(1);
    }
    if(print_headers) {
        fprintf(fpout,"%% Input Rate [%1d]      : %1d\\n",i,InputRate[i]);
    }
}

if(print_headers) {

```

```

    fprintf(fpout,"%% -----\\n");
}

result = fread( &TTTRHdr , 1, sizeof(TTTRHdr) ,fpin);
if(result!=sizeof(TTTRHdr)) {
    fprintf(stderr,"error: error reading TTTRHdr, aborted\\n");
    exit(1);
}

if(print_headers) {
    fprintf(fpout,"%% SyncRate           : %d\\n",TTTRHdr.SyncRate);
    fprintf(fpout,"%% StopAfter          : %d\\n",TTTRHdr.StopAfter);
    fprintf(fpout,"%% StopReason         : %d\\n",TTTRHdr.StopReason);
    fprintf(fpout,"%% ImgHdrSize        : %d\\n",TTTRHdr.ImgHdrSize);
    fprintf(fpout,"%% nRecords          : %llu\\n",TTTRHdr.nRecords);
    fprintf(fpout,"%% -----\\n");
}

// Imaging header only relevant for PicoQuanta-proprietary imaging devices
fseek(fpin,TTTRHdr.ImgHdrSize*4,SEEK_CUR);

// Read and interpret the event records
for(n=0;n<TTTRHdr.nRecords;n++) {
    i=0;
    result = fread(&T3Rec.allbits,sizeof(T3Rec.allbits),1,fpin);
    if(result!=1) {
        if(feof(fpin)==0) {
            fprintf(stderr,"error: error in input file\\n");
            exit(1);
        }
    }

    if(T3Rec.bits.special==1) {
        if(T3Rec.bits.channel==0x3F) { // overflow
            if(print_overflow) {
                fprintf(fpout,"%llu 2 0 0 0\\n", n);
                total_o++;
            }
            if(T3Rec.bits.nsSync==0)
                oflCorrection+=T3WRAPAROUND;
            else
                oflCorrection+=T3WRAPAROUND*T3Rec.bits.nsSync;
        }
    }
}

```

```

}

if((T3Rec.bits.channel>=1)&&(T3Rec.bits.channel<=15)) { // marker
    truensync = oflcorrection + T3Rec.bits.nsync;
    // the time unit depends on sync period which can be obtained from the file header
    if(print_marker && (lastmarker[T3Rec.bits.channel]==0 ||
        (truensync>lastmarker[T3Rec.bits.channel] &&
        truensync-lastmarker[T3Rec.bits.channel]>5))) {
        fprintf(fpout,"%llu 0 %02x %llu %llu\n", n, T3Rec.bits.channel, marker_total, dtime_total);
        total_m++;
        marker_total=0;
        dtime_total=0;
        print_n=0;
    }
    lastmarker[T3Rec.bits.channel]=truensync;
}
} else { // regular input channel
    if((print_start||print_n!=-1) && (print_nmax==-1||print_n<print_nmax)) {
        truensync = oflcorrection + T3Rec.bits.nsync;
        // the nsync time unit depends on sync period which can be obtained from the file header
        // the dtime unit depends on the resolution and can also be obtained from the file header
        if( (print_tmin==-1 || T3Rec.bits.dtime>=print_tmin)
            && (print_tmax==-1 || T3Rec.bits.dtime<=print_tmax)) {
            fprintf(fpout,"%llu 1 %02x %llu %u\n", n, T3Rec.bits.channel, truensync, T3Rec.bits.dtime);
            print_n++;
            total_c++;
        }
        if( (print_tmin==-1 || T3Rec.bits.dtime>=print_tmin)
            && (print_tmax==-1 || T3Rec.bits.dtime<=print_tmax)) {
            dtime_total+=T3Rec.bits.dtime;
            marker_total++;
        }
    }
    if(n%100000==0) {
        fprintf(stdout,"[%llu%%] Total printed records: M %llu / O %llu / C %llu\r",
            100*n/TTTRHdr.nRecords,total_m,total_o,total_c);
        fflush(stdout);
    }
}
fprintf(stdout,"[100%%] Total printed records: M %llu / O %llu / C %llu\n\n",
    total_m,total_o,total_c);

fclose(fpin);

```

```
fclose(fpout);

exit(0);
return(0);
}
```

# Appendix B

## SPAD file converter

This GNU C-compatible code converts the raw output files of the Politecnico di Milano SPAD array to a MATLAB-friendly ASCII or Binary file containing only photon arrivals along with their pixel number and time frame number.

```
// File: spadcounts.c
//
// Data reader for 32x32 photon counting array from Politecnico di Milano
// Written by Dheera Venkatraman
//
// Usage: spadcounts [options] myfile.bin
//
// Options:
// -a          ASCII output
// -b          binary output (default)
// -o file.out output to filename.out
// -s N        new output file every N frames
//
// Output:
//
// For ASCII mode: Text lines, one for each photon arrival, formatted as
// [frame number (0-16383N)] [pixel number (0-1024)] [time bin number (0-1024)]
//
// For binary mode: 64-bit records, one for each photon arrival, formatted as
// [frame number (32 bits)] [pixel number (16 bits)] [time bin number (16 bits)]
//
// (The pixel number and time bin number in principle need only 10 bits each but
// by byte-aligning records we are able to read files much faster in MATLAB.)
```

```

#include<stdio.h>
#include<string.h>
#include<stddef.h>
#include<stdlib.h>
#include<inttypes.h>

FILE* fopen64(const char *filename, const char *type);

typedef struct {
    unsigned int t[1024];
} spadFrame;

typedef union {
    uint16_t allbits;
    struct {
        unsigned short int coarse:6;
        unsigned short int fine:4;
        unsigned short int zero:6;
    } bits;
    struct {
        unsigned short int byte0:8;
        unsigned short int byte1:8;
    } bytes;
} spadRecord;

typedef union {
    uint16_t allbits[18];
    struct {
        uint16_t dummy0[3];
        unsigned short int stop:4;
        unsigned short int dummy1:4;
        unsigned short int dummy2:4;
        unsigned short int dummy3:4;
        uint16_t dummy4[14];
    } bits;
} spadStop;

const int FORMAT_ASCII = 0;
const int FORMAT_BINARY = 1;

int main(int argc, char* argv[]) {
    FILE* infile;

```

```

FILE* outfile;
int result;
unsigned int i;
unsigned long int j;
char c;
uint64_t outrec;

spadRecord raw_records[1024];
spadStop raw_stop;
spadFrame current_frame;
char outfile_name[1024];
char outfile_name_stem[1024];
unsigned long int options_splitfile = 0;
int splitfile_count = 0;

unsigned int pixel_indexes[1024];

for(i=0;i<1024;i++) {
    if(i%2) {
        pixel_indexes[i] = ( 0b1111100000 ^ ( (31-(i/64))<<5 ) ) |
                           ( i/2 & 0b000001111 );
    } else {
        pixel_indexes[i] = ( 0b1111100000 ^ ( (i+1)/2 & 0b1111100000 ) ) |
                           ( (i+1)/2 & 0b000001111 );
    }
}

if(argc<2) {
    fprintf(stderr,"usage: spadcounts [options] infile.bin\n\n");
    fprintf(stderr,"options:\n");
    fprintf(stderr,"      -a          ASCII output\n");
    fprintf(stderr,"      -b          binary output (default)\n");
    fprintf(stderr,"      -o file.out  output to filename.out\n");
    fprintf(stderr,"      -s N        new output file every N frames\n\n");
    exit(-1);
}

short int options_format = FORMAT_BINARY;

sprintf(outfile_name_stem, "%s.out", argv[argc-1]);

for(i=1;i<argc-1;i++) {
    if(strcmp(argv[i-1],"-o")==0) {

```

```

strcpy(outfile_name_stem, argv[i]);
} if(strcmp(argv[i-1],"-s")==0) {
    options_splitfile = atol(argv[i]);
    if(options_splitfile < 0) {
        fprintf(stderr,"error: invalid parameter for -s: %s\n", argv[i]);
        exit(1);
    }
} else if(strcmp(argv[i],"-a")==0) {
    options_format = FORMAT_ASCII;
} else if(strcmp(argv[i],"-b")==0) {
    options_format = FORMAT_BINARY;
}
}

if(options_splitfile > 0) {
    sprintf(outfile_name, "%s-%d", outfile_name_stem, splitfile_count++);
} else {
    sprintf(outfile_name, "%s", outfile_name_stem);
}

if((infile=fopen64(argv[argc-1],"rb"))==NULL) {
    fprintf(stderr,"error: unable to open file for reading: %s\n", argv[argc-1]);
    exit(1);
}

if((outfile=fopen64(outfile_name,"wb"))==NULL) {
    fprintf(stderr,"error: unable to open file for writing: %s\n", outfile_name);
    exit(1);
}

for(j=0;!feof(infile);j++) {

    result = fread(raw_records, sizeof(spadRecord), 1024, infile);
    if(result<1024) break;

    result = fread(&raw_stop, sizeof(spadStop), 1, infile);
    if(result<1) break;

    if(j > 0 && options_splitfile > 0 && j%options_splitfile ==0) {
        fclose(outfile);
        sprintf(outfile_name, "%s-%d", outfile_name_stem, splitfile_count++);
        if((outfile=fopen64(outfile_name,"wb"))==NULL) {
            fprintf(stderr,"error: unable to open file for writing: %s\n", outfile_name);

```

```

        exit(1);
    }
}

for(i=0;i<1024;i++) {
    if(raw_records[i].bits.coarse == 0b00111111) {
        current_frame.t[pixel_indexes[i]] = 65535;
    } else {
        current_frame.t[pixel_indexes[i]] = (raw_records[i].bits.coarse<<4 | raw_stop.bits.stop) - raw_rec
        // if previous was "negative", the count is invalid; we change it to 65535 (no data)
        if(current_frame.t[pixel_indexes[i]] > 32767) {
            current_frame.t[pixel_indexes[i]] = 65535;
        }
    }
}

for(i=0;i<1024;i++) {
    if(current_frame.t[i]!=65535) {
        if(options_format==FORMAT_ASCII) {
            fprintf(outfile, "%ld %d %d\n", j, i, current_frame.t[i]);
        } else if(options_format==FORMAT_BINARY) {
            outrec = ((uint64_t)j<<32) | ((uint64_t)i<<16) | ((uint64_t)current_frame.t[i]);
            fwrite(&outrec, 8, 1, outfile);
        }
    }
}

if(j%4096==0) {
    printf("Reading frame %ld ...\\r", j);
    fflush(stdout);
}
printf("done
\\n");

fclose(infile);
fclose(outfile);

exit(0);
return(0);
}

```



# Bibliography

- [1] Dheera Venkatraman. Tools for quantum optics : pulsed polarization-maintaining erb-doped fiber laser and spatial mode manipulation in spontaneous parametric downconversion. Master's thesis, Massachusetts Institute of Technology, 2007.
- [2] Baris I. Erkmen and Jeffrey H. Shapiro. Unified theory of ghost imaging with gaussian-state light. *Phys. Rev. A*, 77:043809, Apr 2008.
- [3] Dharmpal Takhar, Jason N. Laska, Michael B. Wakin, Marco F. Duarte, Dror Baron, Shriram Sarvotham, Kevin F. Kelly, and Richard G. Baraniuk. A new compressive imaging camera architecture using optical-domain compression. In *Proceedings of Computational Imaging IV at SPIE Electronic Imaging*, pages 43–52, San Jose, CA, Jan. 2006.
- [4] Ayman F. Abouraddy, Magued B. Nasr, Bahaa E. A. Saleh, Alexander V. Sergienko, and Malvin C. Teich. Quantum-optical coherence tomography with dispersion cancellation. *Phys. Rev. A*, 65:053817, May 2002.
- [5] Magued B. Nasr, Bahaa E. A. Saleh, Alexander V. Sergienko, and Malvin C. Teich. Demonstration of dispersion-canceled quantum-optical coherence tomography. *Phys. Rev. Lett.*, 91:083601, Aug 2003.
- [6] C. K. Hong, Z. Y. Ou, and L. Mandel. Measurement of subpicosecond time intervals between two photons by interference. *Phys. Rev. Lett.*, 59:2044–2046, Nov 1987.

- [7] A. M. Steinberg, P. G. Kwiat, and R. Y. Chiao. Dispersion cancellation in a measurement of the single-photon propagation velocity in glass. *Phys. Rev. Lett.*, 68:2421–2424, Apr 1992.
- [8] J. D. Franson. Nonlocal cancellation of dispersion. *Phys. Rev. A*, 45:3126–3132, Mar 1992.
- [9] Baris I. Erkmen and Jeffrey H. Shapiro. Phase-conjugate optical coherence tomography. *Phys. Rev. A*, 74:041601, Oct 2006.
- [10] Baris I. Erkmen. *Phase-Sensitive Light: Coherence Theory and Applications to Optical Imaging*. PhD thesis, Massachusetts Institute of Technology, May 2008.
- [11] C. K. Hong, Z. Y. Ou, and L. Mandel. Measurement of subpicosecond time intervals between two photons by interference. *Phys. Rev. Lett.*, 59:2044–2046, Nov 1987.
- [12] W. H. Louisell, A. Yariv, and A. E. Siegman. Quantum fluctuations and noise in parametric processes. i. *Phys. Rev.*, 124:1646–1654, Dec 1961.
- [13] S. E. Harris, M. K. Oshman, and R. L. Byer. Observation of tunable optical parametric fluorescence. *Phys. Rev. Lett.*, 18:732–734, May 1967.
- [14] Douglas Magde and Herbert Mahr. Study in ammonium dihydrogen phosphate of spontaneous parametric interaction tunable from 4400 to 16 000 Å. *Phys. Rev. Lett.*, 18:905–907, May 1967.
- [15] S. A. Akhmanov, O. N. Chunaev, V. V. Fadeev, R. V. Khokhlov, D. N. Klyshko, A. I. Kovrigin, and A. S. Piskarskas. Parametric Generators of Light. In J. Fox, editor, *Modern Optics*, page 343, 1967.
- [16] R. L. Byer and S. E. Harris. Power and bandwidth of spontaneous parametric emission. *Phys. Rev.*, 168:1064–1068, Apr 1968.
- [17] David C. Burnham and Donald L. Weinberg. Observation of simultaneity in parametric production of optical photon pairs. *Phys. Rev. Lett.*, 25:84–87, Jul 1970.

- [18] P. R. Tapster, J. G. Rarity, and J. S. Satchell. Use of parametric down-conversion to generate sub-poissonian light. *Phys. Rev. A*, 37:2963–2967, Apr 1988.
- [19] Sylvain Fasel, Olivier Alibart, Sbastien Tanzilli, Pascal Baldi, Alexios Beveratos, Nicolas Gisin, and Hugo Zbinden. High-quality asynchronous heralded single-photon source at telecom wavelength. *New Journal of Physics*, 6(1):163, 2004.
- [20] T.B. Pittman, B.C. Jacobs, and J.D. Franson. Heralding single photons from pulsed parametric down-conversion. *Optics Communications*, 246(46):545 – 550, 2005.
- [21] Christian Kurtsiefer, Markus Oberparleiter, and Harald Weinfurter. High-efficiency entangled photon pair collection in type-ii parametric fluorescence. *Phys. Rev. A*, 64:023802, Jul 2001.
- [22] F.N.C. Wong, J.H. Shapiro, and T. Kim. Efficient generation of polarization-entangled photons in a nonlinear crystal. *Laser Physics*, 16(11):1517–1524, 2006.
- [23] Daniel Ljunggren and Maria Tengner. Optimal focusing for maximal collection of entangled narrow-band photon pairs into single-mode fibers. *Phys. Rev. A*, 72:062301, Dec 2005.
- [24] Fabio Antonio Bovino, Pietro Varisco, Anna Maria Colla, and Er V. Sergienko. Effective fiber-coupling of entangled photons for quantum communication, opt. *Commun*, pages 343–348, 2003.
- [25] Ryan S. Bennink, Yun Liu, D. Duncan Earl, and Warren P. Grice. Spatial distinguishability of photons produced by spontaneous parametric down-conversion with a focused pump. *Phys. Rev. A*, 74:023802, Aug 2006.
- [26] Alessandro Fedrizzi, Thomas Herbst, Andreas Poppe, Thomas Jennewein, and Anton Zeilinger. A wavelength-tunable fiber-coupled source of narrowband entangled photons. *Opt. Express*, 15(23):15377–15386, Nov 2007.

- [27] G. D. Boyd and D. A. Kleinman. Parametric Interaction of Focused Gaussian Light Beams. *Journal of Applied Physics*, 39:3597–3639, July 1968.
- [28] Julien Le Gouët, Dheera Venkatraman, Franco N. C. Wong, and Jeffrey H. Shapiro. Classical low-coherence interferometry based on broadband parametric fluorescence and amplification. *Opt. Express*, 17(20):17874–17887, Sep 2009.
- [29] Ryan S. Bennink. Optimal collinear gaussian beams for spontaneous parametric down-conversion. *Phys. Rev. A*, 81:053805, May 2010.
- [30] P. Ben Dixon, Danna Rosenberg, Veronika Stelmakh, Matthew E. Grein, Ryan S. Bennink, Eric A. Dauler, Andrew J. Kerman, Richard J. Molnar, and Franco N. C. Wong. Heralding efficiency and correlated-mode coupling of near-ir fiber-coupled photon pairs. *Phys. Rev. A*, 90:043804, Oct 2014.
- [31] T. B. Pittman, Y. H. Shih, D. V. Strekalov, and A. V. Sergienko. Optical imaging by means of two-photon quantum entanglement. *Phys. Rev. A*, 52:R3429–R3432, Nov 1995.
- [32] Alejandra Valencia, Giuliano Scarcelli, Milena D’Angelo, and Yanhua Shih. Two-photon imaging with thermal light. *Phys. Rev. Lett.*, 94:063601, Feb 2005.
- [33] F. Ferri, D. Magatti, A. Gatti, M. Bache, E. Brambilla, and L. A. Lugiato. High-resolution ghost image and ghost diffraction experiments with thermal light. *Phys. Rev. Lett.*, 94:183602, May 2005.
- [34] Ayman F. Abouraddy, Bahaa E. A. Saleh, Alexander V. Sergienko, and Malvin C. Teich. Role of entanglement in two-photon imaging. *Phys. Rev. Lett.*, 87:123602, Aug 2001.
- [35] Ayman F. Abouraddy, Bahaa E. A. Saleh, Alexander V. Sergienko, and Malvin C. Teich. Entangled-photon fourier optics. *J. Opt. Soc. Am. B*, 19(5):1174–1184, May 2002.

- [36] Milena D'Angelo, Yoon-Ho Kim, Sergei P. Kulik, and Yanhua Shih. Identifying entanglement using quantum ghost interference and imaging. *Phys. Rev. Lett.*, 92:233601, Jun 2004.
- [37] Ryan S. Bennink, Sean J. Bentley, Robert W. Boyd, and John C. Howell. Quantum and classical coincidence imaging. *Phys. Rev. Lett.*, 92:033601, Jan 2004.
- [38] A. Gatti, E. Brambilla, and L. A. Lugiato. Entangled imaging and wave-particle duality: From the microscopic to the macroscopic realm. *Phys. Rev. Lett.*, 90:133603, Apr 2003.
- [39] Xiaodong Xun and Robert W. Cohn. Phase calibration of spatially nonuniform spatial light modulators. *Appl. Opt.*, 43(35):6400–6406, Dec 2004.
- [40] J. Janesick and T. Elliott. Astronomical ccd observing and reduction techniques. *Astronomical Society of the Pacific Conference Series*, 23:1–67, 1992.
- [41] Baris I. Erkmen and Jeffrey H. Shapiro. Ghost imaging: from quantum to classical to computational. *Adv. Opt. Photon.*, 2(4):405–450, Dec 2010.
- [42] Baris I. Erkmen and Jeffrey H. Shapiro. Signal-to-noise ratio of gaussian-state ghost imaging. *Phys. Rev. A*, 79:023833, Feb 2009.
- [43] Jeffrey H. Shapiro. Computational ghost imaging. *Phys. Rev. A*, 78:061802, Dec 2008.
- [44] Nicholas D. Hardy. *Analyzing and Improving Image Quality in Reflective Ghost Imaging*. PhD thesis, Massachusetts Institute of Technology, February 2011.
- [45] Yaron Bromberg, Ori Katz, and Yaron Silberberg. Ghost imaging with a single detector. *Phys. Rev. A*, 79:053840, May 2009.
- [46] Emmanuel J. Cands, Justin K. Romberg, and Terence Tao. Stable signal recovery from incomplete and inaccurate measurements. *Communications on Pure and Applied Mathematics*, 59(8):1207–1223, 2006.

- [47] M.F. Duarte, M.A. Davenport, D. Takhar, J.N. Laska, Ting Sun, K.F. Kelly, and R.G. Baraniuk. Single-pixel imaging via compressive sampling. *Signal Processing Magazine, IEEE*, 25(2):83–91, March 2008.
- [48] Ori Katz, Yaron Bromberg, and Yaron Silberberg. Compressive ghost imaging. *Applied Physics Letters*, 95(13):–, 2009.
- [49] Emmanuel C and Justin Romberg. 1-magic: Recovery of sparse signals via convex programming.
- [50] J. Yang and Y. Zhang. Alternating direction algorithms for l1-problems in compressive sensing.
- [51] J. C. Nicolas. Applications of low-light imaging to life sciences. *Journal of Bioluminescence and Chemiluminescence*, 9(3):139–144, 1994.
- [52] W. Becker, A. Bergmann, M.A. Hink, K. Knig, K. Benndorf, and C. Biskup. Fluorescence lifetime imaging by time-correlated single-photon counting. *Microscopy Research and Technique*, 63(1):58–66, 2004.
- [53] Neil Savage. Single-photon counting. *Nature Photonics*, 3(12):738–739, 2009.
- [54] Gerald S. Buller and A.M. Wallace. Ranging and three-dimensional imaging using time-correlated single-photon counting and point-by-point acquisition. *Selected Topics in Quantum Electronics, IEEE Journal of*, 13(4):1006–1015, July 2007.
- [55] Michael Jack, Justin Wehner, John Edwards, George Chapman, Donald N. B. Hall, and Shane M. Jacobson. Hgcdte apd-based linear-mode photon counting components and ladar receivers, 2011.
- [56] Marius A. Albota, Richard M. Heinrichs, David G. Kocher, Daniel G. Fouche, Brian E. Player, Michael E. O’Brien, Brian F. Aull, John J. Zaykowski, James Mooney, Berton C.

- Willard, and Robert R. Carlson. Three-dimensional imaging laser radar with a photon-counting avalanche photodiode array and microchip laser. *Appl. Opt.*, 41(36):7671–7678, Dec 2002.
- [57] John J. Degnan. Photon-counting multikilohertz microlaser altimeters for airborne and spaceborne topographic measurements. *Journal of Geodynamics*, 34(34):503 – 549, 2002.
- [58] D. L. Snyder. Random point processes. 1975.
- [59] Michael E O'Brien and Daniel G Fouche. Simulation of 3d laser radar systems. *Lincoln Laboratory Journal*, 15(1):37–60, 2005.
- [60] Aongus McCarthy, Nils J. Krichel, Nathan R. Gemmell, Ximing Ren, Michael G. Tanner, Sander N. Dorenbos, Val Zwiller, Robert H. Hadfield, and Gerald S. Buller. Kilometer-range, high resolution depth imaging via 1560 nm wavelength single-photon detection. *Opt. Express*, 21(7):8904–8915, Apr 2013.
- [61] Sara Pellegrini, Gerald S Buller, Jason M Smith, Andrew M Wallace, and Sergio Cova. Laser-based distance measurement using picosecond resolution time-correlated single-photon counting. *Measurement Science and Technology*, 11(6):712, 2000.
- [62] F. Villa, B. Markovic, S. Bellisai, D. Bronzi, A. Tosi, F. Zappa, S. Tisa, D. Durini, S. Weyers, U. Paschen, and W. Brockherde. Spad smart pixel for time-of-flight and time-correlated single-photon counting measurements. *Photonics Journal, IEEE*, 4(3):795–804, June 2012.
- [63] Fabrizio Guerrieri, Simone Tisa, Alberto Tosi, and Franco Zappa. Two-dimensional spad imaging camera for photon counting. *Photonics Journal, IEEE*, 2(5):759–774, 2010.
- [64] Carmelo Scarella, Alberto Tosi, Federica Villa, Simone Tisa, and Franco Zappa. Low-noise low-jitter 32-pixels cmos single-photon avalanche diodes array for single-photon counting from 300 nm to 900 nm. *Review of Scientific Instruments*, 84(12):–, 2013.

- [65] Ahmed Kirmani, Dheera Venkatraman, Dongeek Shin, Andrea Colao, Franco N. C. Wong, Jeffrey H. Shapiro, and Vivek K Goyal. First-photon imaging. *Science*, 343(6166):58–61, 2014.
- [66] Dongeek Shin, Ahmed Kirmani, Vivek K. Goyal, and Jeffrey H. Shapiro. Photon-Efficient Computational 3D and Reflectivity Imaging with Single-Photon Detectors. *arXiv/stat*, 2014.
- [67] S. G. Mallat. A wavelet tour of signal processing. 2009.
- [68] S. P. Boyd and L. Vandenberghe. Convex optimization. 2004.
- [69] Roman Garnett, Timothy Huegerich, Charles Chui, and Wenjie He. A universal noise removal algorithm with an impulse detector. *Image Processing, IEEE Transactions on*, 14(11):1747–1754, 2005.
- [70] D. P. Bertsekas and J. N. Tsitsiklis. Introduction to probability. 2002.
- [71] Zachary T Harmany, Roummel F Marcia, and Rebecca M Willett. This is spiral-tap: sparse poisson intensity reconstruction algorithmstheory and practice. *Image Processing, IEEE Transactions on*, 21(3):1084–1096, 2012.
- [72] Federica Alberta Villa. *Time-of-flight camera for long-distance 3D ranging*. PhD thesis, Politecnico di Milano, 2013.